



Romanian Authority for Nuclear Activities
Institute of Nuclear Research-Pitesti



Gesellschaft für Anlagen-
und Reaktorsicherheit
(GRS) mbH

Comparison of safety
assessments for spent
CANDU or LWR fuels in
repositories in rock salt



Romanian Authority for Nuclear Activities
Institute of Nuclear Research-Pitesti



Gesellschaft für Anlagen-
und Reaktorsicherheit
(GRS) mbH

Comparison of safety
assessments for spent
CANDU or LWR fuels in
repositories in rock salt

Dieter Buhmann
Alice Ionescu
Margarit Pavelescu
Richard Storck

September 2000

Remarks:

This work has been financially supported by a linkage grant of the scientific part of the North Atlantic Treaty Organisation (NATO) under contract no. LG 972750. Work has been carried out by Gesellschaft für Anlagen- und Reaktorsicherheit (GRS) mbH in cooperation with Institute for Nuclear Research (INR) in Romania. Only the authors are responsible for the contents of this report.

GRS - 168
SCN-N.T. 250/2000
ISBN 3-931995-34-8

Deskriptoren:

Aktiver Abfall, Brennelement, CANDU, Endlagerung, Langzeitsicherheit, LWR, Modell, Salz, Sicherheitsanalyse

Abstract

A long-term safety assessment of a repository for either spent CANDU or LWR fuel elements in a salt formation has been performed. A hypothetical repository site has been considered, using data of the European Community project PAGIS for all parts of the system: near field, overburden, and biosphere. Three scenarios have been taken into account: subsidence as the normal evolution of the salt dome, a combined scenario with brine intrusion from the overburden and from undetected brine pockets, and a cavern scenario representing future human actions. Spent fuel elements have been assumed to be disposed of in big storage casks in drifts. For reasons of comparability, the same source term model has been applied for both waste types, but different inventories of radionuclides and different heat production rates have been taken into account. The key parameter for assessing long-term safety was the radiation exposure in the biosphere.

The results of the calculations demonstrate that both types of waste can be disposed of safely. For the combined brine intrusion scenario and for the human intrusion scenario, the radiation exposures are below the limit of German radiation protection law. In the subsidence scenario, however, for conservative values of the input parameters, the limit is exceeded in some calculations. This reflects the situation of a flat emplacement area, which is quickly decoupled by subsidence, leading to high nuclide concentrations. As the subsidence model is very simple and over-conservative, this result must not be over-interpreted. A comparison with the results of PAGIS, which have been derived from the disposal of high-level waste in deep boreholes, in general shows higher consequences in case of a direct disposal of fuel elements.

Table of contents

Abstract	I
Table of contents	III
1 Introduction	1
2 Modelling	3
2.1 Subrosion scenario	4
2.1.1 First phase of the subrosion scenario	5
2.1.2 Second phase of the subrosion scenario	6
2.2 Human intrusion scenario	9
2.2.1 Cavity	11
2.2.2 Sealing of the cavity	12
2.2.3 Sump	13
2.2.4 Additional phenomena	14
2.3 Combined accident scenario	15
2.3.1 Source term for spent fuel elements	17
2.3.1.1 Container failure	17
2.3.1.2 Mobilisation from the waste matrix	20
2.3.1.3 Precipitation	23
3 Input data	25
3.1 General data for the repository system	26
3.1.1 Temperature data	26
3.1.2 Design data	29
3.1.3 Waste inventories	30
3.1.4 Mobilisation data and solubility limits	31
3.1.5 Dose conversion factors	33
3.2 Specific data	34
3.2.1 Subrosion scenario	34
3.2.2 Human intrusion scenario	37
3.2.3 Combined accident scenario	42

4	Results	43
4.1	Best estimate results	43
4.1.1	Subrosion scenario	43
4.1.2	Human intrusion scenario	44
4.1.3	Combined accident scenario	50
4.1.3.1	Repository with CANDU fuel elements	50
4.1.3.2	Repository with spent LWR fuel elements	55
4.2	Local sensitivity analyses	57
4.2.1	Local sensitivity analyses: Subrosion scenario	57
4.2.2	Local sensitivity analyses: Human intrusion scenario	60
4.2.2.1	Variation of the solubility limits	60
4.2.2.2	Variation of the diffusion coefficient	61
4.2.2.3	Variation of the exponent q in the permeability-porosity relation	62
4.2.2.4	Variation of the reference convergence rate	63
4.2.2.5	Variation of the maximum brine pressure	65
4.2.3	Local sensitivity analyses: Combined accident scenario	67
4.2.3.1	Variation of volume of brine pockets	67
4.2.3.2	Variation of the time of brine intrusion from the overburden	69
4.2.3.3	Variation of the reference convergence rate	70
4.2.4	Summary of results	72
4.2.4.1	Subrosion scenario	73
4.2.4.2	Human intrusion scenario	73
4.2.4.3	Combined scenario	74
4.2.4.4	Comparison with results of the PAGIS exercise	75
5	Summary and conclusions	77
6	References	81
	Acknowledgements	82
	List of Figures	83
	List of Tables	85

1 Introduction

In Romania, nuclear power is generated by Canadian type reactors which use natural uranium as nuclear fuel (in the following called CANDU fuel). The spent fuel elements of these power plants are planned to be disposed of either in a salt or a hard rock formation. This report investigates the consequences of direct disposal in a deep repository in salt with respect to long-term safety. The results are compared to those of a hypothetical German concept of direct disposal of spent light water reactor (LWR) fuel elements in salt. All of these investigations are closely related to the models and results of the PAGIS exercise of the European Community, which were published in the year 1988 [6].

Salt is chosen as host rock due to some favourable characteristics regarding long-term performance. Among these are the low permeability and the creeping behaviour. Due to the low permeability, the environment of the waste containers is usually dry because flow of water is negligible. The creeping behaviour of salt, which is also called convergence, results in sealing of any faults that may appear by mechanical stresses and which may provide a path for the release of radioactivity. Thus, under normal conditions and on a short time scale, no release of radionuclides from the repository to the biosphere is expected. But on a long time scale the uplift of the salt dome and following subsidence by groundwater are possible mechanisms that may result in a contamination of the biosphere.

Besides the normal evolution of a salt dome, some exceptional situations may appear which may result in a release of radionuclides from the salt to the geosphere. These situations are modelled by altered evolution scenarios, and are related to the presence of water in the neighbourhood of the waste containers. One possible mechanism by which waste may come into contact to water is an intrusion of brine through a main anhydrite vein or from undetected brine pockets near emplacement drifts. Further possible mechanisms are human activities in the future.

Three consequence calculations are performed: 1. normal evolution of the repository, modelled by a subsidence scenario, 2. human intrusion, modelled by a storage cavern scenario, and 3. combined accident scenario, which consists of a combination of a brine

intrusion from the overburden via a fault in the rock salt and from brine pockets near the emplacement drifts.

The repositories for spent CANDU or LWR fuel elements are assumed to be different mainly in the data of the source term for spent fuel and the temperatures of the emplacement fields. Differences in the amount of waste of both countries are also taken into account. A common model of the source term is applied for both fuel types to improve the comparability of the results.

The calculations are performed using modules of the computer code package EMOS [2]. The older version EMOS5 containing the modules REPOS, CHET and EXPOS is used for the calculation of the subsidence and human intrusion scenarios, while the new version EMOS7 containing modules REPOS6, CHETLIN2 and EXCON1 is used for the calculation of the combined accident scenario. The release of radionuclides from the near field is calculated by REPOS or REPOS6, while CHET or CHETLIN2 calculates the transport in the geosphere. The biosphere codes EXPOS and EXCON1 are used to calculate radiation exposure from radionuclide concentration in groundwater.

The consequences are mainly discussed in terms of annual radiation exposures (effective doses) to future human beings. A purely deterministic approach is applied, and local sensitivity analyses are performed.

In the following, the three scenarios are described, the basic data for the repository systems are presented, and the most interesting characteristics of the modelling approaches for every scenario are briefly shown. A detailed discussion of the results for each of these scenarios follows next. Finally, a summary and conclusion of the results is presented.

2 Modelling

To assess the long-term safety of a repository system, scenarios have to be defined in order to describe the possible future evolution of the system. Scenarios are developed from combinations of features, events, and processes (FEPs) of the repository system. A systematic approach for scenario development has not been followed in this exercise; instead, the procedure described in PAGIS [6] has been adapted.

In PAGIS two categories of evolution have been identified: the so-called normal evolution of the system and the altered evolution, which refers to disruptive events that may interfere with the normal evolution. In these types of evolution the time scale plays an important role. This is mainly due to the different nature of influences that govern the development over a certain time period and that require different kinds of models for the evaluation, and also due to the strong time dependence of the radionuclide inventory. The normal evolution that develops over a long time (i. e. over millions of years) is represented by the subsidence scenario in the actual analyses. For the medium-term development, in a time range between some hundreds to some thousands of years, human actions are taken into account (human intrusion scenario by cavern leaching). For the short term, within the next hundreds of years, brine flow into the drift system of the repository is assumed (i. e. combined accident scenario). The scenarios selected for the present investigation are discussed in detail in the following chapters. A detailed discussion of long-term, short-term, and medium-term events at the repository site is given in reference [6].

Undisturbed rock salt is impermeable to water. Thus, it is in principle an ideal medium for the storage of wastes because leaching of waste is not possible and no transport of contaminants can occur. However, due to the mining actions during the emplacement period, the system is disturbed and the access drifts in the mine are possible pathways for contaminant transport. Furthermore, the heat producing waste leads to mechanical stresses in the host rock, which can result in cracks opening up potential pathways.

Due to the creeping behaviour of salt, open voids are reduced in time. This process is accelerated by high temperatures which usually occur in a repository containing high level waste. Thus, a repository in salt tends to a final state where all the wastes are enclosed

by impermeable rock material. Nevertheless, a release of contaminants is possible by normal evolution processes and by disruptive events, as discussed in the following.

The scenarios differ mainly for the near field models. Geosphere and biosphere are modelled in the same way for the combined accident and the human intrusion scenario. For the subsrosion scenario the geosphere is not modelled explicitly.

Radionuclide transport through the overburden is modelled by a one-dimensional convection-dispersion equation, taking into account sorption processes [6]. Calculation of radiological consequences starts from the radionuclide concentrations in near-surface ground water which are converted to radiation exposure by means of dose conversion factors [6].

2.1 Subrosion scenario

The scenario assumes that the salt dome is dissolved by groundwater in the cap rock region. The subsrosion of the top of the salt dome is balanced by a halokinetic uplift, so that the depth of the salt dome top is unchanged. As a consequence, the emplacement field raises continuously and finally reaches the top of the dome. Waste is degraded and dissolved congruently with salt and transported through the aquifers of the overburden to the biosphere. Here the concentration of radionuclides in drinking water and water for agricultural purposes is reduced by the assumption that due to the high salinity ground water has to be dituted for drinking quality.

The emplacement sites of the repository are located some 500 m below the top of the present salt dome. The dissolution of the rock salt above the emplacement sites will take about several millions of years. Once this has occurred the waste will come into direct contact with groundwater and the remaining radionuclides will pass into the water. The radiological consequences to the population are determined by the residual barrier effects of the salt rock and the overburden.

The main difficulties encountered in predicting the radiological consequences of such a scenario are related by uncertainties in predicting the subsrosion rate, the long-term evo-

lution of the future overburden and ground water movement, and the consumption habits of the future population.

Therefore, a simple model which allows calculation of the radiological consequences has been proposed for the subsrosion scenario [6]. The difficulties previously mentioned are dealt with by conservative assumptions, which overestimate the consequences of the scenario. The uncertainties in the subsrosion rate and in the dilution of the contaminated brine are represented by a range of parameter values, which are used in local sensitivity analyses. In order to describe the processes in the future overburden, modelling approaches are selected which do not require detailed knowledge of future groundwater movement or the structure of the future overburden. Present day consumption habits are used as a basis for intake of radionuclides via drinking water and food chains.

A detailed time history of the subsrosion process has not been modelled because only the point of time at which water contacts the wastes is important. From this moment on, the radionuclides pass together with the dissolved salt into the water. The evolution of the scenario can therefore be divided into two time periods. The qualitative and quantitative description of these periods as well as the mathematical modelling are presented in the following paragraphs.

2.1.1 First phase of the subsrosion scenario

During the first phase the salt dome is eroded from the present salt top down to the repository depth. The activity inventory of radionuclides is reduced by radioactive decay up to the time of release. Due to the lithostatic pressure on the waste containers in this time interval it can be assumed that the containers are damaged and that the waste matrices are fragmented. Due to the creep properties of salt, the waste fragments are enclosed by rock salt.

As already mentioned, subsrosion of a salt dome is subject to strong temporal changes. Thus, according to the literature, the subsrosion rate may be characterized by a log-normal distribution with the most probable value of 0.033 mm/y [6]. The subsrosion rate determines the moment of release, which is the time when release of radionuclides into the

groundwater starts. With a distance of 500 m between the emplacement level and the present salt top, the best estimate value for the moment of release is $1.5 \cdot 10^7$ y. The 3- σ range of the log-normal distribution is from $2.25 \cdot 10^5$ y to $1 \cdot 10^9$ y.

2.1.2 Second phase of the subrosion scenario

During the second phase radionuclides and salt are jointly released into the water and are transported through the geosphere. This transport is retarded by the potential barrier effects of the waste containers, the residual salt rock, the overburden, and the biosphere. In the following the basic assumptions for these processes are discussed.

The waste containers are assumed to be entirely damaged due to the lithostatic pressure during the first phase of the scenario. Therefore, their barrier function is neglected.

Erosion of salt is determined by the rate of removal of the leaching fluid and the dissolved salt. Removal of the dissolved salt is caused by convective fluid transport, diffusion, and dispersion. Although the dissolution of salt in saturated brine stops, saturated brine can still dissolve waste. Therefore, it is assumed that the waste matrix dissolves quickly in contact with brine, in particular because it is already fragmented.

During dissolution of the waste matrix a maximum of the radionuclide concentration occurs at the dissolution location. This maximum is reduced by diffusion and dispersion processes. As dissolution of all waste containers occurs simultaneously over the whole emplacement field, at some distance from the release location it can be assumed that the radionuclide/salt ratio in the brine is approximately the same as the average radionuclide/salt ratio in the emplacement field. This is a conservative assumption because the dissolution of salt occurs evenly across the whole salt dome, while the dissolution of waste matrices is strictly localized.

During the dissolution process the radionuclides are in contact with highly concentrated brine. Dilution with slightly mineralized (or fresh) surface waters will lower the salt and nuclide concentration until water can be used for drinking and agricultural purposes. Thus, the reduction of the radionuclide concentration during transport through the over-

burden is identical with that of salt as long as sorption processes are not considered. Sorption shifts the concentration maxima of some of the radionuclides to lower values and the time of arrival of these maxima in the biosphere to later times.

According to Figure 2.1, the total volume of the emplacement area, i. e. the volume of emplaced canisters surrounded by rock salt, can be estimated by the dimensions of the original emplacement area prior to subsrosion. It is assumed that over the geological time period the original dimensions are changed. This is especially relevant for the height, which is assumed to be about 10 m until the subsrosion process reaches the emplacement level. All data are given in Chapter 3.2.2.

Release of radionuclides stretches over a time period which depends on the subsrosion rate and the height of the disposal field. For the range of the subsrosion rates of 2.2 mm/y to 0.0005 mm/y and the height of the disposal field of 10 m, the release durations are between $4.5 \cdot 10^3$ y and $2 \cdot 10^7$ y. A release duration of $3.0 \cdot 10^5$ y results for the best estimate value of 0.033 mm/y.

The transport times of radionuclides through the overburden are between 10^3 y for mobile nuclides and 10^5 y for less mobile nuclides [6]. Thus, only for mobile nuclides and high subsrosion rates is the release duration comparable to the transport times. For lower sub-

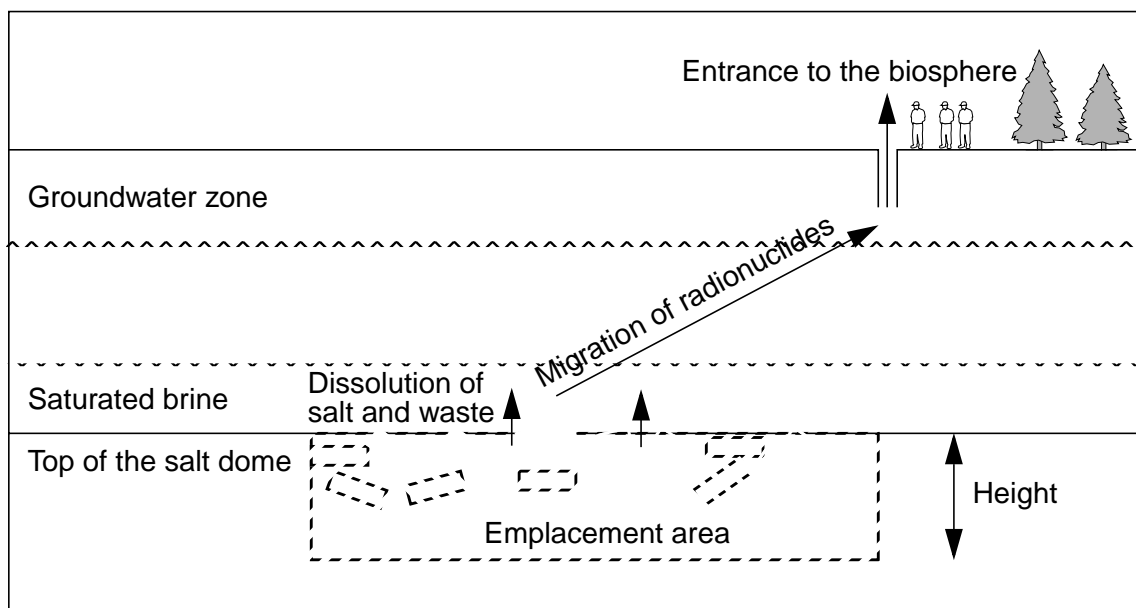


Fig. 2.1 Subrosion scenario: model of nuclide migration (adapted from [6])

rosion rates and less mobile nuclides, however, the transport times are usually lower than the release durations. Thus, the model assumption of a neglect of transport processes in the geosphere is justified.

Short-lived nuclides are not considered since decay during the first phase of the subrosion scenario results in negligible concentrations. An exception are short-lived daughter nuclides. If their half-lives are short compared to their transport times, then it is assumed that they reach the biosphere in secular equilibrium with their parent nuclides. Inventories of these daughter nuclides and the corresponding dose conversion factors are added in an adequate way to the parent nuclides, cf. Table 3.6.

In the following, the mathematical models are described. The specific activity $a_i(t_f)$ in the brine is related to the dissolved quantity of salt m_s , assuming congruent dissolution.

$$a_i(t_f) = A_i(t_f) / m_s \quad (1)$$

where:

A_i activity inventory [Bq] of the radionuclide i in the emplacement field

m_s salt mass [kg] of the emplacement field

t_f release moment [y], related to the subrosion rate

Dilution of brine to drinking water quality during migration in the overburden is taken into account by a dilution factor. Change in the concentration of short-lived daughter nuclides caused by sorption processes and decay are taken into account. The change in concentration of the daughter as compared to the concentration of the long-lived parent is represented by the correction factor $r_{s,i}$, defined as the ratio of retardation factors of the parent and the daughter.

The overall radiological consequences are calculated as sum over all nuclides j as

$$D(t_f) = \sum_j C_{m,s} \cdot \frac{A_j(t_f)}{m_s} \cdot \left(d_j + \sum_i d_i \cdot r_{s,i} \right), \quad (2)$$

where:

$D(t_f)$	total dose [Sv/y] neglecting different transport times from the beginning of the release
d_j, d_i	dose conversion factors [$\text{Sv y}^{-1} \text{ Bq}^{-1}$ l] of the nuclides j and i , resp.
$r_{s,i} = Rf_j/Rf_i$	correction factor of the parent j to the daughter i
$A_j(t_f)$	activity inventory [Bq] at the release moment of the parent j
$C_{m,s}$	salt concentration [kg/l] in the water

The summation j is over all long-lived parents, while the summation i is over all short-lived daughters of nuclide j .

2.2 Human intrusion scenario

It is assumed that during the solution mining of a storage cavern parts of a 1 000-year-old repository with radioactive waste are laid bare. The waste containers in the affected region fall down to the ground of the excavated volume and are buried in the sump of insolubles at the bottom of the cavern. It is likely that all the containers are then defective and that the corrosion of the waste matrix starts immediately. Due to the continuing excavation process the containers are covered by an additional layer of insolubles. Thus, the sump is divided into two parts: the bottom part containing insolubles and waste, the upper part only insolubles.

After the mining process the brine in the cavern is replaced by the medium to be stored. The operational phase of the cavern is assumed to last for about 50 y until the cavern is abandoned. Then the storage medium is replaced by brine to support the mechanical stability of the cavern. Afterwards the access borehole is sealed with concrete. During the operational phase and later on, the volumes of the sump and the open part of the cavern are reduced by convergence. The radionuclides, which have been released from the containers into the bottom part of the sump, are transported into the cavity by the convergence driven flow of contaminated brine and also by molecular diffusion.

The treatment of the brine removed from the cavern to make way for the storage medium is not considered because the concentration of radionuclides in this brine should be relatively low within the short mining period.

Due to creeping of salt and due to the different densities of brine and rock salt, the cavern is not in a stable mechanical state after sealing of the access borehole. Consequently, the cemented casing-shoe of the access borehole is exposed to high stresses and is assumed to fail. As a consequence, a fracture may occur from the cavern to the overburden, establishing a pathway for contaminated brine.

The consequence of the failure of the sealing is a drop of the hydraulic pressure in the cavern, so the convergence of the fracture can start. This tends to restore the initial impermeability of the sealing. An equilibrium between convergence and divergence connected with a distinct sealing permeability is established in this way. This equilibrium is modelled by a constant value of the brine pressure in the cavern. The post-operational phase can thus be characterized by a stabilized cavern and a continuous leakage rate of brine into the overburden.

During the operational phase of the storage cavern, the pressure will be kept as high as possible to avoid a reduction of the cavern volume. However, since the duration of the operational phase is much shorter than that of the post-operational leakage phase, for simplification the hydraulic pressure assumed for the post-operational phase is applied to both phases.

The transport of radionuclides is mainly by advection with the brine, and to a smaller account by diffusion. This transport is from the bottom part of the sump into the top part of the sump and into the open volume of the cavern. As a retention mechanism for radionuclides along this path sorption at the insolubles is possible, but has been neglected because of a lack of data.

The contaminated brine from the cavern intrudes into the aquifers of the overburden. For simplicity, the same assumptions as for the combined accident scenario are adopted concerning the intrusion location and the pathway through the overburden (cf. Chapter 2.3).

The calculations are performed with the computer code EMOS in the version 5.02 [8]. This code contains two special models for the simulation of the solution mining scenario: one for the sump and one for the storage area of the cavern. The sealing of the cavern with its continuous leakage is modelled as a special physical effect by means of a resistor which limits the brine pressure to a fixed value. In the following, the special modelling of the sump as well as of the cavern and its sealing are discussed.

The cavern is modelled as a series of three sections. In the following the storage volume is called the cavity which is represented by only one section. The sump of the cavern is divided into two parts of equal size. The bottom part contains the wastes embedded in insolubles and brine. The top part of the sump is filled with brine and insolubles only. For simplicity, it is assumed that the cavern has a cylindrical shape.

Numerical values of the parameters for the best estimate calculation, as far as they differ from those used for the combined accident scenario (cf. Chapter 2.3), are given in Table 3.7.

2.2.1 Cavity

The cavity is modelled as a section with sealing. During the operational phase the section is filled with the stored medium. This medium is taken into account in the modelling by means of its hydrostatic pressure which reduces the convergence of the cavity.

At the end of the operational phase the cavity is filled with brine. This is simulated as a spontaneous fill-up of the cavity at $t = 50$ y. The brine pressure then increases instantaneously due to convergence until it attains a maximum value which opens the sealing of the access borehole.

The model for the cavity shows differences to the models for repository sections (cf. Chapter 2.3), as follows:

- cylindrical shape of the cavern,
- absence of backfill material,

- special modelling of the sealing resistance,
- brine pressure set to hydrostatic pressure,
- no flow of brine from the overburden into the cavern,
- instantaneous fill-up at $t = 50$ y.

The physical and chemical effects which are taken into account are:

- temperature for convergence and diffusion,
- convergence of the void volume,
- resistance of the sealing against the brine flow,
- radioactive decay,
- advective transport of radionuclides with the brine,
- transport of radionuclides by diffusion,
- precipitation due to solubility limits.

2.2.2 Sealing of the cavity

The sealing of the cavity is modelled in such a way that a continuous leakage rate is obtained. This leakage is assumed to be due to a constant brine pressure. The brine pressure in the cavern is given by the following set of equations:

$$B_j \left(1 - \frac{P_j}{P_p} \right)^m + R_j^{-1} (P_{j+1} - P_j) + R_{j-1}^{-1} (P_{j-1} - P_j) = 0 \quad (3)$$

where:

- B_j pressure independent part of convergence times volume (m^3/y)
- P_j brine pressure in section j (MPa)
- P_p petrostatic pressure (MPa)
- R_j resistance of the sealing of section j (MPa y m^{-3})
- m exponent of the relation between convergence rate and brine pressure; $m = 4$ (-)

Applying this equation to the cavity (index j), and taking into account that

$$P_{j+1} = p_H \quad \text{and} \quad P_j = p_{max}$$

the conductivity $1/R_j$ is obtained which maintains the brine pressure at the specified value of 15 MPa, related to the 800 m level:

$$R_j^{-1} = \frac{B_j \left(1 - \frac{p_{max}}{p_p}\right)^m + \dot{V}_{in} + R_{j-1}^{-1} (p_j - p_{max})}{(p_{max} - p_H)} \quad (4)$$

The brine pressure of the inner section (i. e. the sump) can be substituted by the flux of brine \dot{V}_{in} produced by the convergence of the sump:

$$\dot{V}_{in} = R_{j-1}^{-1} (p_{j-1} - p_j) \quad (5)$$

Since in equation 4 the conductivity is a function of the current brine pressure p_j , the final value p_{max} is attained asymptotically. For the best estimate calculations the term containing p_j is dropped, with the result that the brine pressure attains p_{max} within one time step.

2.2.3 Sump

Both parts of the sump are modelled with the same section model, because the volume of the containers can be ignored compared to the volume of the sump. The sump is described by a model similar to that of a drift section without sealing [8]. The differences between the models are:

- initial value of the porosity,
- cylindrical shape of the sump,
- initial value of the pressure set to hydrostatic pressure,
- void volume is filled with brine from the onset of the scenario.

The physical and chemical effects which are taken into account are:

- temperature for convergence and diffusion,
- convergence of the void volume,
- permeability of the sump filled with insolubles,
- flow resistance,
- radioactive decay,
- transport of radionuclides by diffusion,
- advective transport of radionuclides with brine,
- precipitation due to solubility limits.

2.2.4 Additional phenomena

The insolubles in the sump are modelled in the same way as the backfill in a section. The models used for all the phenomena correspond to those used for the combined accident scenario, as described in [8].

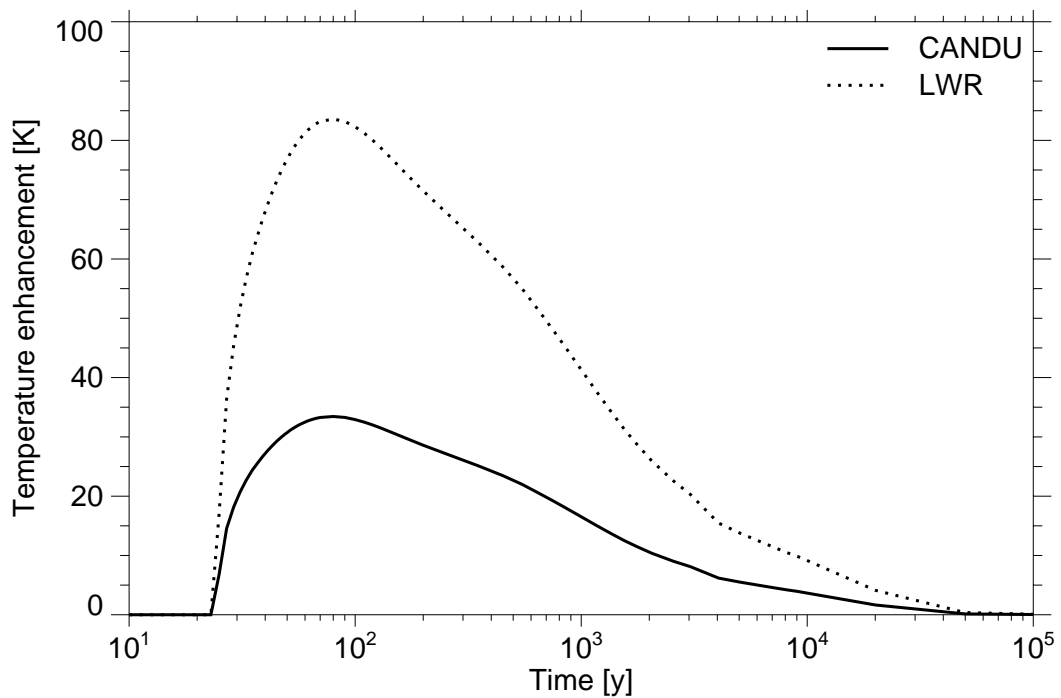


Fig. 2.2 Temperature curves for the sump

The temperature of the sump is assumed to correspond to a hot region of the initial emplacement field, while the temperature in the cavity, due to its large vertical extension, is assumed to be rock temperature. In Figure 2.2 the temperature curves for the sump of the cavern are shown for CANDU and LWR fuel. The temperatures with CANDU fuel are by a factor of 2.5 lower than for LWR fuel.

2.3 Combined accident scenario

The repository is modelled according to a hypothetical repository similar to that described in Ref. [4]. In the following, a short overview is given of the general modelling procedure. The source term for the release of radionuclides from spent fuel elements is assumed to be the same for spent LWR and CANDU fuel elements, but some data are assumed to be different. The modelling of the source term is presented in detail in Chapter 2.3.1. Finally, some relevant input data for the near field are compiled. The modelling and input data for the geosphere and biosphere are taken from Refs. [4] and [6] without changes.

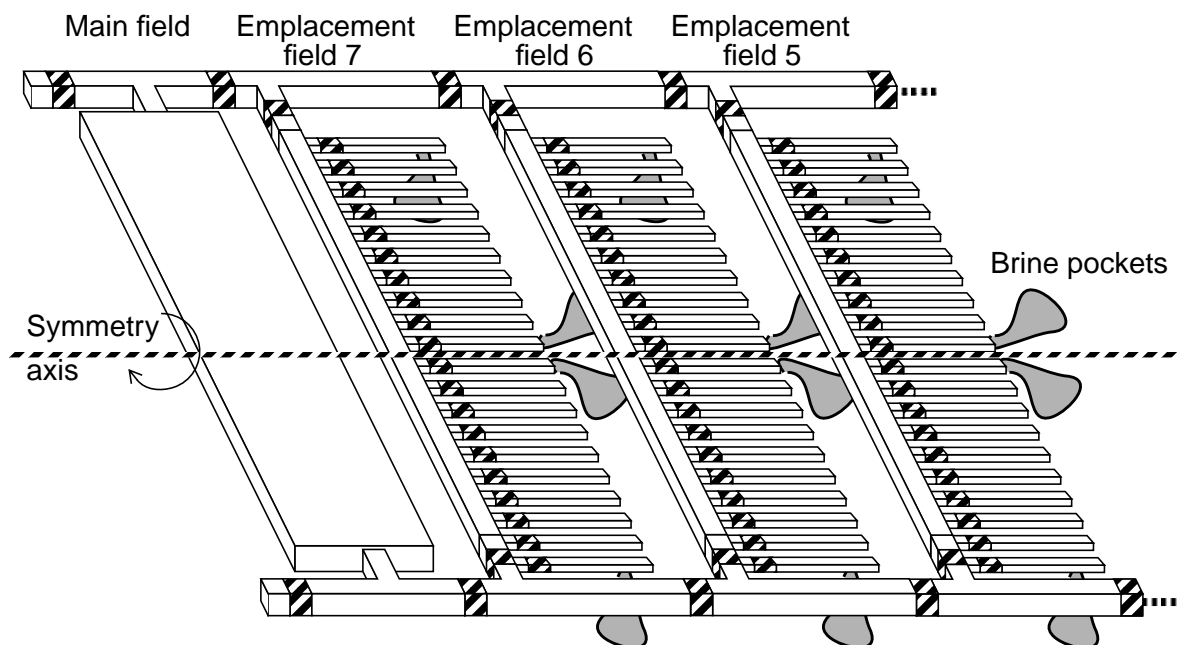


Fig. 2.3 Part of the section system of the near field. The entire repository consists of 7 emplacement fields

The section structure of the near field is schematically shown in Figure 2.3. The main field with the infrastructure region is followed by 7 emplacement fields, each field with 20 emplacement drifts for containers with spent fuel. It is assumed that in each emplacement field 4 brine pockets occur, 2 pockets connected to the drifts at the end of the field and 2 pockets connected to the drifts at the centre of the field. The infrastructure region of the main field is modelled as a drift system with an additional open void. The drifts are modelled as porous media with a flow resistance according to the permeability, and the additional voids are assumed to be accessible to brine but not contributing to the flow resistance.

Due to the symmetry as shown by the symmetry axis, a tree like structure of the near field can be modelled. The resulting structure is shown in Figure 2.4. The numbers for the emplacement fields refer to the time of the end of emplacement in that field after the beginning of operation of the repository, e. g. MD50 is the main drift along a field which is closed 50 y after the beginning of operation.

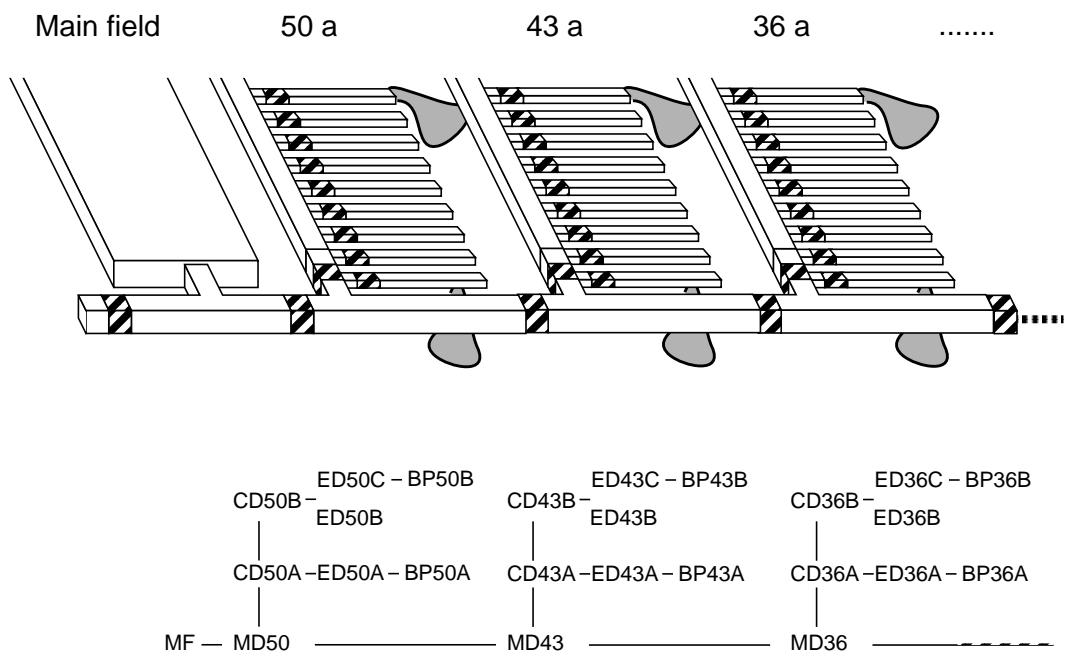


Fig. 2.4 Modelled section structure of the near field. MD: main drift; CD: connecting drift; ED: emplacement drift; BP: brine pocket

For long-term performance assessments, the repository structure is modelled by sections, each section representing a number of drifts. By use of the computer code REPOS6, the release rates from the waste packages followed by the transport through the entire structure up to the intersection to the geosphere are calculated. In the case of an accident, it is assumed that brine enters the emplacement site from outside and from the brine pockets, corrodes the waste containers, and leaches radionuclides from the waste. The first step in these release calculations is the calculation of container failure and mobilisation of radionuclides from the waste. After that, the processes within each emplacement section are calculated, including among others precipitation and radioactive decay of all radionuclides.

2.3.1 Source term for spent fuel elements

To calculate the release rates from the waste packages after contact to brine, the failure of waste containers, the mobilisation of radionuclides from the waste matrix, and the sorption and precipitation of radionuclides in the environment around the waste packages must be considered. The computer code REPOS calculates this release in two steps: mobilisation from the waste packages followed by sorption and precipitation. Container failure and mobilisation from the waste matrix are jointly calculated by source term models. Sorption is neglected in this project and precipitation is calculated in a model of the emplacement drift. In the following, the models of the source term and the precipitation are described.

2.3.1.1 Container failure

The failure of waste containers depends on the materials of the containers and the chemical and physical environment of the emplacement drift. For the direct disposal of spent fuel elements Pollux casks are used. These large casks are designed to withstand the petrostatic pressure in the depth of a repository and are highly resistant to the surrounding brine.

The relative number or fraction of failed containers at the time τ is calculated by

$$n_c(\tau) = \frac{N_c(\tau)}{N_c(0)} = F(\tau), \quad (6)$$

which is the distribution function $F(\tau)$ of the container lifetime. $N_c(\tau)$ is the actual number of failed containers in an emplacement drift at the time τ , $N_c(0)$ the total number of containers in the emplacement drift at the end of the operational phase of the repository.

The relative increase of failed containers per time step is

$$\dot{n}_c(\tau) = \frac{\dot{N}_c(\tau)}{N_c(0)} = f(\tau), \quad (7)$$

where $f(\tau)$ is the distribution density of the container lifetime. In the following, the density is called container failure rate. Furthermore, all the relative numbers refer to the total number of containers $N_c(0)$, so the supplement “relative” is omitted in the following.

The origin of the time scale $\tau = 0$ in the calculation of container failure is the time of brine intrusion into the emplacement drift. The time τ is related to the time scale t in the REPOS code by

$$\tau = t - t_b, \quad (8)$$

where t_b is the time of brine intrusion. The origin of the REPOS time scale $t = 0$ is the end of the operational phase of the repository. Negative values of τ cannot occur because the container failure is only calculated for times after brine intrusion.

For the large Pollux casks the failure rates are assumed to be distributed exponentially. The container failure rate and the amount of failed containers are obtained using the average lifetime τ_{ca} by the following equations:

$$\dot{n}_c(\tau) = \frac{1}{\tau_{ca}} \exp\left(-\frac{\tau}{\tau_{ca}}\right), \quad (9)$$

$$n_c(\tau) = 1 - \exp\left(-\frac{\tau}{\tau_{ca}}\right). \quad (10)$$

Figure 2.5 shows a schematic plot of these functions.

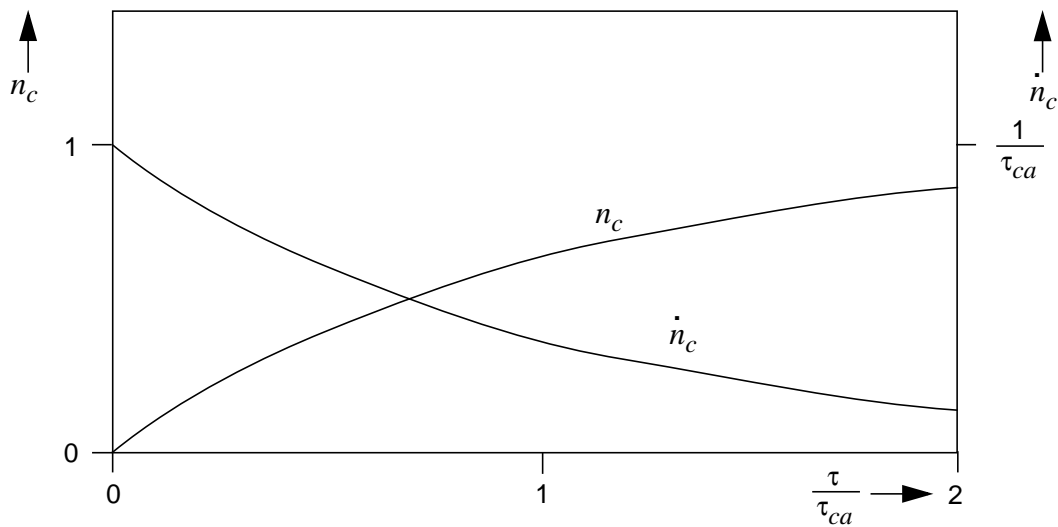


Fig. 2.5 Amount of failed containers n_c and container failure rate \dot{n}_c with exponential distribution of container failure rate

To give an example of the amount of failed containers, an average lifetime of 500 y is assumed. This is valid for Pollux casks and yields an amount of 2 % of failed containers after 10 y and 18 % after 100 y.

Although the container failure is a distinct process, it was shown in recent investigations [1] that a treatment of the container failure as a random process followed by a probabilistic assessment yields release rates out of an emplacement drift, which are almost the same as those calculated with the above described simple method.

2.3.1.2 Mobilisation from the waste matrix

After failure of a waste package, the spent fuel elements are leached by brine, and radionuclides are released. In the following, the release rates for spent fuel elements are given for the time t after closure of the repository.

In the calculation of the release of radionuclides from the fuel elements the barrier effect of the fuel rods is neglected. Therefore, the release starts immediately after the failure of the first container. The fuel elements are divided into three regions, for which the release rates are calculated individually. These regions are

- cladding,
- gas gap in the fuel rods,
- fuel matrix.

The cladding involves all the metallic parts of the fuel elements. Table 3.3 gives a summary of the fractions of the nuclide inventories in the regions. It can be seen that the actinides are especially present in the fuel matrix. The gas gap contains larger amounts of C, Cs and Zr. In the cladding only the elements C, Ni, Mo, Nb, Zr and Tc are present.

To describe the time-dependent release of radionuclides from the three regions X of the fuel element a common approach is used. This approach is based upon constant rates resulting in an activity flux which is a product of the relative release rates and the actual activity inventory. The actual inventory in this formula is the initial inventory in a cask after radioactive decay, neglecting the released amount. This inventory is distributed over the three regions according to the fractions given in table 3.3.

The release rates for the regions are added and then multiplied by the number of failed containers to yield the total release rate $S_i(t)$:

$$S_i(t) = n_c(\tau) \sum_X r_X a_{X,e} A_i(t). \quad (11)$$

r_X is the constant release rate in region X , $a_{X,e}$ the fraction of the inventory $A_i(t)$ of element $e(i)$ in the region X , and $n_c(\tau)$ is the number of failed containers at the time τ . In recent calculations [3], the constant release rates were assumed to have values of 0.1 y^{-1} for the gas gap, which describes an almost instantaneous release, 0.02 y^{-1} for the cladding, and 0.0016 y^{-1} for the fuel matrix. These values have been applied for the actual calculations too.

One essential simplification was applied in the assumptions to equation 11. There is no superposition of container failure and release from the fuel rods by a convolution of the appropriate functions. Instead of that, the constant rates and the relative number of failed containers are simply multiplied to yield the total release rate.

Figure 2.6 shows the cumulated release rates for the three regions of an LWR fuel element with Zr-93 as an example and container failure disregarded. The release in the gas gap ends after 10 years, in the cladding after 50 years and in the fuel matrix after 625 years. The sum of all the cumulated relative releases is 1 after 625 years.

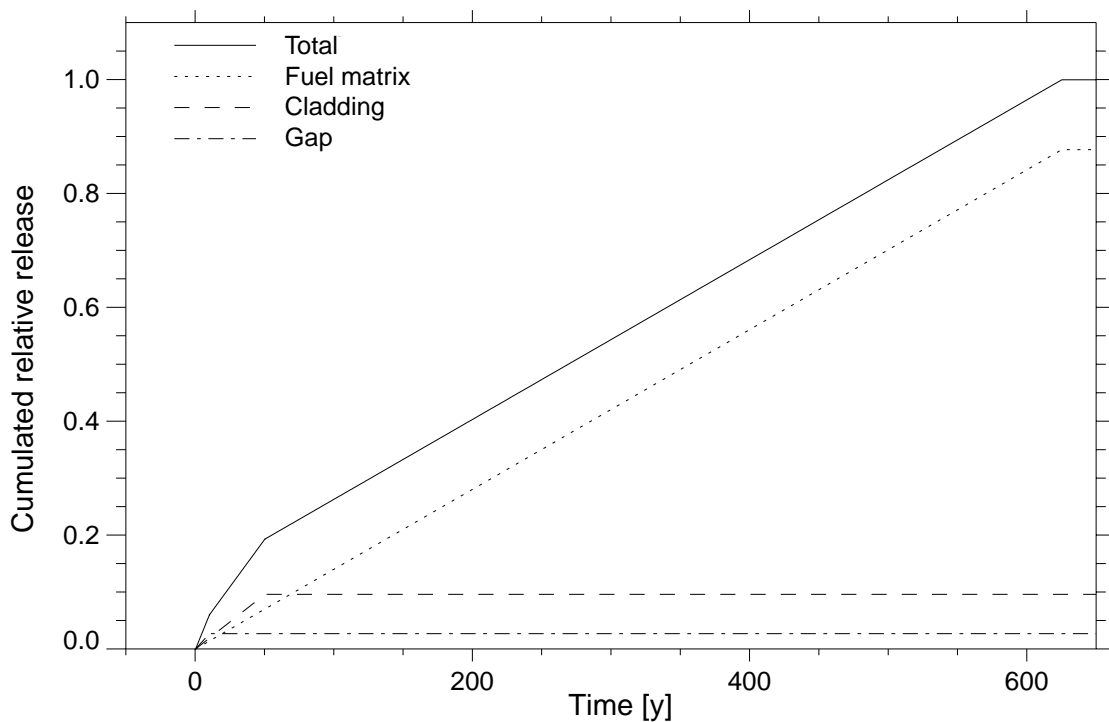


Fig. 2.6 Cumulated release rates of Zr-93 for the regions of LWR fuel elements

In Figure 2.7 the same release rates as in the previous figure are shown, but in this case an exponential failure rate of the containers and an average lifetime of 500 years is assumed. Due to the exponential increase in the number of failed containers, the relative release rates increase in time. The cumulated relative releases are the same as in the previous figure but the slope of the curves is different due to the exponential container failure rate.

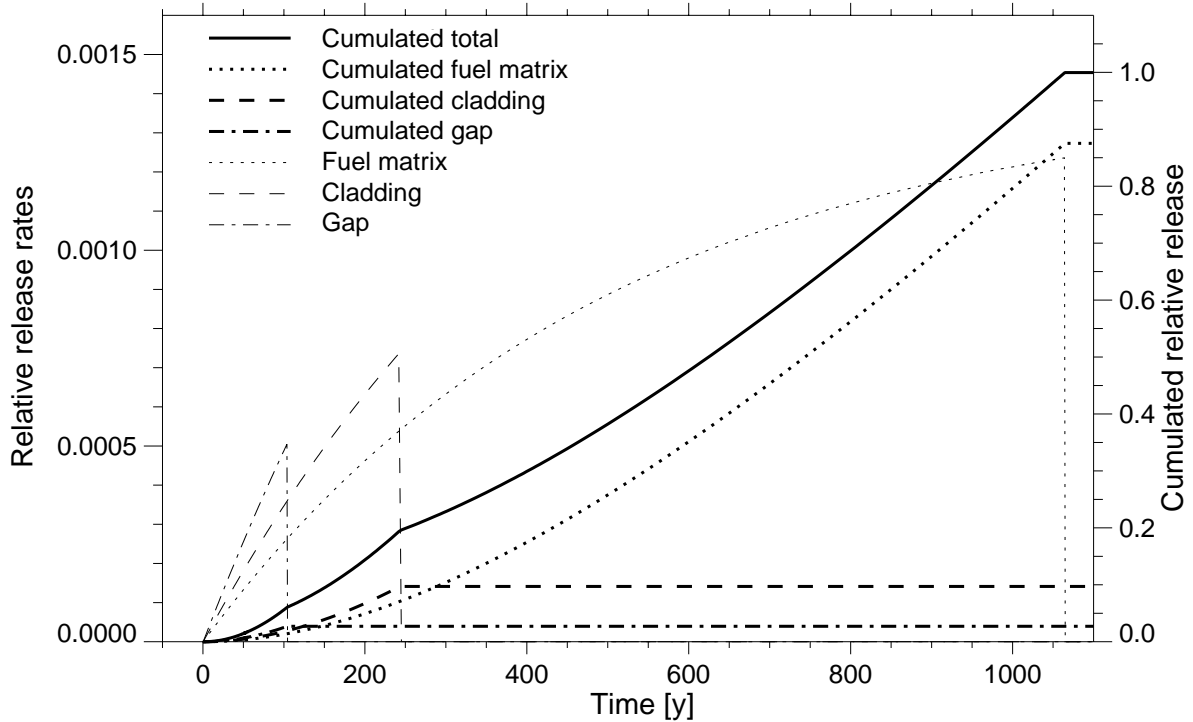


Fig. 2.7 Relative release rates (thin lines) and cumulated release (thick lines) of Zr-93 for different regions of an LWR fuel element

The total release rate $S_i(t)$ is calculated by the relative release rates, multiplied by the actual initial inventory. It gives the flux of radionuclides from the failed canisters of one emplacement drift. It gives no information about the release from the entire emplacement drift because precipitation is calculated in a later step in the subroutine for the emplacement drift. In the following Chapter 2.3.1.3 the procedure to calculate the precipitation of radionuclides is described.

2.3.1.3 Precipitation

Precipitation of radionuclides is modelled by solubility limits depending on the chemical properties of the brine. Due to the low amount of brine in a disposal site solubility limits can be reached soon after the beginning of the degradation of the waste forms, especially for low soluble elements. For the disposal sites the brine is assumed to be acidic which results in the solubility limits L_{empl} given in Table 3.3. The different chemical composition in other parts of the repository results in the solubility limits $L_{connect}$ in Table 3.3. If these limits are lower than in the emplacement drift they may cause further precipitation of some elements, but this effect is not relevant for the discussion of the source term. A detailed description of the models used for the calculation of precipitation is given in [8].

3 Input data

All the input data are based on those given in Refs. [4], [6] and [9]. The data for the geosphere and the biosphere are taken over without changes because the radiation exposures are calculated only as a tool to compare the results. The intention is to compare the influence of different fuel types, and this influence is only given for the near field. For the near field most of the data are taken from Ref. [4].

First, the data which are common to all scenarios are presented. Among these are:

- temperature data,
- container and fuel design data,
- the geometrical data of the repository,
- waste inventories,
- mobilisation data and element specific solubilities, and
- dose conversion factors.

Additional data concerning the geometry of the repository (i. e. the section systems of the repositories and the specific geometrical section data) and the sorption data are presented in Ref. [4]. Finally, specific data for each scenario are presented.

The subsidence scenario requires knowledge of the following data:

- time of the beginning of the release from the repository,
- salt mass in the emplacement area, and
- concentration of salt in drinking water.

For the human intrusion scenario, the following parameters are required:

- geometrical data (radius and height of the cavern and also of the cavity, and final pore volume of the cavity),
- maximum value of brine pressure,
- initial and reference value for the porosity of the sump, and
- time of spontaneous fill-up of the cavity.

Two more specific data are necessary for a complete description of the combined scenario. These are:

- time of brine intrusion from the anhydrite vein (unlimited brine intrusion), and
- time of brine intrusion from the brine pockets (limited brine intrusion).

3.1 General data for the repository system

3.1.1 Temperature data

In the following figures some representative temperature curves are shown which are used for the calculation of the convergence of backfilled drifts. These temperatures hold for the repository with spent LWR fuel elements. The numbers in the legends refer to the temperature curves in [4]. In the case of CANDU fuel, all temperatures are lower by a constant factor of 0.4.

The highest temperatures occur within the emplacement drifts. This results in a fast closure of these drifts if no brine intrudes into them. Intruding brine would support the internal pressure and reduce the convergence process.

The lowest temperatures occur in the main drift along the side of the emplacement fields. These relatively low temperatures are responsible for a longer period of open segments, so that brine can intrude into them even at times later than 100 y after the operational phase of the repository.

The emplacement fields at the centre of the near field exhibit the highest temperatures because a superposition of temperature fields occurs.

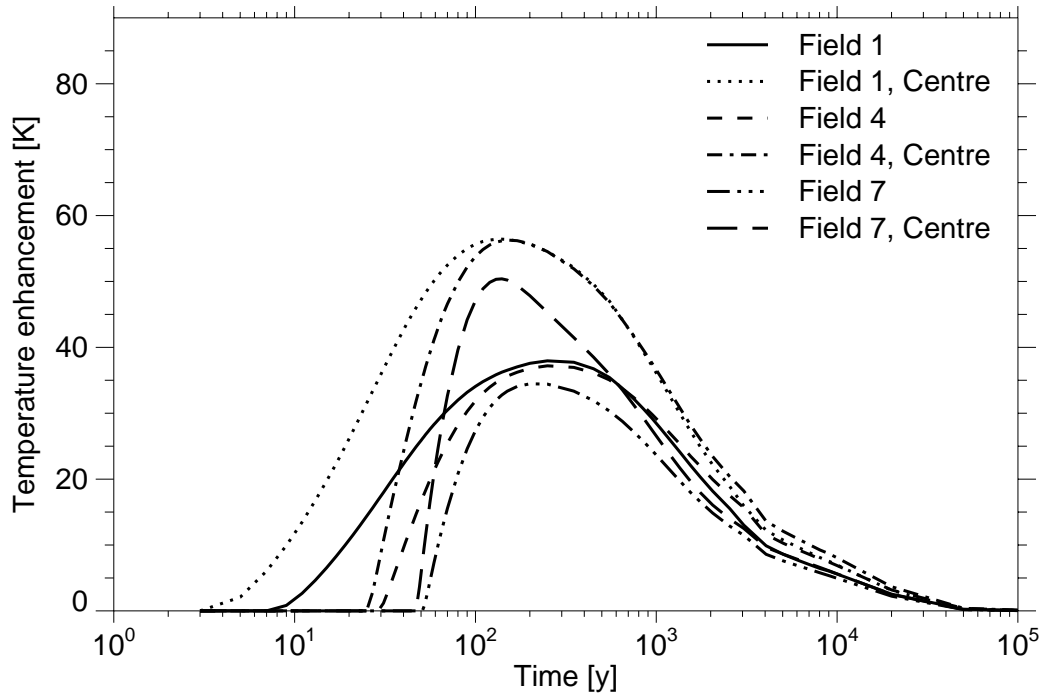


Fig. 3.1 Temperature curves for calculation of convergence of brine pockets

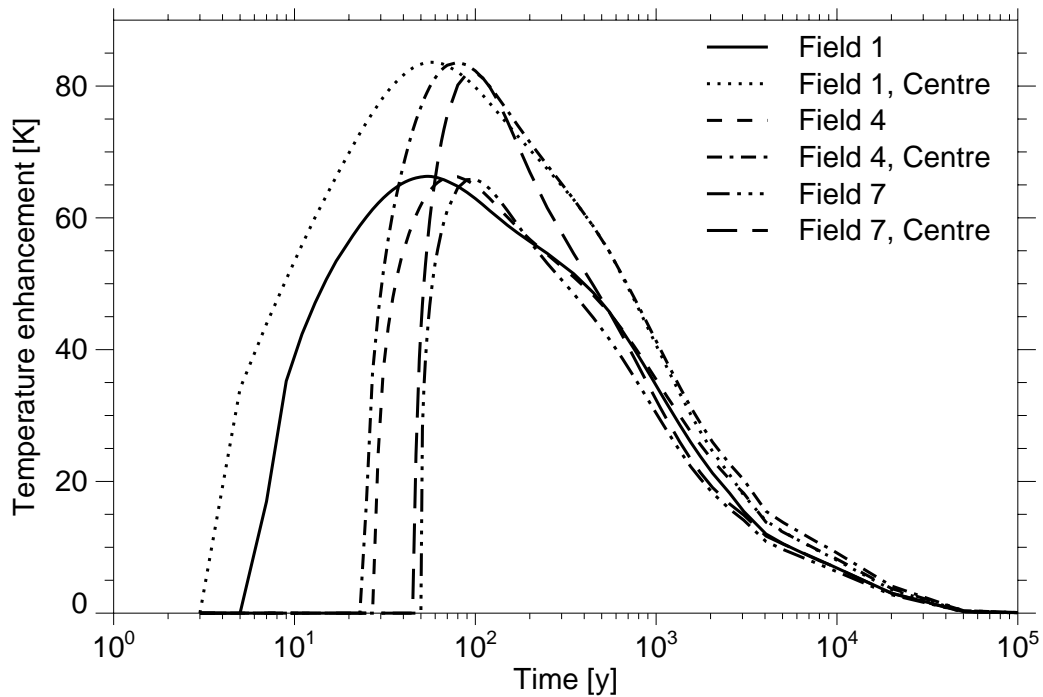


Fig. 3.2 Temperature curves for calculation of convergence of backfill of emplacement drifts

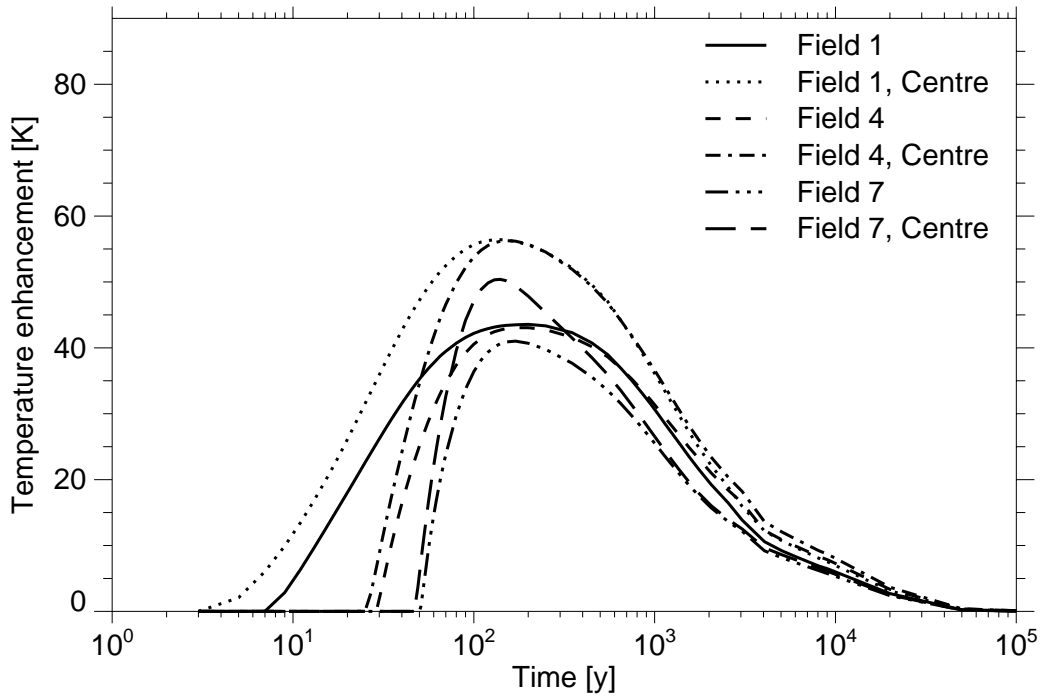


Fig. 3.3 Temperature curves for calculation of convergence of backfill in connecting drifts

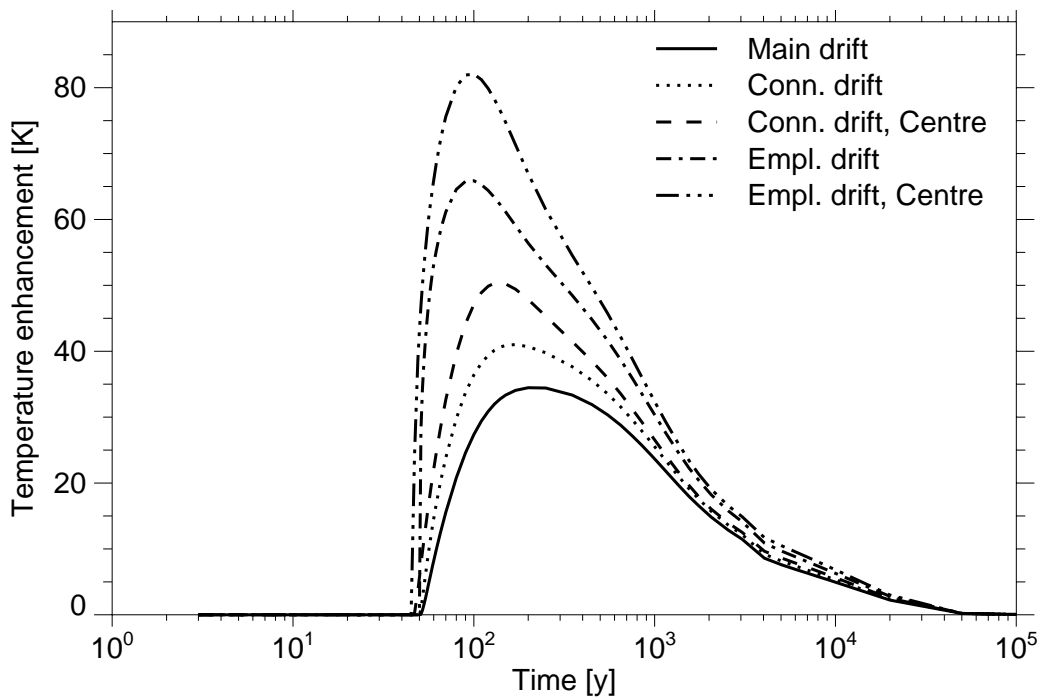


Fig. 3.4 Comparison of temperature curves for calculation of convergence of the segments of emplacement field 7

3.1.2 Design data

In Table 3.1 the relevant design data are given for both fuel types. The initial amount of fuel in the CANDU variant is about 2 times higher than in the LWR variant. Also, the number of Pollux containers is about 2 times higher. But the lengths of the emplacement drifts are assumed to be the same. This is possible by arranging the containers with different spacings. The narrow arrangement in the case of CANDU fuel is justified by its low heat production, as discussed in the following.

Table 3.1 Design data

	LWR	CANDU
Burn-up [GWd/t _U]	45	7.93
Initial amount of fuel [kg uranium]	$1.02 \cdot 10^7$	$2.74 \cdot 10^7$
Number of spent fuel elements	19 040	1 445 220
Number of Pollux containers:		
- total	2 380	4 340
- per drift	17	31
Cooling time after discharge [y]	30	10

In Figure 3.5 the heat production rates of containers with either spent LWR or spent CANDU fuel are compared. The heat production of spent CANDU fuel is generally lower. At the respective emplacement time (10 y after discharge for CANDU and 30 y after discharge for LWR), the heat output of one emplacement drift with spent LWR fuel is 2.5 times higher than for CANDU fuel. From this observation it is assumed that all the temperatures in a repository with CANDU fuel are lower by a factor of 0.4 than the respective temperatures in a repository with LWR fuel. This assumption is necessary because only temperature calculations for repositories with LWR fuel are available.

The disposed waste from CANDU nuclear power plants are fuel bundles of CANDU type exclusively. For LWR the fuel bundles are of UO₂ type only, i. e. without mixed oxide (MOX). The sources for radio toxic elements in both spent fuel types are activation and fission products from the UO₂ matrix, activation products from the Zircaloy sheath and activation products from impurities in both the fuel and the Zircaloy sheath.

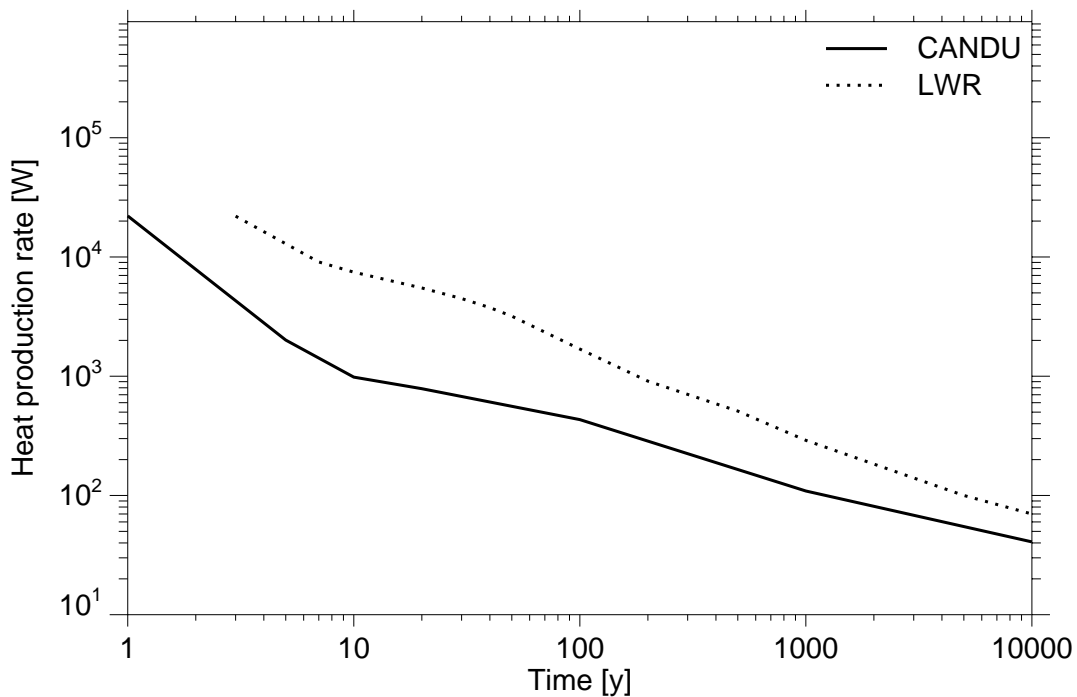


Fig. 3.5 Comparison of heat production rate of one container with CANDU or LWR fuel, resp. for times after discharge from the reactor

3.1.3 Waste inventories

The inventories of a Pollux container are given in Table 3.2. For CANDU it was calculated for the reference 10 years-cooled Bruce reactor fuel [9]. Of the total number of radionuclides, only seventeen fission and activation products and four actinide decay chains are examined in the present study.

Considering the source term, the mobilisation process is dominated by the almost instant release of some radionuclides. In the case of CANDU fuel, the inventory fractions for instant release of some radionuclides including C-14, Cl-36, Se-79, Sr-90, Tc-99, Sn-126, I-129, Cs-135, and Cs-137 are taken from Ref. [5]. In the case of LWR fuel, the inventory fractions are taken from Ref. [4].

Table 3.2 Initial radionuclide inventories per container in Bq for 30 y old spent LWR and 10 y old spent CANDU fuel

CANDU:							
C- 14	3.162·10 ⁺¹¹	Ca- 41	1.067·10 ⁺⁰⁹	Ni- 59	5.074·10 ⁺⁰⁹	Co- 60	6.269·10 ⁺¹³
Se- 79	2.102·10 ⁺¹⁰	Rb- 87	1.124·10 ⁺⁰⁶	Sr- 90	4.110·10 ⁺¹⁵	Zr- 93	1.090·10 ⁺¹¹
Nb- 94	2.612·10 ⁺⁰⁹	Tc- 99	7.955·10 ⁺¹¹	Pd-107	6.502·10 ⁺⁰⁹	Sn-126	3.270·10 ⁺¹⁰
I-129	1.780·10 ⁺⁰⁹	Cs-134	3.529·10 ⁺¹⁵	Cs-135	6.237·10 ⁺⁰⁹	Ba-137	5.814·10 ⁺¹⁵
Cs-137	6.073·10 ⁺¹⁵	Sm-147	3.295·10 ⁺⁰⁴	Cm-247	1.408·10 ⁺⁰¹	Cm-246	1.345·10 ⁺⁰⁷
Cm-245	7.702·10 ⁺⁰⁷	Po-210	6.692·10 ⁻⁰²	Cm-243	4.204·10 ⁺¹⁰	Am-243	1.218·10 ⁺¹¹
Am-242	5.328·10 ⁺¹⁰	Am-241	1.357·10 ⁺¹²	Pu-244	3.548·10 ⁺⁰³	Pu-242	5.562·10 ⁺¹⁰
Pu-241	5.417·10 ⁺¹⁵	Pu-240	5.492·10 ⁺¹³	Pu-239	3.832·10 ⁺¹³	Pu-238	1.843·10 ⁺¹³
Pu-236	4.905·10 ⁺⁰⁹	Np-237	5.840·10 ⁺⁰⁹	U-238	7.702·10 ⁺¹⁰	U-236	1.162·10 ⁺¹⁰
U-235	1.016·10 ⁺⁰⁹	U-234	6.237·10 ⁺¹⁰	U-233	2.096·10 ⁺⁰⁵	U-232	2.475·10 ⁺⁰⁷
Th-232	2.127·10 ⁻⁰¹	Th-230	3.460·10 ⁺⁰⁵	Th-229	3.573·10 ⁺⁰¹	Th-228	1.730·10 ⁺⁰⁶
Pb-210	3.226·10 ⁻⁰¹	Ac-227	9.975·10 ⁺⁰²	Ra-228	5.745·10 ⁻⁰³		
LWR:							
C- 14	1.964·10 ⁺¹¹	Co- 60	1.739·10 ⁺¹⁵	Ni- 59	2.170·10 ⁺¹²	Ni- 63	2.920·10 ⁺¹⁴
Se- 79	7.870·10 ⁺¹⁰	Rb- 87	4.340·10 ⁺⁰⁶	Sr- 90	1.300·10 ⁺¹⁶	Zr- 93	4.155·10 ⁺¹¹
Nb- 94	3.630·10 ⁺¹¹	Mo- 93	1.803·10 ⁺¹⁰	Tc- 99	2.683·10 ⁺¹²	Pd-107	2.374·10 ⁺¹⁰
Sn-126	1.228·10 ⁺¹¹	I-129	6.835·10 ⁺⁰⁹	Cs-135	7.647·10 ⁺¹⁰	Cs-137	1.935·10 ⁺¹⁶
Sm-147	8.590·10 ⁺⁰⁵	Sm-151	5.947·10 ⁺¹³	Eu-154	1.723·10 ⁺¹⁵	Cm-248	1.243·10 ⁺⁰⁶
Pu-244	1.853·10 ⁺⁰⁵	Cm-244	7.074·10 ⁺¹⁴	Pu-240	1.027·10 ⁺¹⁴	U-236	5.101·10 ⁺¹⁰
Th-232	2.323·10 ⁺⁰¹	U-232	1.083·10 ⁺¹⁰	Cm-245	7.271·10 ⁺¹⁰	Pu-241	1.758·10 ⁺¹⁶
Am-241	2.609·10 ⁺¹⁴	Np-237	7.156·10 ⁺¹⁰	U-233	1.326·10 ⁺⁰⁷	Th-229	4.169·10 ⁺⁰⁴
Cm-246	1.816·10 ⁺¹¹	Pu-242	4.926·10 ⁺¹¹	Am-242	7.912·10 ⁺¹¹	U-238	4.943·10 ⁺¹⁰
Pu-238	7.143·10 ⁺¹⁴	U-234	1.471·10 ⁺¹¹	Th-230	1.136·10 ⁺⁰⁷	Ra-226	2.422·10 ⁺⁰⁴
Pb-210	0.000·10 ⁺⁰⁰	Cm-247	3.989·10 ⁺⁰⁵	Am-243	5.673·10 ⁺¹²	Pu-239	5.669·10 ⁺¹³
U-235	2.070·10 ⁺⁰⁹	Pa-231	5.605·10 ⁺⁰⁶				

3.1.4 Mobilisation data and solubility limits

The inventory fractions of the regions of fuel elements and the solubility limits are given in Table 3.3. The release of some radionuclides is limited by precipitation within the emplacement drifts. For elements expected to be highly soluble (including I and Cs) and for those for which the chemistry in natural systems is complex to predict or is not well

understood (including Rh, Po, Ac, Ra and Cf), the solubility limit was assigned a conservatively high value of 1 mol/l.

Table 3.3 Fractions of the inventories of selected elements in the cladding a_C , the gas gap a_G , and the fuel matrix a_F . Solubility limits L in emplacement drifts and connecting drifts (mol/l). *: values for CANDU fuel

Element	a_C	a_G	a_F	$L_{empl.}$	$L_{connect.}$
C	1.0 (0.973 *)	0.0 (0.027 *)	0.0	1.0	$1.0 \cdot 10^{-4}$
Rh *	0.0	0.0	1.0	1.0	$1.0 \cdot 10^{-4}$
Ba *	0.0	0.0	1.0	$1.0 \cdot 10^{-2}$	$1.0 \cdot 10^{-4}$
Po, Ac, Ra, Cf *	1.0	0.0	0.0	1.0	1.0
Co	0.92	0.08	0.0	$1.0 \cdot 10^{-2}$	$1.0 \cdot 10^{-4}$
Se	0.0	0.01 (0.08 *)	0.99 (0.92 *)	$1.0 \cdot 10^{-4}$	$1.0 \cdot 10^{-4}$
Sr	0.0	0.01 (0.025 *)	0.99 (0.975 *)	$1.0 \cdot 10^{-3}$	$1.0 \cdot 10^{-3}$
Zr	0.096	0.027	0.877	$1.0 \cdot 10^{-6}$	$1.0 \cdot 10^{-7}$
Tc	0.001	0.015 (0.06 *)	0.984 (0.939 *)	$1.0 \cdot 10^{-4}$	$1.0 \cdot 10^{-4}$
Ni, Mo, Nb	0.999	0.001	0.0	$1.0 \cdot 10^{-2}$	$1.0 \cdot 10^{-4}$
Pd, Sn	0.0	0.015	0.985	$1.0 \cdot 10^{-2}$	$1.0 \cdot 10^{-4}$
I	0.0	0.015 (0.08 *)	0.985 (0.92 *)	1.0	1.0
Rb	0.0	0.05	0.95	1.0	1.0
Cs	0.0	0.05 (0.08 *)	0.95 (0.92 *)	1.0	1.0
Sm, Eu	0.0	0.01	0.99	$1.0 \cdot 10^{-2}$	$1.0 \cdot 10^{-4}$
Cm, Am	0.0	0.008	0.992	$1.0 \cdot 10^{-4}$	$1.0 \cdot 10^{-5}$
Pu, Pa, Th	0.0	0.008	0.992	$1.0 \cdot 10^{-6}$	$1.0 \cdot 10^{-7}$
Np	0.0	0.008	0.992	$1.0 \cdot 10^{-5}$	$1.0 \cdot 10^{-6}$
U	0.0	0.008	0.992	$1.0 \cdot 10^{-4}$	$1.0 \cdot 10^{-4}$
Ra	0.0	0.008	0.992	$1.0 \cdot 10^{-5}$	$1.0 \cdot 10^{-5}$

3.1.5 Dose conversion factors

The best estimate values for the effective dose conversion factors are listed in Table 3.4.

Table 3.4 Dose conversion factors

Nuclide	Dose conversion factors [(Sv/y)/(Bq/m ³)]	Nuclide	Dose conversion factors [(Sv/y)/(Bq/m ³)]
C- 14	$5.9 \cdot 10^{-8}$	Cm-245	$3.5 \cdot 10^{-7}$
Cl- 36	$9.5 \cdot 10^{-9}$	Am-241	$3.4 \cdot 10^{-7}$
Ca- 41	$1.9 \cdot 10^{-9}$	Np-237	$7.5 \cdot 10^{-7}$
Ni- 59	$5.4 \cdot 10^{-11}$	U-233	$4.7 \cdot 10^{-8}$
Se- 79	$6.1 \cdot 10^{-10}$	Th-229	$6.7 \cdot 10^{-7}$
Rb- 87	$4.1 \cdot 10^{-9}$		
Sr- 90	$2.6 \cdot 10^{-8}$	Pu-242	$3.2 \cdot 10^{-7}$
Zr- 93	$2.4 \cdot 10^{-10}$	U-238	$4.2 \cdot 10^{-8}$
Mo- 93	$3.8 \cdot 10^{-10}$	Th-234	$8.39 \cdot 10^{-9}$
Nb- 94	$1.6 \cdot 10^{-9}$	U-234	$4.6 \cdot 10^{-8}$
Tc- 99	$6.3 \cdot 10^{-10}$	Th-230	$1.1 \cdot 10^{-7}$
Pd-107	$5.4 \cdot 10^{-11}$	Ra-226	$1.8 \cdot 10^{-7}$
Sn-126	$4.6 \cdot 10^{-9}$	Pb-210	$9.1 \cdot 10^{-7}$
I-129	$2.1 \cdot 10^{-7}$	Po-210	$4.26 \cdot 10^{-6}$
Cs-135	$3.7 \cdot 10^{-9}$		
Cs-137	$2.1 \cdot 10^{-8}$	Cm-247	$3.2 \cdot 10^{-7}$
Sm-147	$3.0 \cdot 10^{-8}$	Am-243	$3.4 \cdot 10^{-7}$
		Pu-239	$3.5 \cdot 10^{-7}$
Cm-248	$1.3 \cdot 10^{-6}$	U-235	$4.5 \cdot 10^{-8}$
Pu-244	$3.2 \cdot 10^{-7}$	Pa-231	$2.0 \cdot 10^{-6}$
Pu-240	$3.5 \cdot 10^{-7}$	Ac-227	$2.2 \cdot 10^{-6}$
U-236	$4.4 \cdot 10^{-8}$	Th-227	$2.23 \cdot 10^{-8}$
Th-232	$5.4 \cdot 10^{-7}$	Ra-223	$3.48 \cdot 10^{-7}$
Ra-228	$1.20 \cdot 10^{-6}$		
Th-228	$3.08 \cdot 10^{-7}$		

3.2 Specific data

3.2.1 Subrosion scenario

In the following, the input data for the subrosion scenario and their ranges of values are discussed. All the input data are outlined in two tables. In Table 3.5, the specific input data, i. e. the moment of release, the concentration of salt in drinking water, and the mass of salt within the repository field are given.

Table 3.5 Specific input data for the subrosion scenario

Parameter	Best estimate value	Distribution	3- σ range
Mass of salt in the repository field	$1.29 \cdot 10^{10}$ kg	constant	-
Concentration of salt in drinking water	$3.1 \cdot 10^{-5}$ kg/l	log normal	$10^{-6} - 10^{-3}$ kg/l
Moment of release	$1.5 \cdot 10^7$ y	log normal	$2.25 \cdot 10^5 - 10^9$ y

The moment of release results from the time period required for water to dissolve the salt rock down to the repository level until the release of radionuclides starts.

The concentration of salt in drinking water can vary over a wide range. Waters with higher salt content, like mineral waters, are of course drinkable but these are not suitable for a person's exclusive drinking requirements. The geological fresh-water limit is set to 1 kg/m^3 as most fresh-water plants and animals can tolerate this concentration.

To calculate the nuclide concentrations in the saturated brine under the assumption of congruent dissolution of rock salt, the amount of salt in the emplacement field must be known. The dimensions of this field, especially the length and the height, are a little bit overestimated in order to take into account the distortion of it due to the creep movement of salt. The width of the disposal field is about 300 m, the length is assumed to be 2 000 m and the height is taken to be 10 m, almost three times higher than the actual height of 3.3 m. The resulting volume is $6 \cdot 10^6 \text{ m}^3$. With a salt rock density of $2\,150 \text{ kg/m}^3$, the total mass of salt in the spent fuel disposal area is $1.29 \cdot 10^{10}$ kg.

Table 3.6 Input data for the subrosion scenario

Parent nuclide	Daughter nuclide	Half-life [y]	Initial inventory (CANDU fuel) [Bq]	Initial inventory (LWR fuel) [Bq]	Rf best estimate [-]	r_s [-]	d_e best estimate [(Sv/y)/(Bq/m ³)]	$r_s \cdot d_e$ absolute [(Sv/y)/(Bq/m ³)]	$r_s \cdot d_e$ relative [%]
Rb-87		$4.70 \cdot 10^{10}$	$4.88 \cdot 10^{09}$	$1.03 \cdot 10^{10}$	11		$4.10 \cdot 10^{-09}$		
Zr-93		$1.53 \cdot 10^{06}$	$4.73 \cdot 10^{14}$	$9.89 \cdot 10^{14}$	1001		$2.40 \cdot 10^{-10}$		
Tc-99		$2.13 \cdot 10^{05}$	$3.45 \cdot 10^{15}$	$6.39 \cdot 10^{15}$	71		$6.30 \cdot 10^{-10}$		
Pd-107		$6.50 \cdot 10^{06}$	$2.82 \cdot 10^{13}$	$5.65 \cdot 10^{13}$	101		$5.40 \cdot 10^{-11}$		
I-129		$1.57 \cdot 10^{07}$	$7.73 \cdot 10^{12}$	$1.63 \cdot 10^{13}$	6		$2.10 \cdot 10^{-07}$		
Cs-135		$2.30 \cdot 10^{06}$	$2.71 \cdot 10^{13}$	$1.82 \cdot 10^{14}$	11		$3.70 \cdot 10^{-09}$		
Sm-147		$1.07 \cdot 10^{11}$	$1.43 \cdot 10^{08}$	$2.04 \cdot 10^{09}$	10000		$3.00 \cdot 10^{-08}$		
Pu-244		$8.27 \cdot 10^{07}$	$1.54 \cdot 10^{07}$	$4.41 \cdot 10^{08}$	10000		$3.20 \cdot 10^{-07}$	$3.20 \cdot 10^{-07}$	47.8
	Pu-240	$6.54 \cdot 10^{03}$	$2.38 \cdot 10^{17}$		10000	1	$3.50 \cdot 10^{-07}$	$3.50 \cdot 10^{-07}$	52.2
	U-236	$2.34 \cdot 10^{07}$	$5.05 \cdot 10^{13}$	$1.21 \cdot 10^{14}$	21		$4.40 \cdot 10^{-08}$		
	Th-232	$1.41 \cdot 10^{10}$	$2.58 \cdot 10^{04}$	$1.93 \cdot 10^{05}$	3001		$5.40 \cdot 10^{-07}$		
Effective dose conversion factor for Pu-244:							$6.70 \cdot 10^{-07}$		
Np-237		$2.14 \cdot 10^{06}$	$2.53 \cdot 10^{13}$	$1.70 \cdot 10^{14}$	301		$7.50 \cdot 10^{-07}$		
	U-233	$1.59 \cdot 10^{05}$	$2.02 \cdot 10^{09}$	$4.87 \cdot 10^{10}$	21		$4.70 \cdot 10^{-08}$	$4.70 \cdot 10^{-08}$	90.9
	Th-229	$7.34 \cdot 10^{03}$	$1.54 \cdot 10^{06}$		3001	0.007	$6.70 \cdot 10^{-07}$	$4.69 \cdot 10^{-09}$	9.1
Effective dose conversion factor for U-233:							$5.17 \cdot 10^{-08}$		

Table 3.6 Input data for the subrosion scenario

Parent nuclide	Daughter nuclide	Half-life [y]	Initial inventory (CANDU fuel) [Bq]	Initial inventory (LWR fuel) [Bq]	Rf best estimate [-]	r_s [-]	d_e best estimate [(Sv/y)/(Bq/m ³)]	$r_s \cdot d_e$ absolute [(Sv/y)/(Bq/m ³)]	$r_s \cdot d_e$ relative [%]
Pu-242		$3.87 \cdot 10^{05}$	$2.41 \cdot 10^{14}$	$1.17 \cdot 10^{15}$	10 000		$3.20 \cdot 10^{-07}$		
U-238		$4.47 \cdot 10^{09}$	$3.34 \cdot 10^{14}$	$1.18 \cdot 10^{14}$	21		$4.20 \cdot 10^{-08}$		
U-234		$2.45 \cdot 10^{05}$	$2.73 \cdot 10^{14}$	$3.50 \cdot 10^{14}$	21	1	$4.60 \cdot 10^{-08}$	$4.60 \cdot 10^{-08}$	10.83
	Th-230	$7.71 \cdot 10^{04}$	$2.60 \cdot 10^{10}$		3 001	0.007	$1.10 \cdot 10^{-07}$	$7.70 \cdot 10^{-10}$	0.18
	Ra-226	$1.60 \cdot 10^{03}$	$5.93 \cdot 10^{07}$		10	2	$1.80 \cdot 10^{-07}$	$3.78 \cdot 10^{-07}$	88.99
Effective dose conversion factor for U-234:								$4.25 \cdot 10^{-07}$	
Cm-247		$1.56 \cdot 10^{07}$	$6.11 \cdot 10^{04}$	$9.49 \cdot 10^{08}$	10 000		$3.20 \cdot 10^{-07}$	$3.20 \cdot 10^{-07}$	48.48
	Am-243	$7.39 \cdot 10^{03}$	$5.28 \cdot 10^{14}$		10 000	1	$3.40 \cdot 10^{-07}$	$3.40 \cdot 10^{-07}$	51.52
Effective dose conversion factor for Cm-247:								$6.60 \cdot 10^{-07}$	
U-235		$7.04 \cdot 10^{08}$	$4.41 \cdot 10^{12}$	$4.93 \cdot 10^{12}$	21		$4.50 \cdot 10^{-08}$	$4.50 \cdot 10^{-08}$	91.46
	Pa-231	$3.28 \cdot 10^{04}$	$9.32 \cdot 10^{08}$		10 000	0.002	$2.00 \cdot 10^{-06}$	$4.20 \cdot 10^{-09}$	8.54
Effective dose conversion factor for U-235:								$4.92 \cdot 10^{-08}$	

Sorption causes a shift in dissolved concentrations of short-lived daughters in relation to those of the long-lived parents. A detailed description of this effect is given in the PAGIS report [6]. Long-lived nuclides are assumed to be those with half lives above 100 000 y. The considered short-lived daughter nuclides with longest half lives are: Pu-240 (6 500 y), Th-229 (7 300 y), Th-230 (77 000 y), Ra-226 (1 600 y), Am-243 (7 400 y) and Pa-231 (32 800 y). In the following results only the long-lived nuclides are regarded but they comprise the short-lived nuclides due to the concept of effective dose conversion factors.

The change in the nuclide concentrations of short-lived daughters compared to long-lived parents caused by sorption effects is described by correction factors r_s . Calculation of these factors is based on the retardation coefficients Rf of the individual nuclides. A porosity of 0.2 and a rock density of 2 500 kg/m³ are used for the calculation of the retardation coefficients. The values for r_s in Table 3.6 cover a range from 0.002 to 2. The initial waste inventories of the emplacement field, the retardation factors Rf and the dose conversion factors d_e are also given in Table 3.6. The relative values of the product $r_s \cdot d_e$ relate to the sum over all nuclides which are in activity equilibrium. It can be seen, for example, that the short-lived nuclide Ra-226 makes a dominant contribution to radiation exposure after migration of the parent U-234.

3.2.2 Human intrusion scenario

All geometric data of the cavern, its location in the salt dome and the values of the hydrostatic and petrostatic pressures are presented in Figure 3.6. The top of the salt dome is assumed to be about 300 m below ground. The top of the cavern is located 150 m below the top of the salt dome and the entire vertical extension of the cavern is 500 m. The total height of the sump is 31 m, corresponding to 5 weight % of insolubles with a porosity of 0.4. The affected disposal gallery horizon is at 870 m. The total volume of the cavern is 10⁶ m³.

The best estimate values of the specific parameters and some limits for parameter variations used for the cavern scenario are listed in Table 3.7.

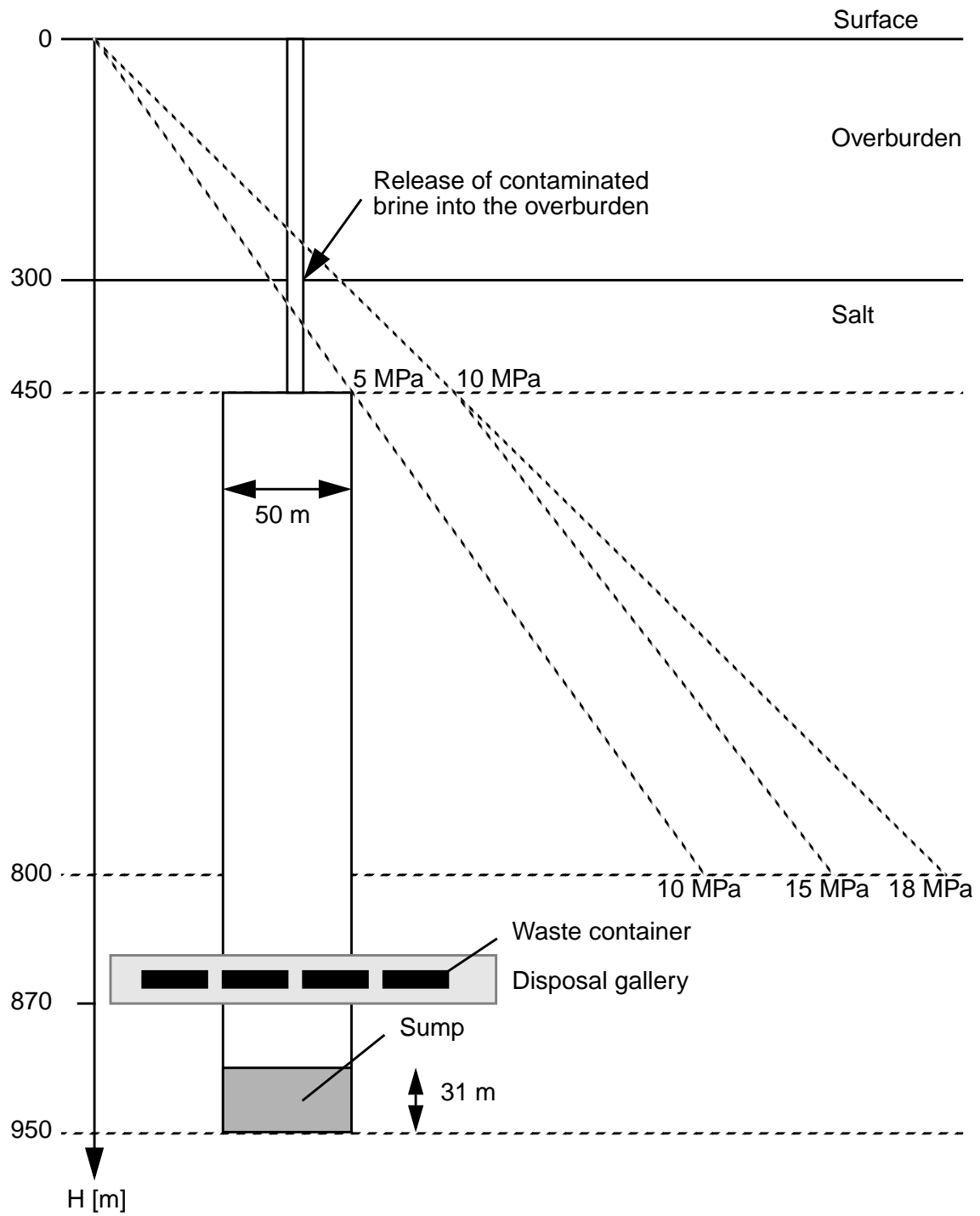


Fig. 3.6 Sketch of the cavern system. Adapted from [6]

Table 3.7 Selected input parameters for the human intrusion scenario. *) 3σ interval

Parameter	Dimension	Best est. value	Lower bounds	Upper bounds	Distribution function
Reference value of the convergence rate K_r	1/a	0.01	$1.38 \cdot 10^{-4}$	0.725*)	log normal
Coefficient of diffusion $D(T_0)$	m^2/s	$1.5 \cdot 10^{-9}$	$5.03 \cdot 10^{-11}$	$4.47 \cdot 10^{-8}$	log normal
Exponent in permeability-porosity relation q	-	4.5	3.25	6.23*)	log normal
Variation factor for permeability f_p	-	1.0			
Initial porosity of sump ϕ	-	0.4			
Final porosity ϕ_e	-	0.001			
Radius of the cavern	m	25.0			
Height of the cavern	m	500.0			
Volume of the cavern	m^3	10^6			
Height of the sump (bottom half)	m	15.5			
Height of the sump (upper half)	m	15.5			
Height of the cavity	m	469.0			
Initial and reference porosity of the insolubles	-	0.4			
Reference point below the surface	m	870			
Maximum value of brine pressure	MPa	15.0			

The hydrostatic and petrostatic pressures within the cavern are calculated for the reference level which is located at 800 m. All input data are relative to this level. The hydrostatic pressure corresponding to the 800 m level is 10 MPa (i. e. $\Delta p = 0.012$ MPa/m) and the petrostatic pressure at the same level is 18 Mpa (i.e. $\Delta p = 0.023$ MPa/m).

As derived from Figure 3.7, 28 containers fall into the sump if spent CANDU fuel is considered as disposed waste. In the LWR case, only 16 containers are affected by solution mining. This difference is due to the spacings of the containers, which are dictated by temperature considerations. As discussed in Chapter 3.1.1, spent CANDU fuel produces less heat per container than the LWR fuel, and, as a consequence, the containers can be arranged closer to each other.

The scenario starts at $t = 0$ years with the mining of the cavern, cf. Figure 3.8. At that time, the containers are partially destroyed and corroded, and therefore their barrier function is neglected.

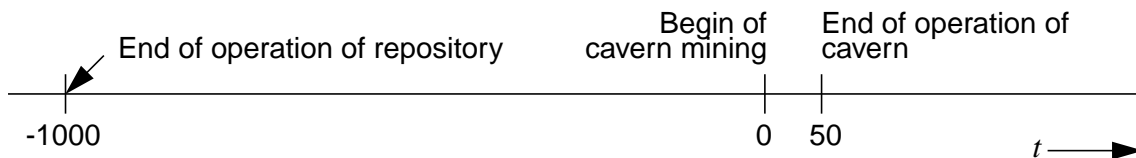


Fig. 3.8 Time scale of the cavern scenario

The time period between the operational phase of the ancient repository and the solution mined cavern is assumed to be 1 000 y. This time was chosen as a compromise between two conservative demands. First, the onset of the scenario should be set to a late time point at which the heat production, even in the hottest region of the repository, is negligible. Secondly, an early time should be chosen if the radionuclide inventory is taken as a criterion, which is reduced in time. At 1 000 y, the heat generation by waste is low, so the temperatures in the cavity and sump will be close to that of the host rock. The host rock temperature at the reference level is about 310 K.

For simplicity it is assumed that the containers fall into the sump right from the beginning of the scenario. The mining of the cavern takes about 1 y, a period which is neglected due to the much longer time frame of the entire scenario. Hence, in the model the brine above the sump is replaced by the stored medium at $t = 0$ y. The operational phase of the cavern is supposed to last for about 50 y until the cavern is abandoned. The stored medium is not explicitly modelled, but its presence sets the pressure in the cavity to a value that corresponds to the hydrostatic pressure. Since the sump remains filled with brine, the leaching of the waste matrices starts immediately.

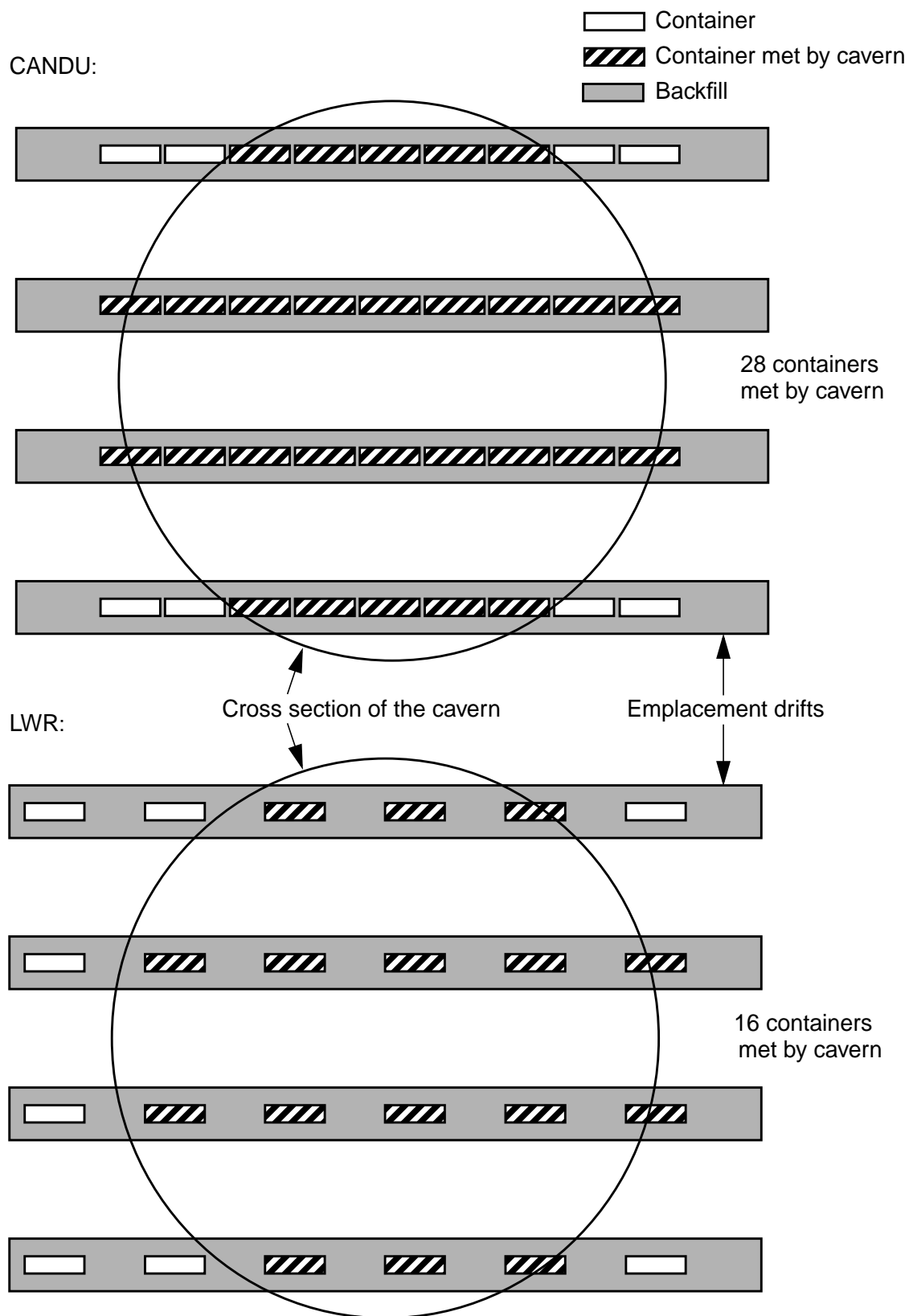


Fig. 3.7 Estimation of affected containers by the solution mining of the cavern

At $t = 50$ y the stored medium will be replaced by brine and a leakage from the cavern is assumed as described in Chapter 2.2. The value of the permeability of the leakage pathway is assumed to be a value which corresponds to the condition that the hydraulic pressure equals the petrostatic pressure at the top of the cavern. With 10 MPa petrostatic pressure and 5 MPa hydrostatic pressure at the top of the cavern, the hydraulic pressure has to rise 5 MPa above hydrostatic pressure. Then, the hydraulic pressure at the 800 m level is 15 MPa. This value is used as the maximum pressure p_{max} in the reference calculations.

The release of contaminants into the overburden starts immediately at the end of the operational period at $t = 50$ y. At that time the former access borehole opens a contact between the surface of the salt dome and the cavern. The inventories of the waste containers, the modelling of the mobilisation, the solubility limits, the migration pathway through the overburden, and the dose conversion factors are general data and have already been described in Chapter 3.1.

3.2.3 Combined accident scenario

Besides the general data, a complete description of the combined scenario requires the knowledge of the following parameter values:

- time of water intrusion from the anhydrite vein: 85 years,
- time of water intrusion from the brine pockets: 0 years (immediately after emplacement of the waste containers),
- volume of a brine pocket: 200 m³,
- time of interim storage of the waste packages: 10 y for CANDU fuel, 30 y for LWR fuel.

4 Results

The consequences of the three scenarios are calculated in two ways: by best estimate calculations and local sensitivity analyses. Best estimate calculations are deterministic calculations with best estimate values for the input parameters and some conservative assumptions in the modelling. Results are presented as doses to individuals for each scenario, neglecting the probability of occurrence. Local sensitivity analyses are best estimate calculations with one single parameter being varied over its assumed 3- σ range to study the behaviour of the system. Results of local sensitivity analyses are presented as released nuclide masses or as individual doses for each scenario as a function of the considered input parameter.

The performance assessments are made for both spent CANDU and spent LWR fuel repositories. In the following, the discussion is mainly focused on CANDU fuel, while results for LWR fuel are presented for comparison.

4.1 Best estimate results

4.1.1 Subrosion scenario

As described in Chapter 2.1 the subrosion rate determines the time of release of radionuclides and the radionuclide activity, too. In the best estimate case a subrosion rate of 0.033 mm/y is assumed which results in a time of release of $1.5 \cdot 10^7$ y. Time of release means the onset of a radionuclide flux into the groundwater. With this value the resulting maximum of the radiation exposure from CANDU fuel is $3.7 \cdot 10^{-4}$ Sv/y and in the LWR case $1.5 \cdot 10^{-4}$ Sv/y. The main contributor to dose is U-234 (Ra-226) in both cases. Although these radiation exposures are rather high compared to those of the combined accident scenario (cf. Chapter 4.1.3), the conservative assumptions in the model have to be kept in mind. The results of the best estimate calculations are listed in Table 4.6 together with results of local sensitivity analyses.

4.1.2 Human intrusion scenario

In this scenario, the temperatures in the neighbourhood of the waste containers after 1000 y can only be roughly estimated. By these preliminary calculations for CANDU fuel, three different sets of temperature have been chosen for the cavern sections. These calculations have been performed to demonstrate the negligible influence of a detailed modelling of the temperature fields. The results are listed in Table 4.1. It turned out that, due to the generally low temperatures of the emplacement field after 1 000 y, it is of minor importance which of the three options is used. Thus, in order to be conservative, the calculations are performed with the first set of temperatures which yields the highest radiological consequences.

Table 4.1 Preliminary tests on the influence of section temperatures on radiological consequences. CANDU fuel

No.	Temperature data	Time of cavern closure [y]	Time of dose maximum [y]	Maximum dose [Sv/y]
1.	- sump temperature corresponds to a field with highest temperatures - cavern has rock temperature at the reference level (i. e. no height dependence)	$8.89 \cdot 10^5$	$4.94 \cdot 10^5$	$6.80 \cdot 10^{-5}$
2.	- sump temperature corresponds to a field with highest temperatures - cavern has rock temperature at the centre of the cavity	$9.02 \cdot 10^5$	$5.05 \cdot 10^5$	$6.46 \cdot 10^{-5}$
3.	- every section has rock temperature at the corresponding depth	$9.03 \cdot 10^5$	$5.05 \cdot 10^5$	$6.47 \cdot 10^{-5}$

The temporal evolution of the scenario starts at $t = 0$ y by leaching the waste matrices, because containers are assumed to be defect from the beginning of the scenario. After 50 y, when the cavern is sealed, the porosity of the sump has gained a value of 0.365 (0.217 for LWR fuel) due to convergence. After that time, the brine pressure rises within less than 0.5 y from the hydrostatic level of 10 MPa to the given maximum value of 15 MPa. At this pressure it is assumed that the sealing of the cavern cracks and that the

contaminated brine starts to pass into the geosphere. The increase of brine pressure slows down the convergence, which reduces the brine flow.

Figure 4.1 shows the flow of brine out of the sump and out of the cavity. The effect of the closure of the sealing after 50 y can be seen clearly. At that moment, the flow from the sump to the cavity is reduced by two orders of magnitude and the brine outflow from the cavity into the overburden starts. There are some differences in the brine flows within the variants for CANDU and LWR fuel. In both cases, however, the cavity reaches its final porosity after about 900 000 y, as already listed in Table 4.1. At that moment, the porosity in the sump has still a value of 0.013 (0.0065 in the case of LWR).

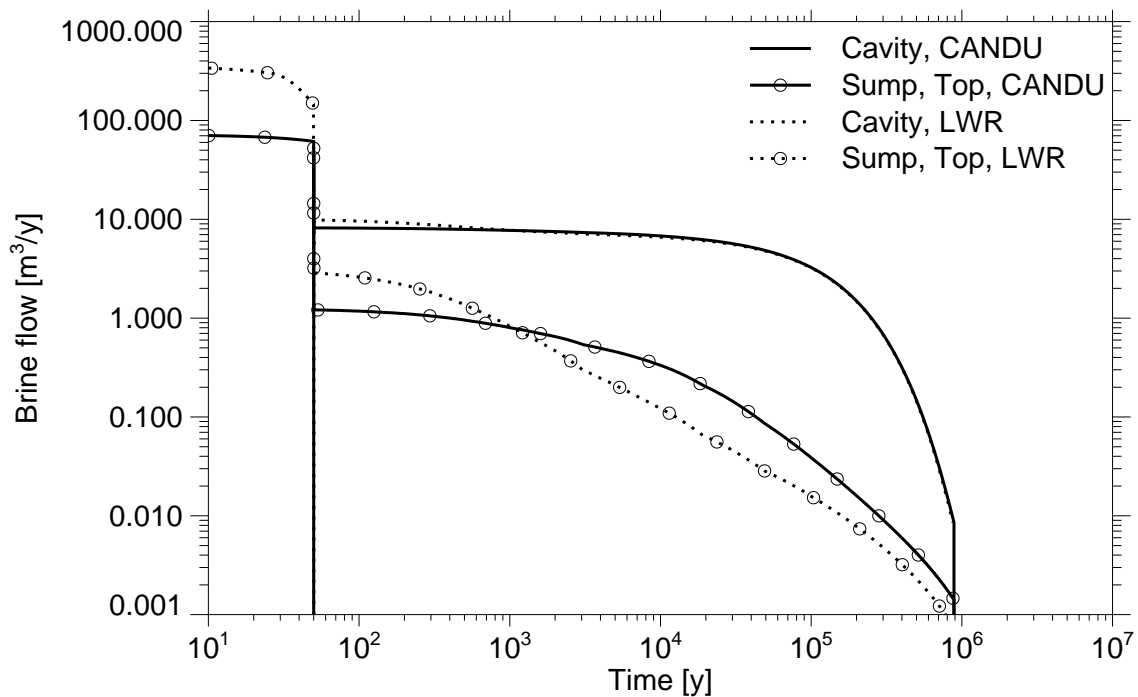


Fig. 4.1 Flow of brine out of the sump and out of the cavity

With the given values of the mobilisation rates for LWR and CANDU fuel, the mobilisation of radionuclides is fast and ends after 646 y. The released radionuclides reach the upper half of the sump by diffusion and by advective flow due to convergence of the bottom part. Figure 4.2 shows as an example the release rates of I-129 from the bottom part of the sump. The breakdown of the release rates at $t = 50$ y corresponds to the drop of brine flow as discussed with Figure 4.1.

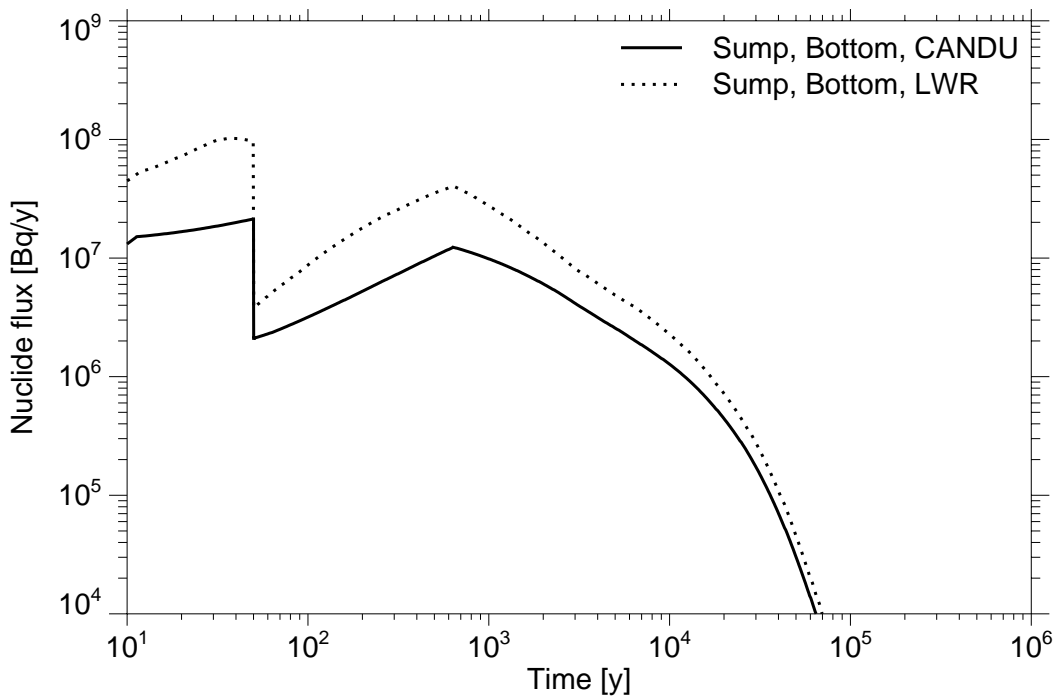


Fig. 4.2 Release rates of I-129 from the bottom part of the sump

The contaminated brine is squeezed out from the top of the sump into the open volume of the cavity by convergence. Finally, the radionuclides are released into the overburden when the cavity is filled with brine. This process starts at $t = 50$ y. In Figure 4.3 the release rates of I-129 out of the top half of the sump and out of the cavity are plotted. The shapes of the curves are similar to those in Figure 4.2, i. e. the cavity mainly acts as diluting volume for the radionuclides.

For some radionuclides with low solubility, the release is limited by the solubility limits. In Table 4.2 the times at which precipitation occurs for those elements are listed. Because the contaminated brine is diluted during movement from the sump to the cavity and because the assumed solubility limits are the same for all parts of the cavern, elements reach the solubility limits only in the bottom of the sump, where after mobilisation the highest concentrations occur.

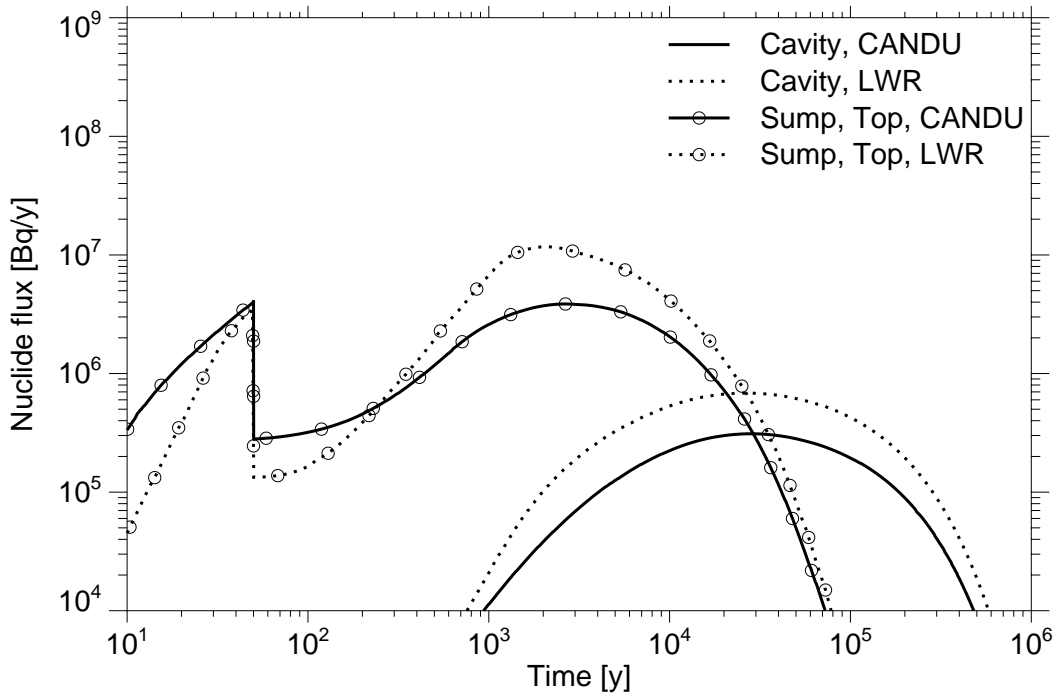


Fig. 4.3 Release rates of I-129 out of the top part of the sump and out of the cavity

Table 4.2 Time of precipitation of solubility controlled nuclides in the bottom of the sump

Element	Time of precipitation [y]	
	CANDU	LWR
Zr	6.8	3.7
Tc	-	504.4
Pu	3.0	3.0
Np	397.6	75.7
Th	285 676.9	22 418.7
U	1.5	2.9

After the discussion of the release of I-129, in Figures 4.4 and 4.5 the release rates out of the cavern for those nuclides are shown which contribute most to the radiation exposure. It can be seen that for LWR fuel the shape of the release curve of Np-237 is different from the other curves due to reaching the solubility limit of Np.

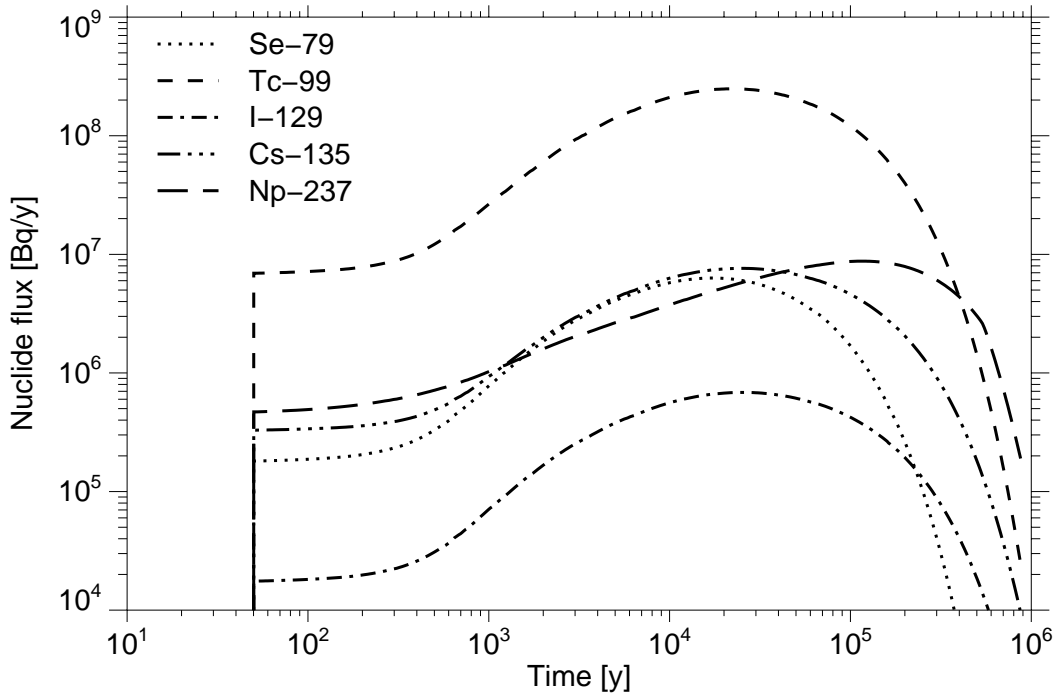


Fig. 4.4 Release rates of dose relevant nuclides from the cavern (LWR fuel)

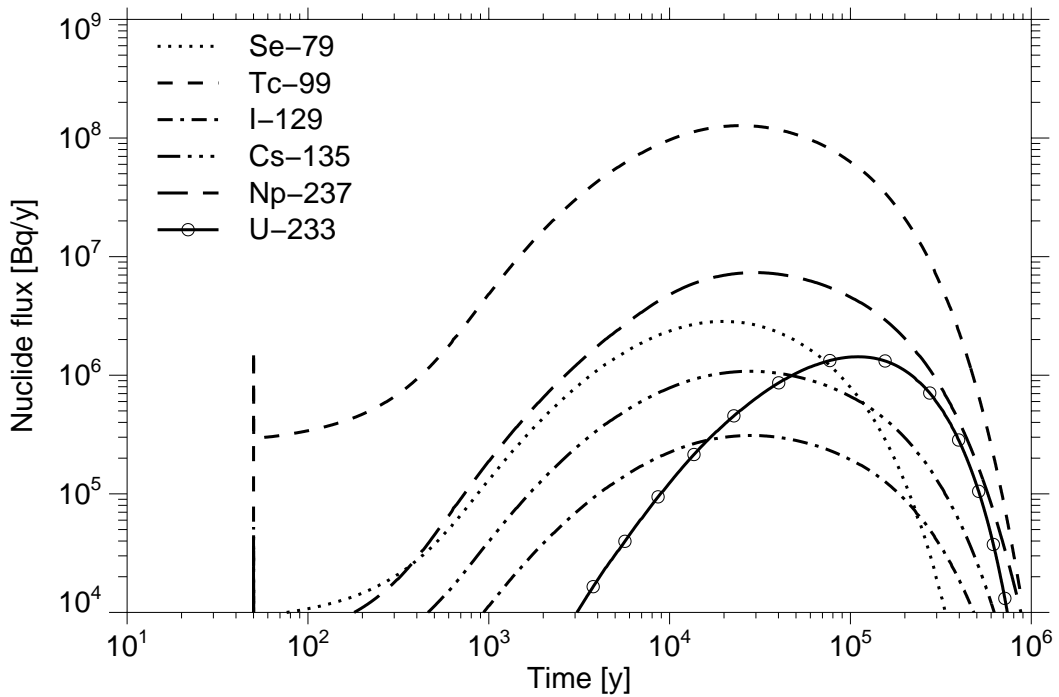


Fig. 4.5 Release rates of dose relevant nuclides from the cavern (CANDU fuel)

The corresponding temporal evolution of the annual radiation exposure is shown in Figures 4.6 and 4.7. With CANDU fuel, the annual radiation exposure attains a maximum of $6.8 \cdot 10^{-5}$ Sv/y at $t = 494\ 000$ years. The main contributions to the radiation exposure are from Np-237, followed by U-233, I-129 and Tc-99. For LWR fuel, the maximum is $1.26 \cdot 10^{-4}$ Sv/y at $t = 553\ 000$ years. In this case, the main contributions to the radiation exposure are again from Np-237, followed by I-129 and Tc-99. In both cases, Se-79 dominates the radiation exposure at early times.

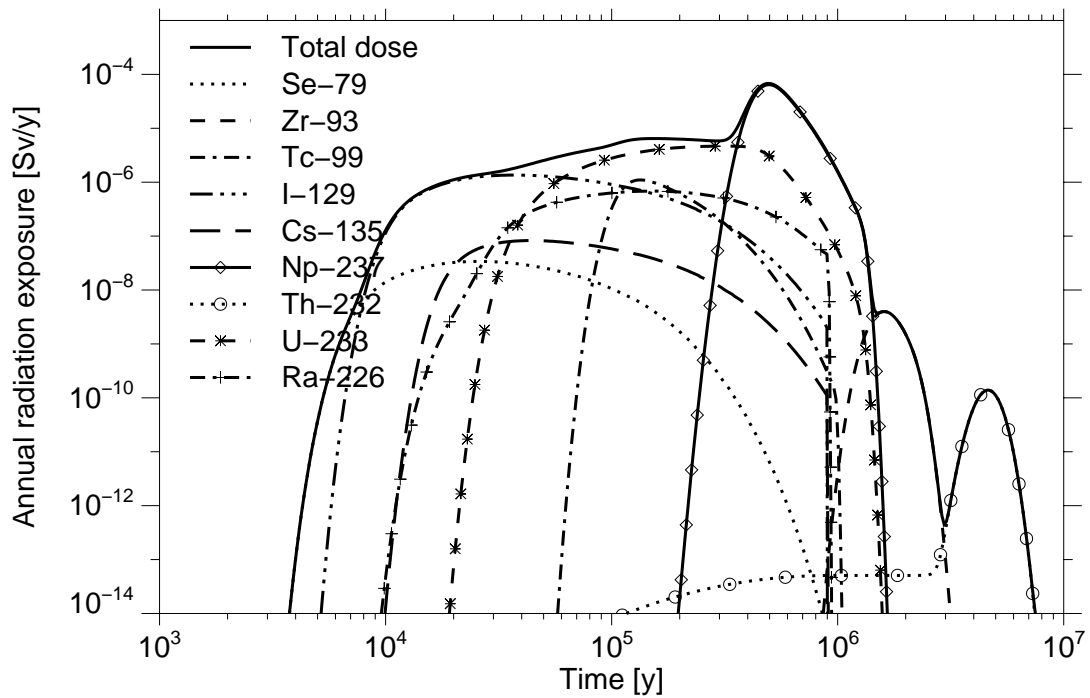


Fig. 4.6 Human intrusion scenario (CANDU fuel): Temporal evolution of the radiation exposure in the reference case

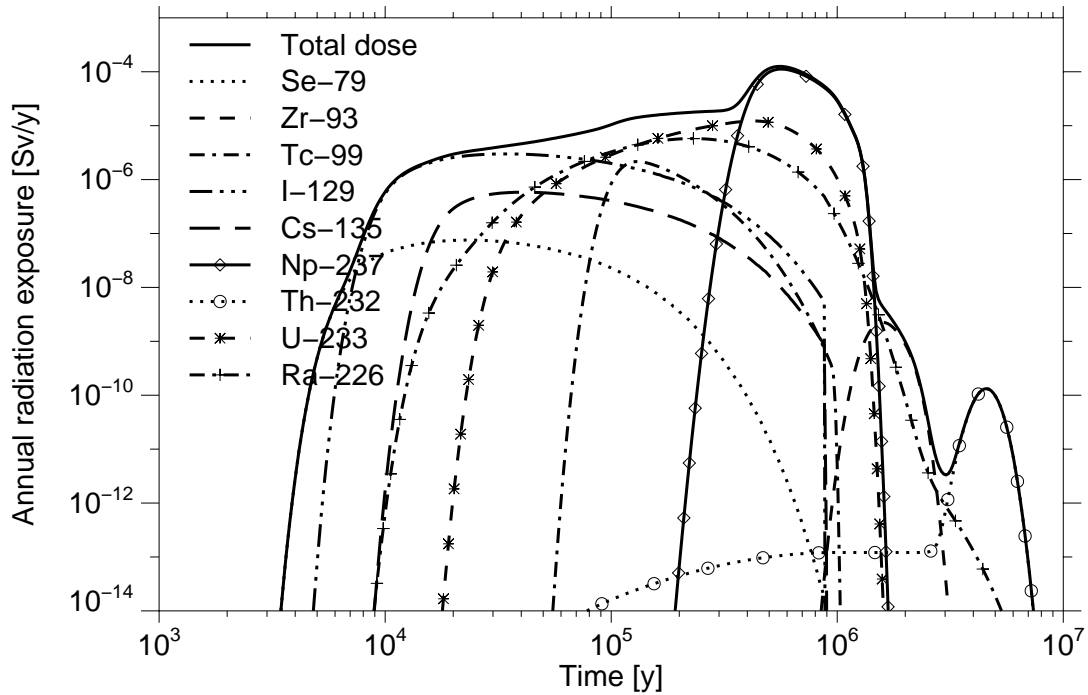


Fig. 4.7 Human intrusion scenario (LWR fuel): Temporal evolution of the radiation exposure in the reference case

4.1.3 Combined accident scenario

The results are presented in this chapter first for CANDU fuel, then for LWR fuel. The best estimate values of the input parameters are the same for both fuel types, with some exceptions regarding radionuclide inventories and, for some nuclides, solubility limits and distribution of nuclide inventory between gap and matrix of the fuel elements.

4.1.3.1 Repository with CANDU fuel elements

The time history of relevant segments and the amounts of water entering the repository are listed in Table 4.3. All emplacement fields contribute to the radionuclide release because brine from the brine pockets keeps most of the emplacement drifts open due to the brine back pressure reducing convergence. Thus the intruding brine from the main anhydrite can flow from the central field into the emplacement areas. Only those emplacement

Table 4.3 Combined accident scenario (CANDU fuel): Time history of segments

Segment	Contact to geosphere	Period of inflow [y]		Begin of squeezing out [y]	Brine volumes [m ³]				Time of final porosity [y]
		Begin	End		Inflow		Outflow		
					from above	from below	above	below	
BP50C	yes	0.1	0.1	0.12	400		350		
BP50A	yes	0.1	0.1	0.12	400		351		
BP43A	yes	0.1	0.1	0.12	400		369		
BP36A	yes	0.1	0.1	0.12	400		362		
BP28A	yes	0.1	0.1	0.12	400		356		
BP21A	yes	0.1	0.1	0.12	400		353		
BP14A	yes	0.1	0.1	0.12	400		350		
BP07A	yes	0.1	0.1	0.12	400		298		
ED50A	yes	0.11	57	57		351	297		
ED50B	no	92			138				152
ED50C	yes	0.11	41	41		350	296		
ED43A	yes	0.11	36	36		369	309		
ED43B	no	77			120				128
ED43C	yes	0.11	35	35		304	244		
ED36A	yes	0.11	34	34		362	298		
ED36C	yes	0.11	33	33		292	229		
ED28A	yes	0.11	32	32		356	289		
ED28C	yes	0.11	31	31		282	218		
ED21A	yes	0.11	31	31		353	284		
ED21C	yes	0.11	31	31		276	211		
ED14A	yes	0.11	31	31		350	281		
ED14C	yes	0.11	30	31		272	207		
ED07A	yes	0.11	29	30		298	228		
ED07C	yes	0.11	14	14		284	215		
CD50B	yes	41	92	92	7	243	139	85	
CD50A	yes	57	89	90		431	417	1.5	
CD43B	yes	35	77	77	47	199	141	75	
CD43A	yes	36	62	62		411	388	7	
CD36B	yes	33	76	76	47	189	135	68	
CD36A	yes	34	60	60		393	367	7	
CD28B	yes	31	76	76	47	182	131	62	

Table 4.3 Combined accident scenario (CANDU fuel): Time history of segments
(Contd.)

Segment	Contact to geosphere	Period of inflow [y]		Begin of squeezing out [y]	Brine volumes [m ³]				Time of final porosity [y]
		Begin	End		Inflow		Outflow		
					from above	from below	above	below	
CD28A	yes	32	59	59		380	354	6.9	
CD21B	yes	31	75	75	47	175	125	61	
CD21A	yes	31	58	58		368	341	6.8	
CD14B	yes	30	74	74	48	171	120	60	
CD14A	yes	31	57	57		360	333	6.6	
CD07B	yes	14	66	66	5.8	185	113	39	
CD07A	yes	29	63	63		335	315	0.2	
MD07	yes	63	182	184		315	202		
MD14	yes	57	185	186		535	407		
MD21	yes	58	186	187		748	621		
MD28	yes	59	187	188		974	851		
MD36	yes	60	189	189		1 218	1 102		
MD43	yes	62	191	191		1 490	1 390		
MD50	yes	89	210	211		1 806	1 729		
CF2	yes	196	245	246	4 146	1 729	5 168		
MF	yes	85	196	246	11 347	5 168	11 857	4 146	

drifts which are not connected to brine pockets do not contribute to the release of radionuclides. Because there is no brine to reduce the convergence process, these emplacement drifts are closed by convergence before any brine can enter them.

Almost 15 845 m³ of water enters into the repository, 11 347 m³ intruding from the geosphere and 4 498 m³ from the brine pockets. About 11 857 m³ of contaminated water is squeezed out of the repository over the time period of 1 million years, which is a little bit more than the total inflow from the geosphere. By convergence almost 80 % of the brine volume of the brine pockets is squeezed out into the emplacement drifts.

Flow of brine into and out of the main field is plotted in Figure 4.8. At the bottom of this figure, the corresponding flows for the 7th emplacement field, which is adjacent to the

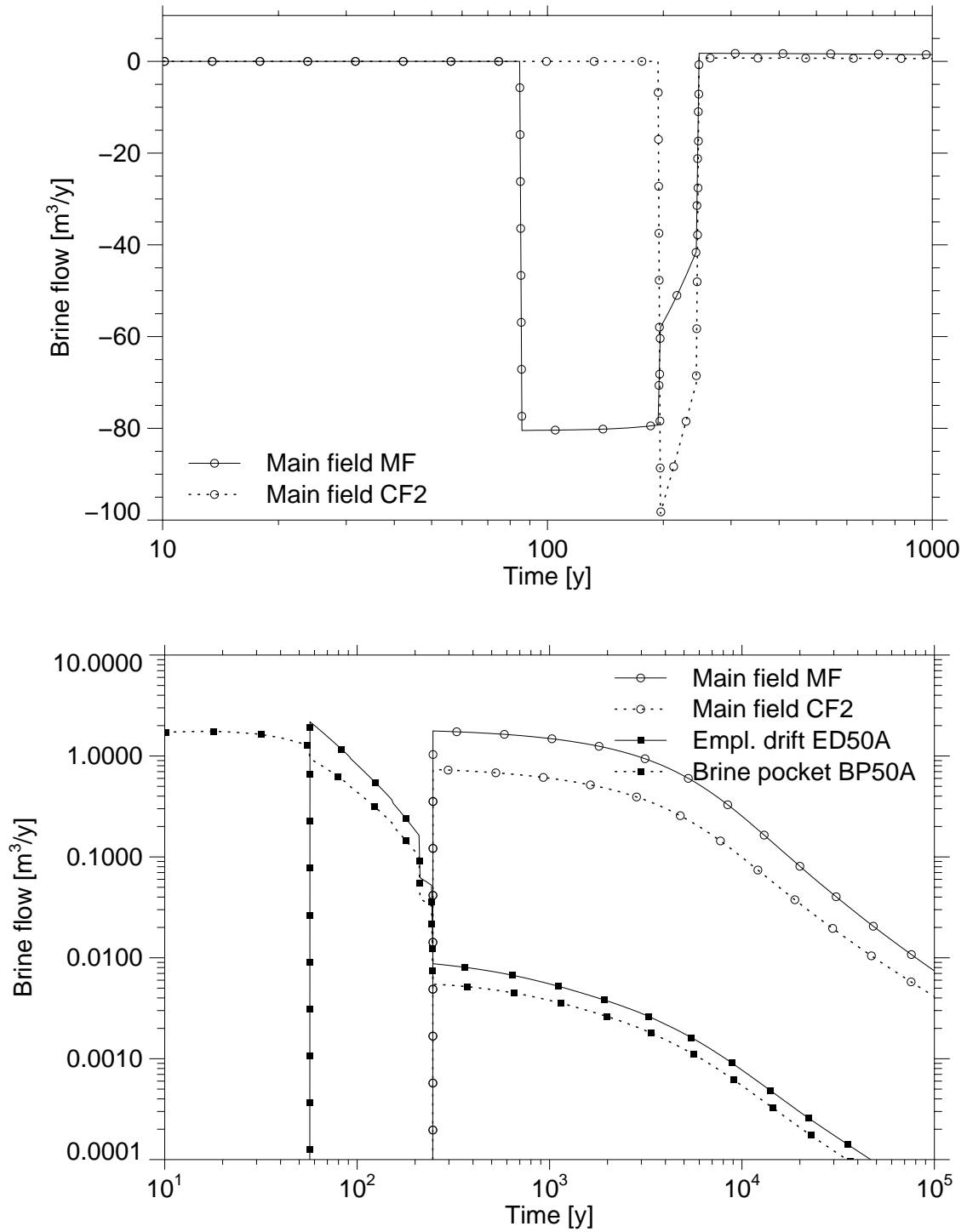


Fig. 4.8 Combined accident scenario (CANDU fuel):
 a) above: Flow of brine into (negativ values) and out of (positive values) the main field;
 b) below: Flow of brine out of the main field (only positive values of the above figure), out of an emplacement drift, and out of a brine pocket

main field, are shown additionally for the segments ED50A and BP50A. For computational reasons the main field has been split into two parts: MF facing the geosphere and CF2 facing the inner parts of the repository, i. e. the main drift MD50. Brine from the anhydrite vein starts to enter the main field at $t = 85$ y and flows towards the main drift MD50 (flow of brine is negative). Later on, at $t = 246$ y, contaminated brine changes its flow direction and is squeezed out towards the geosphere (positive flow). Almost 90 % of the contents of the brine pocket BP50A is released into the emplacement drift ED50A, which is completely filled at $t = 57$ y.

The main contributions to the total dose are by I-129, followed by Ra-225, Np-237, and U-233. The temporal evolutions of the radiation exposures for several of the most important nuclides are shown in Figure 4.9. The total dose rises to about $9 \cdot 10^{-6}$ Sv/y at 440 000 y and is more than one order of magnitude below the limit of German radiation protection law.

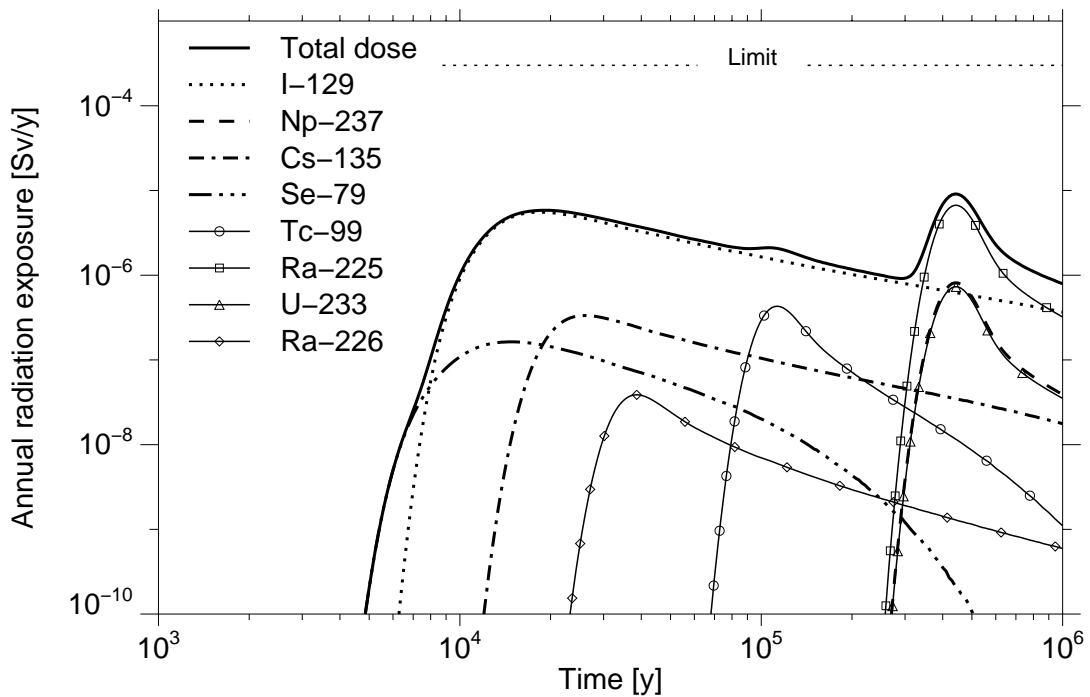


Fig. 4.9 Combined accident scenario (CANDU fuel): Temporal evolution of the radiation exposure in the reference case

4.1.3.2 Repository with spent LWR fuel elements

The time history of segments and the amount of water entering the repository is listed in Table 4.4. Only the emplacement drifts ED50A and ED50C of field 7 adjacent to the main field contribute to the radionuclide release. Any other field is closed by convergence before brine from the brine pockets comes into contact with brine from the main field. This is different from the case of CANDU fuel (cf. Chapter 4.1.3.1) and is due to the higher temperatures in emplacement fields with LWR fuel. Segments omitted in the table reach final porosity later than a segment in direction of the main field and have no contact to brine. Most of the segments of the fields 1 to 5 have been omitted because they are never relevant to release of radionuclides from the near field.

Table 4.4 Combined accident scenario (LWR fuel): Time history of segments

Segment	Contact to geosphere	Period of inflow [y]		Begin of squeezing out [y]	Brine volumes [m ³]				Final porosity	
		Begin	End		Inflow		Outflow		Time [y]	Segment
					from above	from below	above	below		
BP50C	yes	0.1	0.1	0.1	400		94			
BP50A	yes	0.1	0.1	0.1	400		99			
BP43A	no	0.1	0.1	0.1	400		52		129	extern
BP36A	no	0.1	0.1	0.1	400		40		128	extern
BP28A	no	0.1	0.1	0.1	400		36		127	extern
BP21A	no	0.1	0.1	0.1	400		35		126	extern
BP14A	no	0.1	0.1	0.1	400		35		126	extern
ED50A	yes	0.1	18	18		99	43			
ED50B	no								16	backfill
ED50C	yes	0.1	10	11		94	34			
ED43A	no	0.1	5.0	5.3		52	7.5		129	extern
ED43B	no								0.1	backfill
ED43C	no								0.1	backfill
ED36A	no	0.1	3.2	3.3		40	3.5		128	extern
ED28A	no	0.1	2.9	3.0		36	2.3		127	extern
ED21A	no	0.1	2.9	2.9		35	2.3		126	extern
ED14A	no	0.1	2.9	2.9		35	2.2		126	extern

Table 4.4 Combined accident scenario (LWR fuel): Time history of segments
(Contd.)

Segment	Contact to geosphere	Period of inflow [y]		Begin of squeezing out [y]	Brine volumes [m ³]				Final porosity	
		Begin	End		Inflow from above	Inflow from below	Outflow above	Outflow below	Time [y]	Segment
ED07A	no								-17	backfill
CD50B	yes	10	56	57		34	7.0			
CD50A	yes	17	68	68		50	33			
CD43B	no								46	backfill
CD43A	no	5.0	68	68		7.5	0.4		129	extern
MD43	no	68				0.4			129	backfill
MD50	yes	68	144	146		33	11			
MF	yes	85	234	236	11 803	11	11 055			

The total amount of water entering the repository is about 12 190 m³, 11 800 m³ intruding from the geosphere, 390 m³ from the brine pockets. About 11 055 m³ of contaminated brine are squeezed out of the repository over 1 million years. This is about the same amount as the total inflow from the geosphere. It is remarkable that only about 7 % of the total volume of the brine pockets are squeezed out into the emplacement drifts. This is due to the early closure of most of these drifts by the convergence process.

A plot of the temporal evolution of the radiation exposures is shown in Figure 4.10. The total dose is dominated by I-129 and Cs-135 and the maximum is more than three orders of magnitude below the limit of German radiation protection law. The contributions to the total dose of other radionuclides besides I-129 and Cs-135 are about two orders of magnitude lower than the dose of I-129.

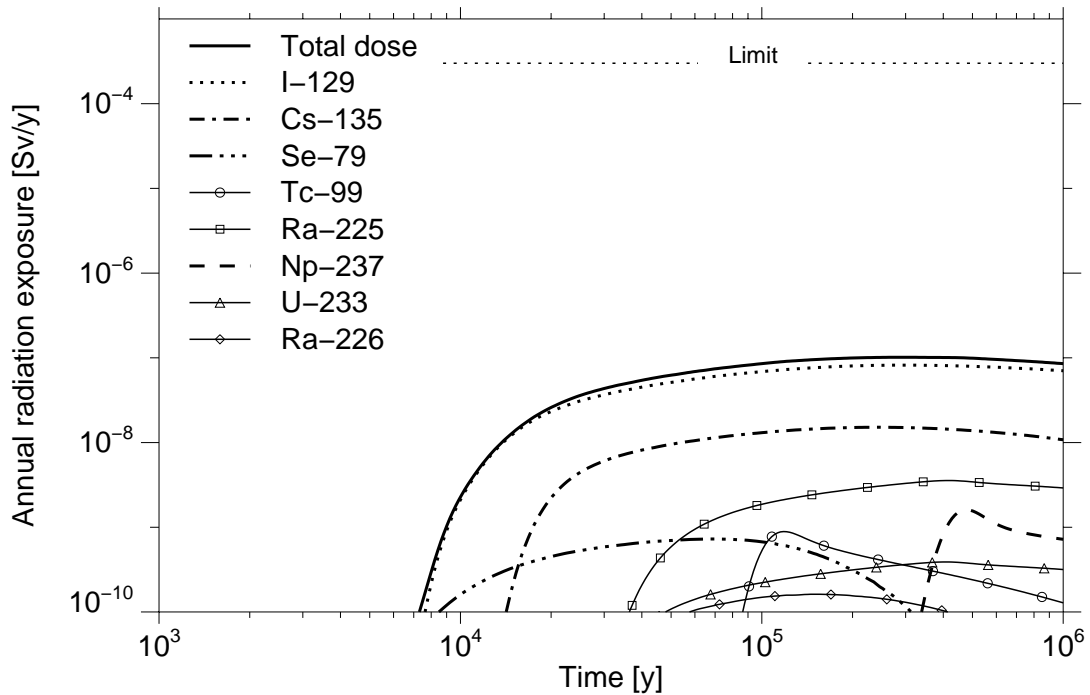


Fig. 4.10 Combined accident scenario (LWR fuel): Temporal evolution of the radiation exposure in the reference case

4.2 Local sensitivity analyses

4.2.1 Local sensitivity analyses: Subrosion scenario

For local sensitivity analyses the subrosion rate and the dilution factor have been varied. The calculated radiation exposures depend strongly on the subrosion rates because the times of release and thus the actual activities at these times change. The dilution of concentrated brine to quality of drinking water has a similarly strong influence because in agreement with the model assumptions the radionuclide concentrations are diluted by the same factor (high dilution means low concentration). Tables 4.5 and 4.6 give a summary of the results of the local sensitivity analyses. Taking into account the 3- σ ranges of the subrosion rate and the salt concentration in water as discussed in Chapter 3.2.1, the total doses for CANDU fuel are in the range from $1.0 \cdot 10^{-5}$ Sv/y to $1.7 \cdot 10^{-2}$ Sv/y as listed in Table 4.5 ($3.5 \cdot 10^{-6}$ Sv/y to $4.8 \cdot 10^{-2}$ Sv/y for LWR fuel). In all cases U-234 is the most important radionuclide with respect to the total dose.

Table 4.5 Subrosion scenario: Maximum radiation exposure [Sv/y] for CANDU and LWR fuel as function of subrosion rate and concentration of salt

Subrosion rate [mm/y]	Salt concentration [mg/l]					
	1		31 (best estimate)		1000	
	CANDU	LWR	CANDU	LWR	CANDU	LWR
2.2	$1.7 \cdot 10^{-5}$	$4.8 \cdot 10^{-5}$	$5.3 \cdot 10^{-4}$	$1.5 \cdot 10^{-3}$	$1.7 \cdot 10^{-2}$	$4.8 \cdot 10^{-2}$
0.5	$1.4 \cdot 10^{-5}$	$1.9 \cdot 10^{-5}$	$4.4 \cdot 10^{-4}$	$5.9 \cdot 10^{-4}$	$1.4 \cdot 10^{-2}$	$1.9 \cdot 10^{-2}$
0.033 (b. e.)	$1.2 \cdot 10^{-5}$	$4.7 \cdot 10^{-6}$	$3.7 \cdot 10^{-4}$	$1.5 \cdot 10^{-4}$	$1.2 \cdot 10^{-2}$	$4.7 \cdot 10^{-3}$
0.005	$1.2 \cdot 10^{-5}$	$4.1 \cdot 10^{-6}$	$3.6 \cdot 10^{-4}$	$1.3 \cdot 10^{-4}$	$1.2 \cdot 10^{-2}$	$4.1 \cdot 10^{-3}$
0.0005	$1.0 \cdot 10^{-5}$	$3.5 \cdot 10^{-6}$	$3.1 \cdot 10^{-4}$	$1.1 \cdot 10^{-4}$	$1.0 \cdot 10^{-2}$	$3.5 \cdot 10^{-3}$

Table 4.6 Subrosion scenario (CANDU fuel): Maximum radiation exposure [Sv/y] as function of subrosion rate. Concentration of salt: 31 mg/l

Nuclide	Subrosion rate [mm/y]				
	2.2	0.5	0.033 (b.e.)	0.005	0.0005
Rb-87	$4.78 \cdot 10^{-11}$	$4.78 \cdot 10^{-11}$	$4.78 \cdot 10^{-11}$	$4.77 \cdot 10^{-11}$	$4.71 \cdot 10^{-11}$
Zr-93	$2.45 \cdot 10^{-07}$	$1.73 \cdot 10^{-07}$	$3.05 \cdot 10^{-10}$	$5.91 \cdot 10^{-27}$	0.0
Tc-99	$2.50 \cdot 10^{-06}$	$2.01 \cdot 10^{-07}$	$3.44 \cdot 10^{-27}$	0.0	0.0
Pd-107	$3.56 \cdot 10^{-09}$	$3.27 \cdot 10^{-09}$	$7.36 \cdot 10^{-10}$	$8.53 \cdot 10^{-14}$	0.0
I-129	$3.84 \cdot 10^{-06}$	$3.71 \cdot 10^{-06}$	$2.00 \cdot 10^{-06}$	$4.70 \cdot 10^{-08}$	$2.67 \cdot 10^{-25}$
Cs-135	$2.24 \cdot 10^{-07}$	$1.77 \cdot 10^{-07}$	$2.61 \cdot 10^{-09}$	$1.98 \cdot 10^{-20}$	0.0
Sm-147	$1.03 \cdot 10^{-11}$	$1.03 \cdot 10^{-11}$	$1.03 \cdot 10^{-11}$	$1.02 \cdot 10^{-11}$	$1.02 \cdot 10^{-11}$
Pu-244	$2.46 \cdot 10^{-11}$	$2.45 \cdot 10^{-11}$	$2.17 \cdot 10^{-11}$	$1.07 \cdot 10^{-11}$	$5.63 \cdot 10^{-15}$
U-236	$1.22 \cdot 10^{-05}$	$1.20 \cdot 10^{-05}$	$7.89 \cdot 10^{-06}$	$6.38 \cdot 10^{-07}$	$5.18 \cdot 10^{-16}$
Th-232	$2.49 \cdot 10^{-07}$	$2.49 \cdot 10^{-07}$	$2.49 \cdot 10^{-07}$	$2.49 \cdot 10^{-07}$	$2.40 \cdot 10^{-07}$
Np-237	$4.23 \cdot 10^{-05}$	$3.29 \cdot 10^{-05}$	$3.53 \cdot 10^{-07}$	$3.95 \cdot 10^{-19}$	0.0
U-233	$2.56 \cdot 10^{-06}$	$2.42 \cdot 10^{-06}$	$2.65 \cdot 10^{-08}$	$2.96 \cdot 10^{-20}$	0.0
Pu-242	$1.23 \cdot 10^{-04}$	$3.08 \cdot 10^{-05}$	$4.02 \cdot 10^{-16}$	0.0	0.0
U-238	$3.4 \cdot 10^{-05}$	$3.36 \cdot 10^{-05}$	$3.4 \cdot 10^{-05}$	$3.3 \cdot 10^{-05}$	$2.9 \cdot 10^{-05}$
U-234	$3.4 \cdot 10^{-04}$	$3.3 \cdot 10^{-04}$	$3.27 \cdot 10^{-04}$	$3.2 \cdot 10^{-04}$	$2.8 \cdot 10^{-04}$
Cm-247	$1.5 \cdot 10^{-13}$	$1.4 \cdot 10^{-13}$	$7.6 \cdot 10^{-14}$	$1.7 \cdot 10^{-15}$	$7.7 \cdot 10^{-33}$
U-235	$5.2 \cdot 10^{-07}$	$5.2 \cdot 10^{-07}$	$5.1 \cdot 10^{-07}$	$4.7 \cdot 10^{-07}$	$1.9 \cdot 10^{-07}$

A comparison of the results with PAGIS [6] is interesting. In PAGIS, emplacement of waste has been assumed to be in 300 m deep boreholes, in the present study in drifts. Thus, the results of the subsrosion scenario are different because it takes much longer to lay bare a deep repository than a flat repository. This is sketched in Figure 4.11. For the best estimate value of the subsrosion rate, it takes 9 million years to dissolve all of the salt of the emplacement area (thickness ΔH) in the case of PAGIS, but only 300 000 years in the present study. Thus, the concentrations of the dissolved radionuclides would be also different by a factor of 30 if the initial inventories were the same. The higher difference of a factor of 150 in the calculated maxima of the total doses (PAGIS: $9.7 \cdot 10^{-7}$ Sv/y; this study (LWR fuel): $1.5 \cdot 10^{-4}$ Sv/y) is thus a result of the different emplacement technique (borehole vs. drift) and the different initial inventories of the dose relevant radionuclides.

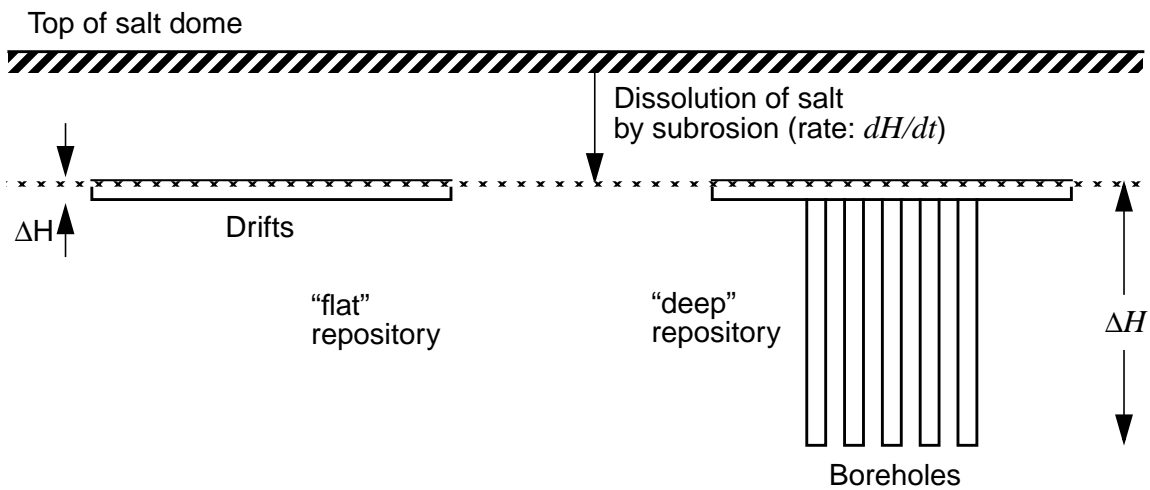


Fig. 4.11 Comparison of subsrosion process for deep and flat repositories

Although the maximum radiation exposures are in many cases above the German dose rate limit of $3 \cdot 10^{-4}$ Sv/y, it should be kept in mind that the model for the subsrosion scenario is over-conservative and simple, e. g. it takes neither sorption in the geosphere nor solubility limits at the place of dissolution of waste into account. Thus, the calculated radiation exposures are conservative maximum values and a more realistic calculation should be performed which is expected to result in much lower values.

4.2.2 Local sensitivity analyses: Human intrusion scenario

In this chapter the results of varying five parameters are presented. These parameters are varied according to their given ranges (cf. Table 3.7):

- solubility limits,
- diffusion coefficient $D(T_0)$,
- exponent in permeability-porosity relation q ,
- reference convergence rate K_r , and
- maximum brine pressure p_{max} .

The main interest in the parameter variations is the influence of these parameters on the maximum radiation exposure. For some parameters, like the maximum brine pressure and the reference convergence rate, additional results are presented concerning the released masses of representative nuclides, the release rates out of the cavern and the times at which sections reach the impermeable state.

4.2.2.1 Variation of the solubility limits

The best estimate values of the element specific solubility limits are varied by a common factor for all elements in the range between 0.1 and 10. This variation has been performed only for CANDU fuel. Figure 4.12 shows the resulting maximum radiation exposures.

The radiation exposure is directly influenced by the dissolved activity. Lowering the solubility limits means that a higher amount of contaminants precipitates and is no longer available for transport by water flow. This reduces the radiation exposure. The maximum radiation exposure decreases by 64.3 % of the best estimate value if all the solubility limits are set to the lower limit. For best estimate value and for values towards the upper limit no solubility limit of the dose relevant nuclide Np-237 is attained. Thus, the increase of maximum radiation exposure for the maximum solubility limit is much lower by only 3.75 %. It is caused by inventory build-up due to radioactive decay of parent nuclides, which reach solubility limits at later times. The times at which the maximum radiation exposures are attained vary between 554 000 y and 494 000 y.

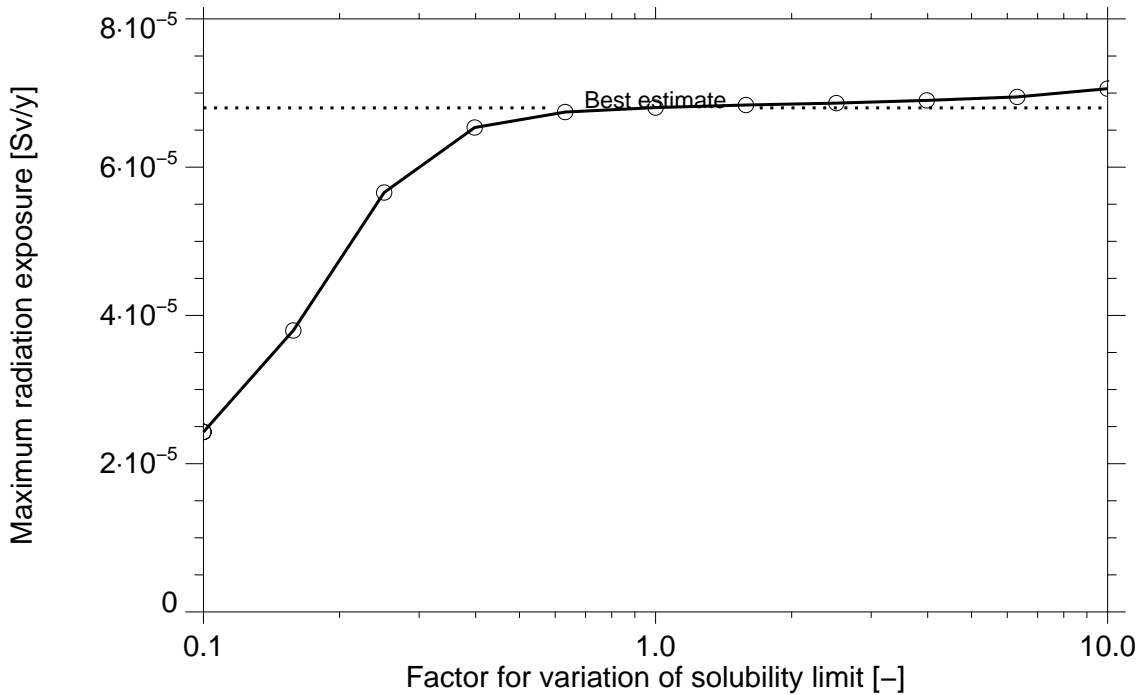


Fig. 4.12 Human intrusion scenario (CANDU fuel): Maximum radiation exposure (total dose) as function of solubility limit

4.2.2.2 Variation of the diffusion coefficient

The diffusion coefficient is varied in the range between $5 \cdot 10^{-11}$ and $4.5 \cdot 10^{-8}$ m²/s. The results of the variation are presented in Figure 4.13. Diffusion is a transport mechanism for radionuclides in solution additional to advective flow. Reducing the diffusion coefficient reduces the radiation exposure, and the maximum of the radiation exposure is shifted to later times. For the lower limit of the diffusion coefficient, the maximum radiation exposures are reduced by 57 % (83 % for LWR fuel) of the best estimate value. For the upper limit the maximum radiation exposure changes much less to about 1 % above the best estimate value (89 % for LWR fuel). This can be explained as follows: As in the computer model the release from the cavern into the overburden is purely advective, it is proportional to the nuclide concentration in the cavity. If diffusion is fast, an almost constant concentration is attained in the sump and the cavity. Thus, the release into the overburden and consequently the radiation exposure becomes independent of changes in the diffusion coefficient for high values.

The different behaviour of CANDU and LWR fuel results from the different relative contributions of advective and diffusive flows. Due to lower temperatures in the CANDU case diffusive flow is important compared to advective flow already for the best estimate value of the diffusion coefficient. Thus in the range considered, its influence on maximum radiation exposure is less pronounced than for LWR fuel.

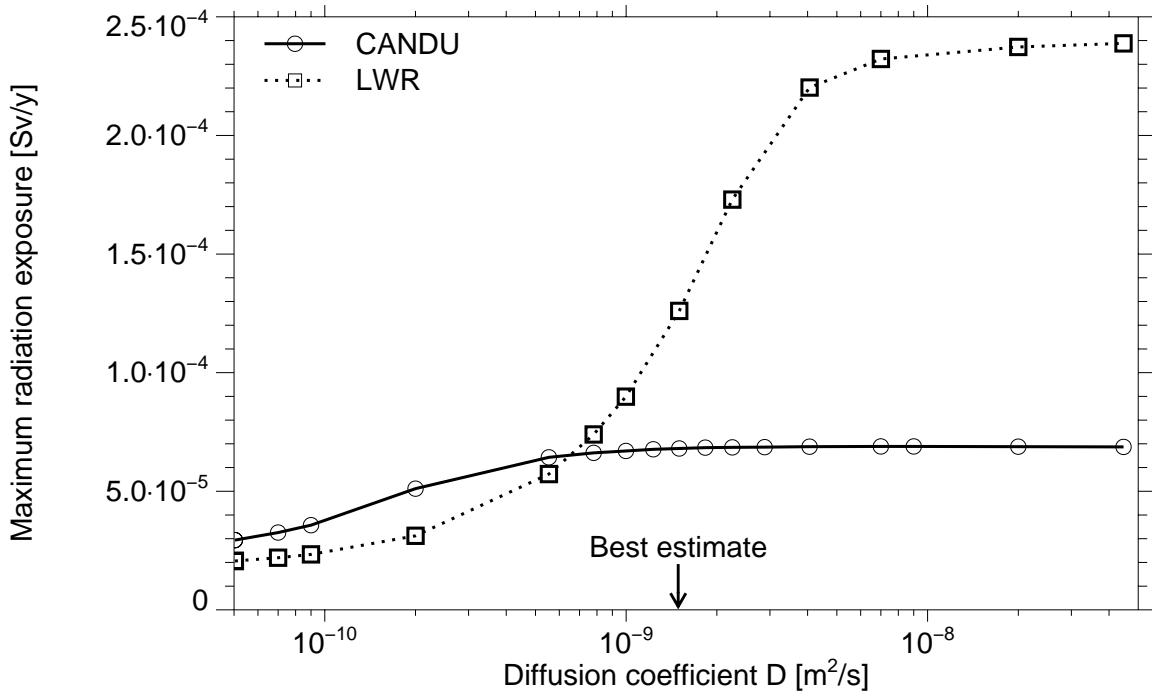


Fig. 4.13 Human intrusion scenario: Maximum radiation exposure (total dose) as function of diffusion coefficient

4.2.2.3 Variation of the exponent q in the permeability-porosity relation

According to [8], the permeability of sealings and backfill is calculated from the porosity by the equation:

$$K = f_p c \phi^q \tag{12}$$

where c and the exponent q are empirical constants obtained from experimental data. The variation factor f_p is introduced to model a more permeable sealing and backfill in the fill-up phase.

The sensitivity analysis performed for the exponent q shows that this parameter has almost no influence on the radiation exposure, so the results are not shown.

4.2.2.4 Variation of the reference convergence rate

The influence of the variation of the reference convergence rate on the maximum radiation exposures is shown in Figure 4.14. For the lower limit of the reference convergence rate, the maximum of the radiation exposure is reduced by 97 % of the reference value (96 % for LWR fuel). For the upper limit, the radiation exposure is about at the reference value, for LWR fuel it is about 76 % less than the reference value. For the 3- σ range of the reference convergence rate, the times of occurrence of the maximum radiation exposures vary between 580 000 y and 450 000 y for both types of fuel. The times of reaching

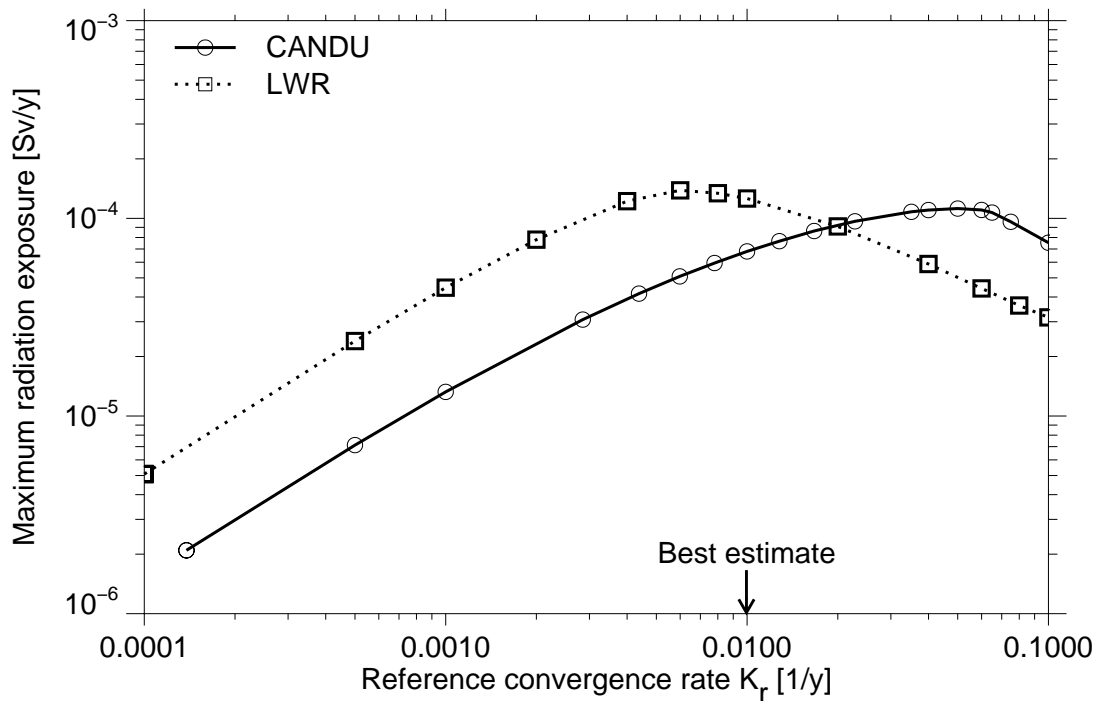


Fig. 4.14 Human intrusion scenario: Maximum radiation exposure (total dose) as function of reference convergence rate

the final porosity in the cavity (i. e. the times of section closure) are decreasing from $6.5 \cdot 10^7$ y (940 000 y for LWR fuel) to 85 000 y for both types of fuel. A maximum occurs for a reference convergence rate of $K_r = 5 \cdot 10^{-2} \text{ y}^{-1}$ ($K_r = 6 \cdot 10^{-3} \text{ y}^{-1}$ for LWR fuel). This maximum is almost 65 % higher than the reference value (11 % for LWR fuel).

With decreasing convergence rate the release of radionuclides is retarded and the maxima of the radiation exposures are shifted to later times.

The cumulative released masses of radionuclides (after 10^6 y) for a varied convergence rate are plotted in Figure 4.15 for CANDU fuel. The releases are shown for:

- a long-lived nuclide with a high solubility limit, e.g. I-129
- a long-lived nuclide with a low solubility limit, e.g. Np-237
- a short-lived nuclide with a high solubility limit, e.g. C-14

A short-lived nuclide with low solubility limit is not shown because all the relevant nuclides are decayed over the considered time interval. As long as the time of section closure,

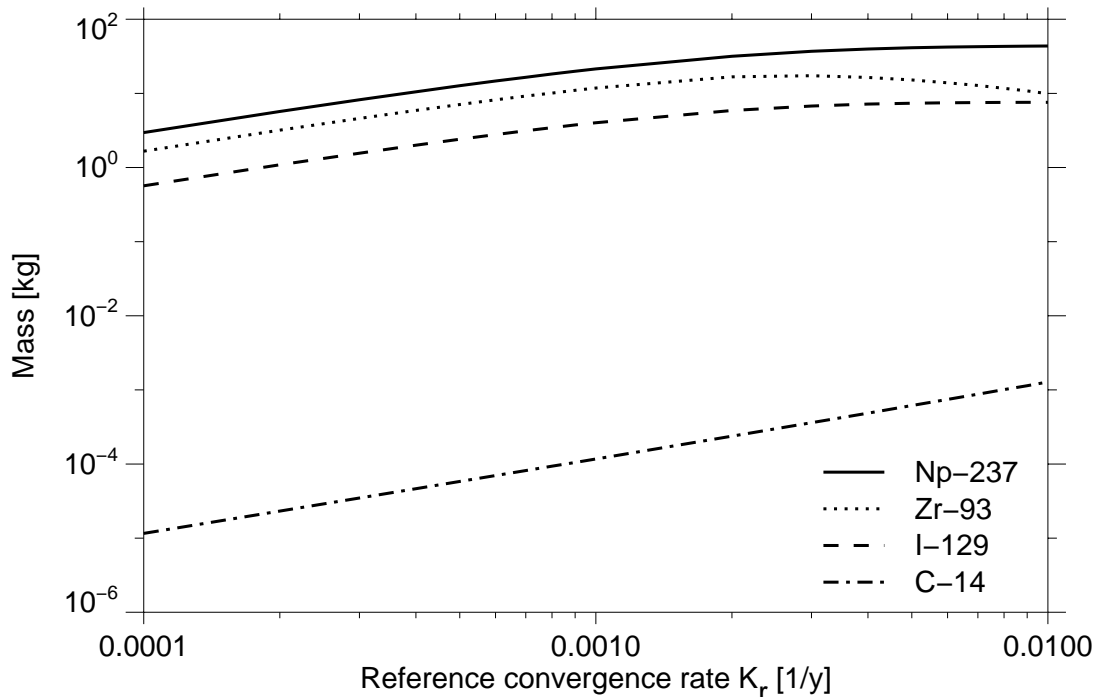


Fig. 4.15 Human intrusion scenario (CANDU fuel): Local sensitivity analyses for the reference convergence rate – Released masses from the cavity after 10^6 y

which is a function of the convergence rate, is later than 10^6 years, the cumulative release in general increases with increasing convergence rate. The decreases of the Zr-93 and Np-237 curves for $K_r > 3.0 \cdot 10^{-3} \text{ y}^{-1}$ reflect that both elements precipitate due to reaching their solubility limits before the top section attains final porosity. As Table 4.2 shows, Zr attains its solubility limit in the bottom part of the sump at very early times (6.8 y). For Np the time of attaining the solubility limit decreases slowly with increasing convergence rate from 457.3 y to 397.6 y due to build-up from its parent nuclide Am-241.

4.2.2.5 Variation of the maximum brine pressure

The maximum brine pressure has been varied between 13 MPa and 17 MPa. The results are shown in Figure 4.16. With increasing maximum brine pressure, the convergence of the cavern and, consequently, the times of cavity closure are retarded. Increasing the brine pressure results in an increase of the time of cavity closure from 110 000 y for both fuel types to $7.2 \cdot 10^7$ y ($>10^7$ y for LWR fuel). With increasing brine pressure the release curves of the radionuclides are shifted to later times and are additionally broadened. For CANDU fuel the maximum radiation exposures are decreasing. For LWR fuel, a maximum in the curve occurs at about the reference value of 15 MPa. For the lower limit of the brine pressure, the maximum radiation exposure rises to 79 % above the best estimate case, for LWR fuel the maximum drops by 35 %. For the upper limit, the maximum radiation exposure decreases by 97 % of the best estimate value (95 % for LWR fuel).

For CANDU fuel, Table 4.7 lists the mobilized and released masses in kg of some selected nuclides with different half-lives out of the sump and out of the cavern. An increase of the maximum brine pressure (and, consequently, decrease of the convergence process) generally results in an increase of the released masses into the sump. Long-lived nuclides with a high solubility limit (e. g. I-129 and Cs-135) show released masses similar to release rates, i. e. release rates and released masses decrease as pressure increases.

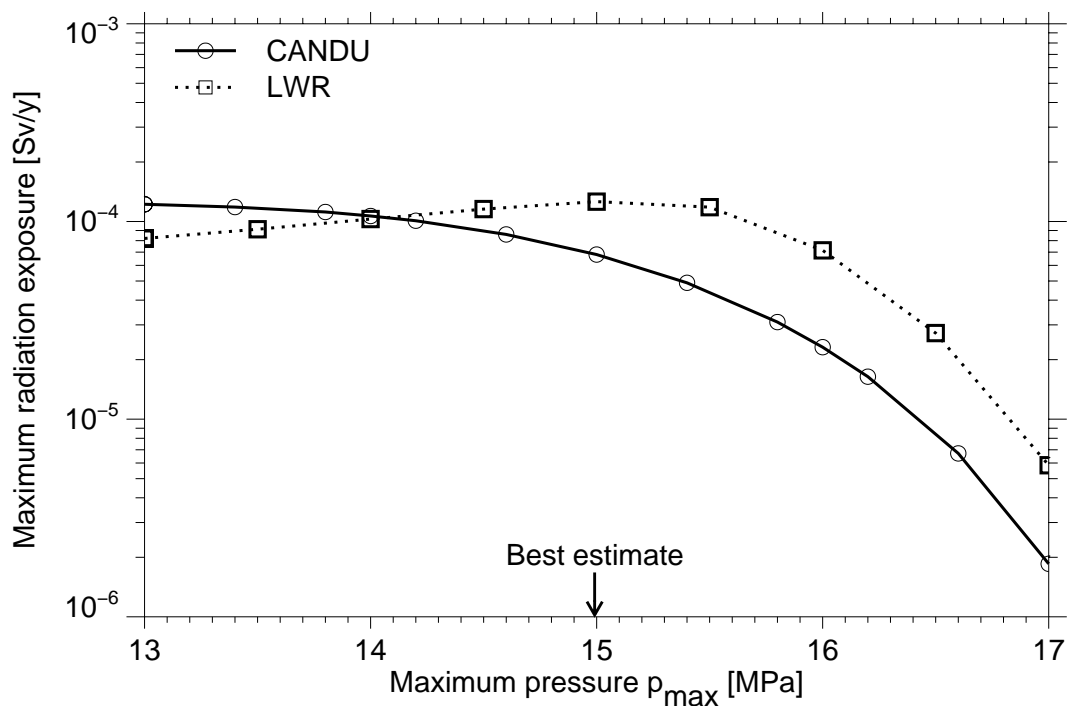


Fig. 4.16 Human intrusion scenario: Maximum radiation exposure (total dose) as function of maximum brine pressure

Table 4.7 Human intrusion scenario (CANDU fuel): Local sensitivity analyses for the maximum brine pressure – Cumulative released masses of radionuclides at times of cavern closure

Nuclide	Half life [y]	Inventory at disposal time [kg]	Total mass of mobilized nuclides [kg]	Mass of released nuclides out of the bottom of the sump [kg]			Mass of released nuclides out of the cavern [kg]		
				14 Mpa	15 Mpa	16 Mpa	14 Mpa	15 Mpa	16 Mpa
Zr-93	$1.53 \cdot 10^6$	32.8	32.8	4.3	10.6	28.6	4.2	9.9	22.0
I-129	$1.57 \cdot 10^7$	7.6	7.6	7.6	7.6	7.6	7.6	7.6	7.4
Cs-135	$2.30 \cdot 10^6$	4.1	4.1	4.1	4.1	4.1	4.0	3.9	3.4
U-236	$2.34 \cdot 10^7$	136.0	159.6	1.61	4.3	15.0	2.4	5.4	14.1
Th-232	$1.41 \cdot 10^{10}$	$4.1 \cdot 10^{-5}$	$7.5 \cdot 10^{-11}$	1.41	4.3	17.1	1.3	4.2	17.2
Np-237	$2.14 \cdot 10^6$	6.4	40.6	44.6	44.8	44.8	44.8	43.6	37.5

4.2.3 Local sensitivity analyses: Combined accident scenario

4.2.3.1 Variation of volume of brine pockets

The importance of brine pockets rests on the fact that an early intrusion of brine into emplacement drifts results in an early mobilisation of radionuclides and a slower convergence process due to support by brine pressure. In recent probabilistic investigations (e.g. [7]) it has already been shown that the volume of brine pockets is a sensitive parameter to the release of radionuclides. In the present calculations, at volumes of less than 25 m³ for CANDU and less than 200 m³ for LWR fuel, no release of radionuclides occurs at all. If the volumes of brine pockets are larger than 1 000 m³, the total doses slightly exceed the limit of 3·10⁻⁴ Sv/y in the case of CANDU fuel.

A typical plot of the temporal evolution of the radiation exposure is shown in Figure 4.17 for LWR fuel and a brine volume of 500 m³. The contributions to the total dose of the radionuclides besides I-129 and Cs-135 are at an early time lower by more than one order of magnitude than the radiation exposure resulting from I-129. At later times the long-lived radionuclides like Np-237 and Ra-225 become relevant to radiation exposure. This

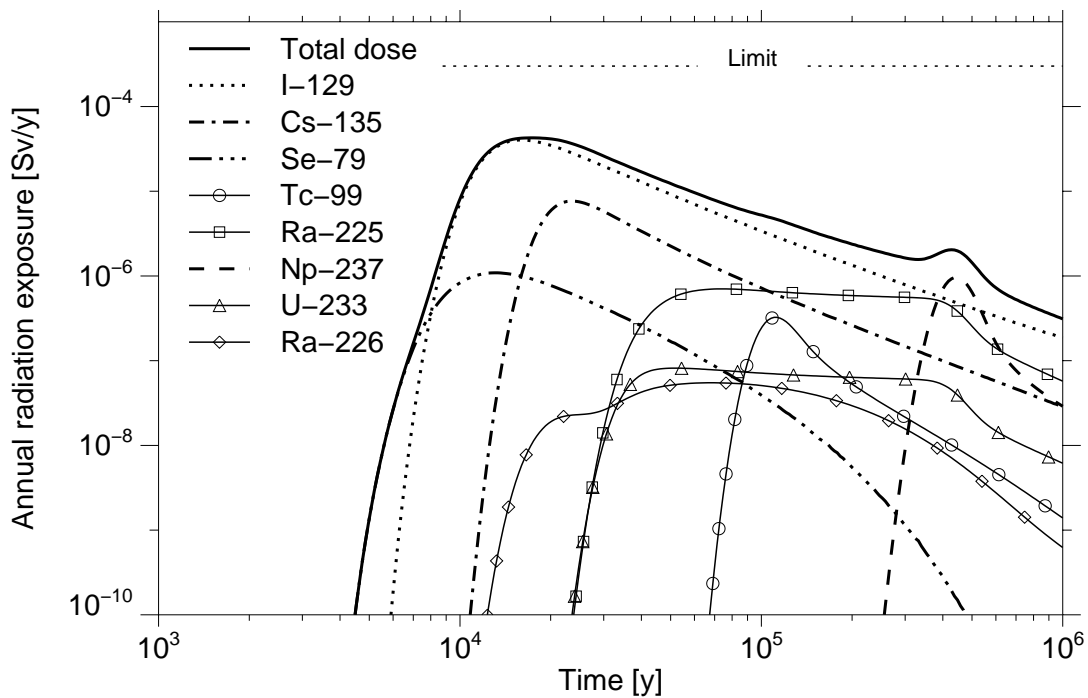


Fig. 4.17 Radiation exposures for a volume of the brine pockets of 500 m³. LWR fuel

behaviour is different from the reference case. Table 4.8. gives a survey of the calculated radiation exposures for LWR fuel and different volumes of the brine pockets.

Table 4.8 Combined accident scenario (LWR fuel): Maximum radiation exposure (total dose) as function of volume of brine pockets

Brine volume [m ³]	Total dose [Sv/y]	Release from number of drifts	Time of occurrence of maximum dose [y]
less than 200	0.0	0	-
200	$1.01 \cdot 10^{-7}$	4	296 000
250	$5.29 \cdot 10^{-7}$	4	105 000
300	$3.54 \cdot 10^{-6}$	4	32 600
500	$4.27 \cdot 10^{-5}$	6	17 200
1000	$8.31 \cdot 10^{-5}$	6	14 950

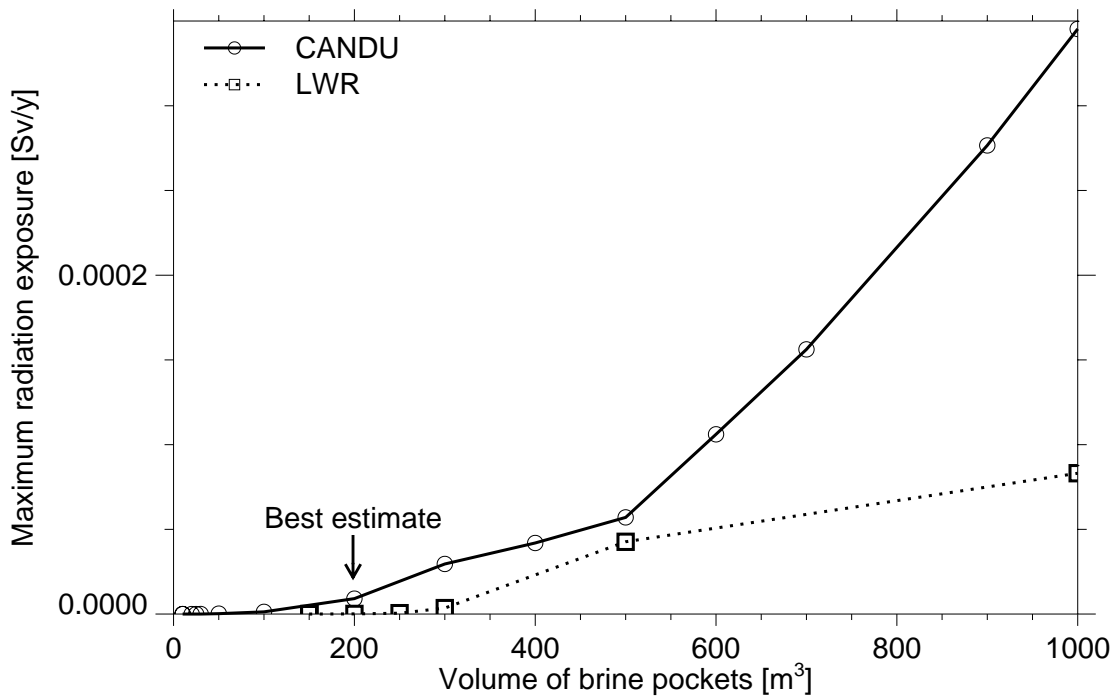


Fig. 4.18 Combined accident scenario: Maximum radiation exposure (total dose) as function of volume of brine pockets

In Figure 4.18 the dependence of the maximum radiation exposure on different volumes of the brine pockets is shown. The radiation exposures are dominated by I-129, Cs-135, Np-237, and Ra-225. It can be concluded that the volume of brine pockets is one of the most sensitive parameters with respect to radiation exposure.

4.2.3.2 Variation of the time of brine intrusion from the overburden

The time of brine intrusion is of particular importance because the intruding water reduces the convergence rate, thus keeping the segments of the repository open for longer times. The time of the brine intrusion from the overburden into the repository has been varied in the range between 1 and 1 000 y. The influence of the time of brine intrusion on radiation exposure is shown in Figure 4.19. If the brine intrudes earlier than 100 y, the main drifts are already filled with brine from the brine pockets. In this case, there is almost no influence on the radiation exposures compared to the reference case, the maximum radiation exposure being about $1 \cdot 10^{-5}$ Sv/y for CANDU fuel and about $1 \cdot 10^{-7}$ Sv/y for LWR fuel. However, if the brine intrusion from the overburden is later than about 500 y for CANDU fuel or 300 y for LWR fuel, the main field closes by convergence and no release of radionuclides occurs at all, because there is no contact of contaminated brine with the biosphere. The main contributors to radiation exposure are I-129, Cs-135, Ra-225 and Np-237.

In Figure 4.20 the effect of brine filled segments on the release is demonstrated. For three times of brine intrusion (1, 100 and 1000 y) the amount of brine in three relevant segments is shown. If the brine intrudes early after 1 y, the main drifts are filled with brine from the brine pockets and the main field is almost entirely filled with brine from the overburden. Only a small amount of brine from the pockets enters the main field. Almost the same situation occurs for the time $t_B = 100$ y. The only difference is that due to 100 years of convergence the open voids in the main field are smaller. A different situation results if the brine intrudes late after 1000 y. In this case the open voids of the main field are entirely closed due to convergence. The small amount of brine from the pockets is not sufficient to fill more than the residual open voids after the backfill in the main field has reached final porosity, which is a porosity similar to solid salt rock.

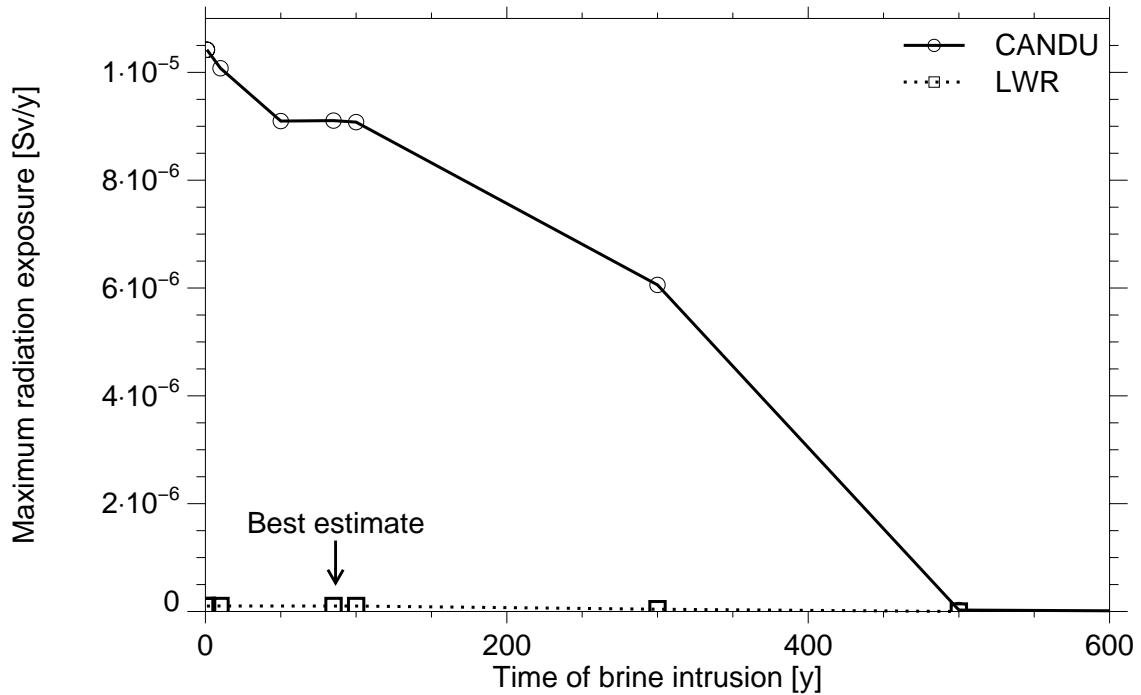


Fig. 4.19 Combined accident scenario: Maximum radiation exposure (total dose) as function of time of brine intrusion

Even for the early intrusion case, i. e. immediately after the repository closure, the radiological consequences are low, but there is a threshold effect of the intrusion time due to creep closure. The radiation exposures are in any case more than one order of magnitude below the German radiation protection limit. Nevertheless, the time of brine intrusion is a sensitive parameter with respect to radiation exposure.

4.2.3.3 Variation of the reference convergence rate

The convergence of rock salt is one of the most important parameters with respect to a release of radionuclides. In the models of the computer code used [8] it is described by the formula

$$K = K_{\text{ref}} \cdot f_p(p) \cdot f_\phi(\phi) \cdot f_T(T), \quad (13)$$

with the reference (initial) convergence rate K_{ref} , which represents the convergence rate of an empty cavity at rock temperature, with no brine, and in the reference depth of the repository. The function $f_p(p)$ describes the dependence of the convergence rate on the brine pressure in the pore volume. The functions $f_\phi(\phi)$ and $f_T(T)$ describe the dependence of the convergence rate on the porosity of the backfill and the dependence on temperature.

The reference convergence rate has been varied in the interval between 10^{-4} y^{-1} and 10^{-2} y^{-1}). The results are plotted in Figure 4.21. The total dose in all variants is dominated by I-129 followed by Ra-225 for CANDU fuel or Cs-135 for LWR fuel, respectively. There is a strong dependence of the radiation exposure on the convergence rate. A maximum of the curves occurs at about $K_r = 10^{-3} \text{ y}^{-1}$. Towards higher values the radiation exposures decrease because due to the faster convergence the amount of brine in the

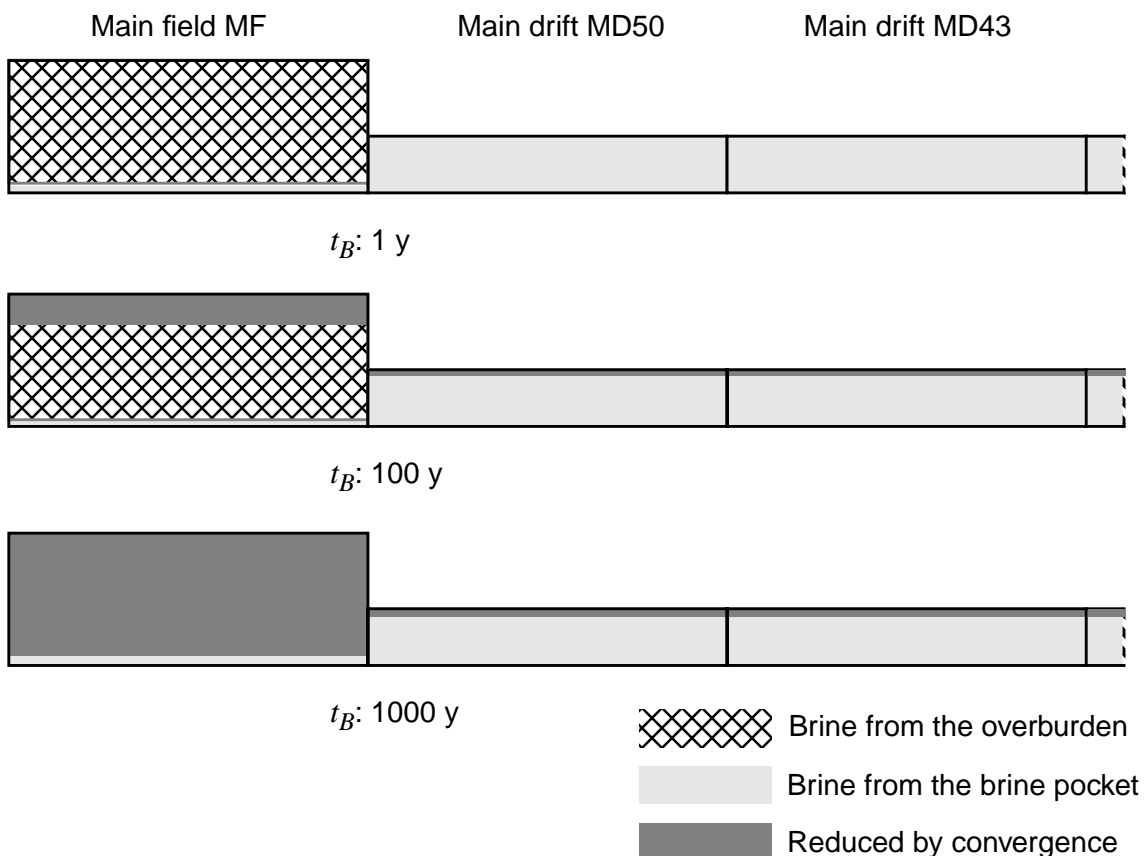


Fig. 4.20 Final state of the fill-up phase of relevant parts of the repository as function of time of brine intrusion (t_B) from the overburden

repository and consequently the release rate drops. Towards lower values of the convergence rate the radiation exposures also decrease, but this time because the convergence process itself becomes slow and consequently the release rates drop.

For CANDU fuel some additional remarks are given: for $K_r = 10^{-3} \text{ y}^{-1}$ all the emplacement drifts contribute to the release of contaminants. At $K_r = 2 \cdot 10^{-3} \text{ y}^{-1}$ one of the emplacement drifts is no longer contributing to the release and, above $K_r = 2 \cdot 10^{-3} \text{ y}^{-1}$, only 14 of the 16 emplacement drifts with brine pockets are open. This explains the sudden drop of the maximum radiation exposure. A similar observation holds for LWR fuel. The main contributors to radiation exposure are I-129 and Ra-225.

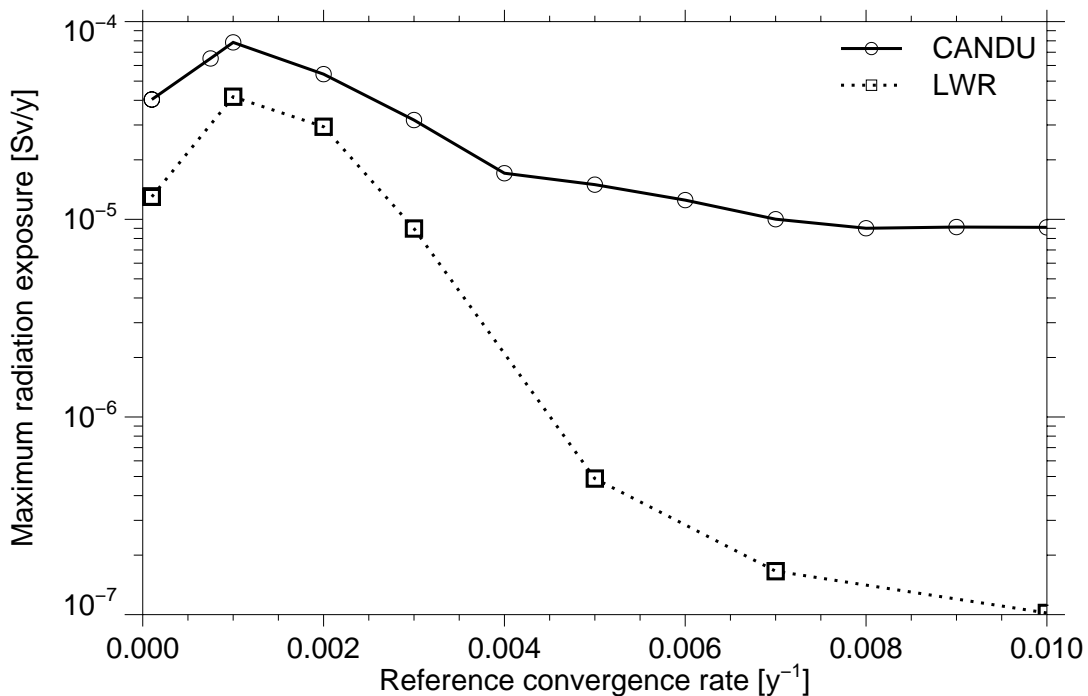


Fig. 4.21 Combined accident scenario: Maximum radiation exposure (total dose) as function of the reference convergence rate

4.2.4 Summary of results

In the following, the above described results are summarized for each scenario to stress the main differences between spent CANDU and spent LWR fuel repositories. Finally, some comparisons are made with results from the PAGIS exercise.

4.2.4.1 Subrosion scenario

In the reference cases, the maximum total doses are almost the same for CANDU and LWR fuel. In the case of CANDU fuel, the radiation exposure is slightly above the German radiation protection limit of $3 \cdot 10^{-4}$ Sv/a; in the case of LWR fuel, the radiation exposure is slightly below this limit.

A decrease of the subrosion rate results in a decrease of the radiation exposures. For extremely low subrosion rates (less than about 0.0005 mm/y), most of the radionuclides are decayed and do not contribute to the radiation exposure. Nevertheless, even in that case the release of the long-lived nuclide U-234 results in a maximum radiation exposure almost as high as in the reference case.

4.2.4.2 Human intrusion scenario

For the reference case, the release rates of a large number of radionuclides into the overburden have been calculated. The maxima of the release rates are shown to occur between 10^4 y and 10^5 y. For both fuels, the cavern attains its final porosity after about 900 000 y. After that time, no more release from the cavern into the overburden is possible.

The maximum radiation exposure has a value of $6.8 \cdot 10^{-5}$ Sv/y ($1.26 \cdot 10^{-4}$ Sv/y for LWR fuel) and is caused by Np-237. It occurs at about 494 000 y after disposal (553 000 y for LWR fuel). The radiological consequences of LWR fuel are slightly higher than for CANDU fuel, mainly due to its higher temperatures.

Local sensitivity analyses have been performed in order to investigate the sensitivity of a radionuclide release to the overburden. The parameters have been selected using the maximum radiation exposure as a criterion.

For both fuels, the ranking of parameters by importance is the following:

- brine pressure p_{max} ,
- reference convergence rate K_r ,
- diffusion coefficient, and
- solubility limits.

The variation of the exponent in the porosity-permeability relation q has no effect on the radiation exposure.

For CANDU fuel, in the variant with low brine pressure the calculated radiation exposures are close to the German radiation protection limit. For LWR fuel this limit is already almost reached with best estimate values of the parameters. Nevertheless, the consequences of this human intrusion scenario are acceptable, especially because its probability is low.

4.2.4.3 Combined scenario

In the reference cases, the maximum radiation exposures are different by almost two orders of magnitude. In the case of CANDU fuel, the radiation exposure is higher because all the emplacement fields contribute to the release. Also, there is a higher amount of water intruding into the repository compared to the repository with LWR fuel.

Low layout temperatures generated by CANDU fuel are keeping the repository open for more than 10^6 years. The radiological consequences for this repository are higher than for LWR fuel. For the CANDU repository, only sections not connected with brine pockets are sealed before water from the overburden can reach the emplacement drifts. Thus, all emplacement fields contribute to the release of radionuclides. On the other hand, in the LWR repository only fuel elements from the 7th field contribute to the radiation exposure, because the connection between the 7th field and the rest of the repository is broken due to an early closure of the main drift MD43 by convergence.

For both fuels the ranking of parameters by importance is the following:

- volume of brine pockets,
- reference convergence rate, and
- time of brine intrusion.

The first and the last parameter have a threshold effect.

The main difference in the results for the two fuel types is caused by the low temperatures in the repositories with CANDU spent fuel. In that case, a volume of the brine pockets higher than about 800 m³ results in exceeding the German radiation protection limit. For both fuels, the most important contributor to radiation exposure is I-129. The next important nuclides are Ra-225 and Np-237 for CANDU fuel, or Cs-135 and Np-237 for LWR fuel, respectively.

4.2.4.4 Comparison with results of the PAGIS exercise

While the present study deals with direct disposal of spent fuel elements, the PAGIS exercise [6] aimed at the investigation of disposal of vitrified high level waste. Thus, a comparison of the results is fruitful because many of the models and assumptions of PAGIS have been adopted for this study. In Chapter 4.2.1, the results for subsidence have already been compared with PAGIS results. The maxima of the radiation exposures in PAGIS turned out to be more than 2 orders of magnitude lower than in this study, mainly due to the large vertical dimensions of the mine.

For the other scenarios – human intrusion and combined accident – the results of the comparison are shown in Figure 4.22. For the cavern scenario the annual radiation exposures are similar over the entire time period of the scenario for spent CANDU and spent LWR fuel respectively, but the values are generally lower for spent CANDU fuel. In the PAGIS results, the radiation exposure is over a long time period lower than for spent CANDU fuel, but the maximum radiation exposure is of the same order of magnitude as in the CANDU or LWR cases. This is a direct consequence of the geometrical arrangement of emplacement drifts or boreholes. I. e. the differences in the calculated radiation

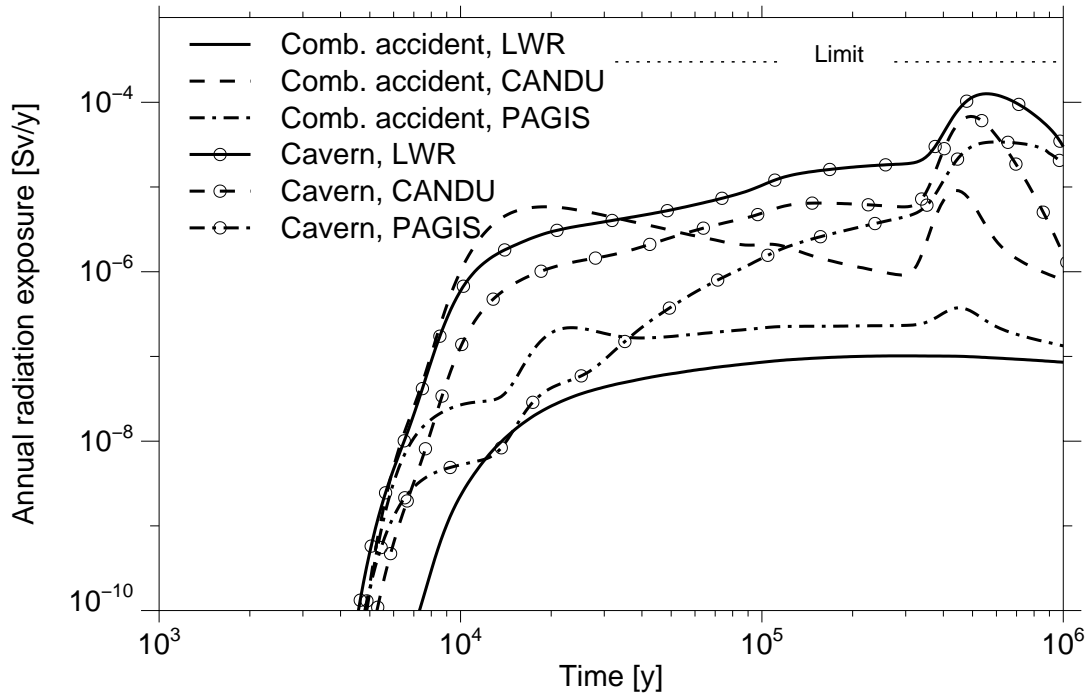


Fig. 4.22 Comparison of annual radiation exposures (total dose) with PAGIS results

exposures are a consequence of the different nuclide inventories affected by the solution mined cavern of the scenario. In the case of PAGIS, the low radiation exposures at early times result from a lower nuclide inventory of fission products.

For the combined accident scenario the results for spent CANDU and spent LWR fuel are quite different. This is a consequence of the different temperatures in the repository due to the much lower heat production of spent CANDU fuel. In the LWR case many drifts are closed by convergence at early times and only a few emplacement drifts contribute to the release of radionuclides, while in the CANDU case the entire repository contributes to the release. Thus, the radiation exposure is much higher in the CANDU case. The PAGIS curve shown in Figure 4.22 has been recalculated with the new computer code EMOS and with a volume of the brine pocket of 200 m^3 , which is the same as in the present study but higher than in the reference case discussed in [6]. The radiation exposures are slightly higher than in the LWR case, which is mainly a consequence of the different nuclide inventories in the affected HLW borehole and the affected LWR emplacement drifts.

5 Summary and conclusions

Performance assessments for a hypothetical repository in a salt formation revealed differences in the calculated consequences if either spent CANDU fuel or spent LWR fuel is disposed of. Deterministic calculations and local sensitivity analyses with respect to some of the most influential parameters have been performed for three scenarios: subsidence, combined accident, and human intrusion. The differences in the modelling for CANDU and LWR fuel are in the inventories and temperatures of the waste emplacement fields. The results have been mainly discussed in terms of effective doses. The calculated consequences for the LWR case are similar to earlier calculations of the PAGIS project of the European Union.

For the subsidence scenario with best estimate values of the input parameters, the radiation exposures are at the German radiation protection limit of $3 \cdot 10^{-4}$ Sv/y. A maximum radiation exposure of $3.7 \cdot 10^{-4}$ Sv/y has been calculated for CANDU fuel and $1.5 \cdot 10^{-4}$ Sv/y for LWR fuel, respectively. For both fuels, the main contributor to radiation exposure is U-234.

The subsidence rate and the acceptable salt concentration of drinking water are critical parameters in this scenario. For a high subsidence rate of 2.2 mm/y the maximum radiation exposures are $5.3 \cdot 10^{-4}$ Sv/y for CANDU fuel and $1.5 \cdot 10^{-3}$ Sv/y for LWR fuel, respectively. Low subsidence rates of 0.0005 mm/y result in maximum radiation exposures of $3.1 \cdot 10^{-4}$ Sv/y for CANDU fuel and $1.1 \cdot 10^{-4}$ Sv/y for LWR fuel. The salt concentration has a linear effect on the calculated radiation exposures. A reduction of the salt concentration by a factor reduces the radiological consequences by the same factor. For the assumed range of salt concentrations, the calculated maximum radiation exposures are in the range of 10^{-5} Sv/y to $1.7 \cdot 10^{-2}$ Sv/y for CANDU fuel and $3.5 \cdot 10^{-6}$ Sv/y to $4.8 \cdot 10^{-2}$ Sv/y for LWR fuel, respectively.

The subsidence scenario includes some very conservative assumptions which overestimate the calculated radiation exposures. The most important assumption is that the barrier effect of the geosphere is omitted, i. e. there is no retardation of the primary nuclides and no dispersion in the geosphere. More realistic models are expected to reduce the calculated radiological consequences drastically.

In the human intrusion scenario with best estimate values of input parameters, the maximum radiation exposure for CANDU fuel is $6.8 \cdot 10^{-5}$ Sv/y ($1.3 \cdot 10^{-4}$ Sv/a for LWR fuel) and is mainly caused by Np-237. This maximum occurs at about 494 000 y after disposal (553 000 y for LWR fuel). The radiological consequences for LWR fuel turned out to be generally slightly higher than for CANDU fuel, mainly due to the higher temperatures resulting in faster convergence.

Local sensitivity analyses have been performed to investigate the influence of some input parameters on the radionuclide release to the overburden. The following parameters have been selected:

- solubility limits
- diffusion coefficient
- reference convergence rate K_r
- maximum brine pressure p_{max}

The variation of the exponent in the porosity-permeability relation q turned out to have no effect on the radiation exposure.

In some variants the maximum radiation exposures can rise to values higher than the best estimate value, but they are generally lower than about $2.5 \cdot 10^{-4}$ Sv/y for both CANDU and LWR fuel. Thus, the consequences of the human intrusion scenario are acceptable, especially because its probability of occurrence is low.

In the combined accident scenario an intrusion of brine from the overburden into the repository via the main anhydrite is considered in combination with a limited brine intrusion from brine pockets which are located in the neighbourhood of the emplacement galleries. Applying best estimate values of the input parameters, the maximum radiation exposures for this scenario are $9 \cdot 10^{-6}$ Sv/y for CANDU fuel and $1 \cdot 10^{-7}$ Sv/y for LWR fuel. The most relevant nuclides are I-129 and Ra-225 for CANDU fuel, and I-129 and Cs-135 for LWR fuel, respectively.

As a consequence of the low temperatures in the repository with CANDU fuel, especially emplacement drifts connected to a brine pocket stay open for a long period of time. Thus,

drifts of all emplacement fields contribute to the radionuclide release out of the repository. This is different for LWR fuel. In this case, only the drifts from one emplacement field adjacent to the main field contribute to the radionuclide release, because all the other drifts are closed by convergence before they are reached by brine. As a consequence, the calculated radiation exposures are higher for CANDU fuel, although the inventories are generally lower.

Three parameters have been assumed to be important to radiological consequences in the combined accident scenario:

- volume of brine pockets
- time of brine intrusion from the overburden
- reference convergence rate

The maximum radiation exposures increase with increasing volume of the brine pockets. Below a threshold value of 25 m³ for CANDU fuel (200 m³ for LWR fuel) no release of nuclides occurs at all. The time of brine intrusion also has a threshold effect: if the brine intrudes later than about 500 y, no release of radionuclides occurs at all. The highest radiation exposures are close to the reference values and occur for brine intrusion immediately after closure of the repository. The variation of the reference convergence rate yields a maximum of the calculated radiation exposures of about 8·10⁻⁵ Sv/y for CANDU fuel and 4·10⁻⁵ Sv/y for LWR fuel at values of about 1·10⁻³ y⁻¹.

The results of the combined accident scenario are different from the results of the subsion scenario in that the radiation exposures for CANDU fuel are generally higher than for LWR fuel. The reason is that in the combined accident scenario in the LWR case the high inventory is “shielded” because only parts of the repository are involved in a release of radionuclides as described above. In the subsion scenario, for both fuel types the total inventories contribute to the release and thus, the radiation exposure is lower for CANDU due to the lower inventory.

The calculated radiation exposures for the human intrusion scenario are between those for the subsion and the combined accident scenario and are of comparable height for CANDU and LWR fuel. In these cases the inventories contributing to the release are

almost the same although the total inventories are different. But the affected inventories are given by the dimensions of the cavern, which hits upon more CANDU than LWR containers.

The layout temperature turned out to be a parameter with an overwhelming importance in the combined accident scenario. It strongly affects the release from the repository and, finally, the radiological consequences to humans. Nevertheless it should be emphasised that the temperature field for the CANDU repository is based on some rough approximations and it should be recalculated for future studies.

6 References

- [1] Boese, B.; Buhmann, D.; Hirsekorn, R.-P.; Storck, R.; Tix, C.: Weiterentwickelte Modellansätze chemischer und physikalischer Effekte im Grubengebäude eines Endlagers im Salinar. Gesellschaft für Anlagen- und Reaktorsicherheit (GRS) mbH, GRS-123, Braunschweig 1996

- [2] Buhmann, D.: Das Programmpaket EMOS. Ein Instrumentarium zur Analyse der Langzeitsicherheit von Endlagern. Gesellschaft für Anlagen- und Reaktorsicherheit (GRS) mbH, GRS-159, Braunschweig 1999

- [3] Buhmann, D.; Brenner, J.; Storck, R.: The Efficiency of Source Terms in Performance Assessments for Salt Repositories. In: High-Level Radioactive Waste Management. Proceedings of the Fifth Annual Intern. Conference, 22.-26.05.1994, Las Vegas. p. 501-507. ANS and ASCE New York/USA 1994

- [4] Buhmann, D.; Nies, A.; Storck, R.: Analyse der Langzeitsicherheit von Endlagerkonzepten für wärmeerzeugende radioaktive Abfälle. GSF-Bericht 27/91. GSF - Forschungszentrum für Umwelt und Gesundheit GmbH, Braunschweig 1991

- [5] Johnson, L.H. et al.: The disposal of Canada's Nuclear Fuel Waste: A Study of Postclosure Safety of In-Room Emplacement of Used CANDU Fuel in Copper Containers in Permeable Plutonic Rock, Volume 2: Vault Model. Atomic Energy of Canada Ltd., AECL-11494-2, COG-95-552-2, 1996

- [6] Storck, R.; Aschenbach, J.; Hirsekorn, R.-P.; Nies, A.; Stelte, N.: Performance Assessment of Geological Isolation Systems for Radioactive Waste (PAGIS): Disposal in Salt Formations. EUR 11 778 EN, GSF-Bericht 23/88. Commission of the European Communities, Gesellschaft für Strahlen- und Umweltforschung mbH München, Brussels-Luxembourg 1988

- [7] Storck, R. and Buhmann, D.: A Comparison of Long-Term Safety Aspects – Concepts for Disposal of Spent Fuel and Wastes from Reprocessing. Nuclear Technology 121, 212-220, February 1998
- [8] Storck, R.; Buhmann, D.; Hirsekorn, R.-P.; Kühle, T.; Lührmann, L.: Das Programmpaket EMOS zur Analyse der Langzeitsicherheit eines Endlagers für radioaktive Abfälle. Version 5. Gesellschaft für Anlagen- und Reaktorsicherheit (GRS) mbH, GRS-122, Braunschweig 1996
- [9] Tait, J. C.; Gauld, I. C. and Wilkin, G. B.: Derivation of initial radionuclide inventories for the safety assessment of the disposal of used CANDU fuel. Atomic Energy of Canada Ltd., AECL-9881, 1989

Acknowledgements

The authors gratefully acknowledge financial support by the Scientific and Environmental Affairs Division of NATO under contract number LG 972750.

List of Figures

Figure 2.1	Subrosion scenario: model of nuclide migration.....	7
Figure 2.2	Temperature curves for the sump.....	14
Figure 2.3	Part of the section system of the near field	15
Figure 2.4	Modelled section structure of the near field.....	16
Figure 2.5	Amount of failed containers n_c and container failure rate with exponential distribution of container failure rate	19
Figure 2.6	Cumulated release rates of Zr-93 for the regions of LWR fuel elements.....	21
Figure 2.7	Relative release rates (thin lines) and cumulated release (thick lines) of Zr-93 for different regions of an LWR fuel element	22
Figure 3.1	Temperature curves for calculation of convergence of brine pockets ...	27
Figure 3.2	Temperature curves for calculation of convergence of backfill of emplacement drifts	27
Figure 3.3	Temperature curves for calculation of convergence of backfill in connecting drifts	28
Figure 3.4	Comparison of temperature curves for calculation of convergence of the segments of emplacement field 7.....	28
Figure 3.5	Comparison of heat production rate of one container with CANDU or LWR fuel, resp. for times after discharge from the reactor	30
Figure 3.6	Sketch of the cavern system	38
Figure 3.8	Time scale of the cavern scenario.....	40
Figure 3.7	Estimation of affected containers by the solution mining of the cavern.....	41
Figure 4.1	Flow of brine out of the sump and out of the cavity	45
Figure 4.2	Release rates of I-129 from the bottom part of the sump.....	46
Figure 4.3	Release rates of I-129 out of the top part of the sump and out of the cavity	47
Figure 4.4	Release rates of dose relevant nuclides from the cavern (LWR fuel) ...	48
Figure 4.5	Release rates of dose relevant nuclides from the cavern (CANDU fuel).....	48
Figure 4.6	Human intrusion scenario (CANDU fuel): Temporal evolution of the radiation exposure in the reference case.....	49

Figure 4.7	Human intrusion scenario (LWR fuel): Temporal evolution of the radiation exposure in the reference case.....	50
Figure 4.8	Combined accident scenario (CANDU fuel): a) above: Flow of brine into and out of the main field; b) below: Flow of brine out of the main field, out of an emplacement drift, and out of a brine pocket	53
Figure 4.9	Combined accident scenario (CANDU fuel): Temporal evolution of the radiation exposure in the reference case.....	54
Figure 4.10	Combined accident scenario (LWR fuel): Temporal evolution of the radiation exposure in the reference case.....	57
Figure 4.11	Comparison of subsrosion process for deep and flat repositories	59
Figure 4.12	Human intrusion scenario (CANDU fuel): Maximum radiation exposure (total dose) as function of solubility limit	61
Figure 4.13	Human intrusion scenario: Maximum radiation exposure (total dose) as function of diffusion coefficient.....	62
Figure 4.14	Human intrusion scenario: Maximum radiation exposure (total dose) as function of reference convergence rate	63
Figure 4.15	Human intrusion scenario (CANDU fuel): Local sensitivity analyses for the reference convergence rate – Released masses from the cavity after 10^6 y.....	64
Figure 4.16	Human intrusion scenario: Maximum radiation exposure (total dose) as function of maximum brine pressure.....	66
Figure 4.17	Radiation exposures for a volume of the brine pockets of 500 m^3 . LWR fuel	67
Figure 4.18	Combined accident scenario: Maximum radiation exposure (total dose) as function of volume of brine pockets	68
Figure 4.19	Combined accident scenario: Maximum radiation exposure (total dose) as function of time of brine intrusion.....	70
Figure 4.20	Final state of the fill-up phase of relevant parts of the repository as function of time of brine intrusion (t_B) from the overburden	71
Figure 4.21	Combined accident scenario: Maximum radiation exposure (total dose) as function of the reference convergence rate	72
Figure 4.22	Comparison of annual radiation exposures (total dose) with PAGIS results	76

List of Tables

Table 3.1	Design data	29
Table 3.2	Initial radionuclide inventories per container in Bq for 30 y old spent LWR and 10 y old spent CANDU fuel	31
Table 3.3	Fractions of the inventories of selected elements in the cladding a_C , the gas gap a_G , and the fuel matrix a_F . Solubility limits L in emplacement drifts and connecting drifts (mol/l)	32
Table 3.4	Dose conversion factors	33
Table 3.5	Specific input data for the subsrosion scenario	34
Table 3.6	Input data for the subsrosion scenario	35
Table 3.7	Selected input parameters for the human intrusion scenario	39
Table 4.1	Preliminary tests on the influence of section temperatures on radiological consequences. CANDU fuel	44
Table 4.2	Time of precipitation of solubility controlled nuclides in the bottom of the sump	47
Table 4.3	Combined accident scenario (CANDU fuel): Time history of segments	51
Table 4.4	Combined accident scenario (LWR fuel): Time history of segments	55
Table 4.5	Subrosion scenario: Maximum radiation exposure [Sv/y] for CANDU and LWR fuel as function of subsrosion rate and concentration of salt	58
Table 4.6	Subrosion scenario (CANDU fuel): Maximum radiation exposure [Sv/y] as function of subsrosion rate. Concentration of salt: 31 mg/l.....	58
Table 4.7	Human intrusion scenario (CANDU fuel): Local sensitivity analyses for the maximum brine pressure – Cumulative released masses of radionuclides at times of cavern closure	66
Table 4.8	Combined accident scenario (LWR fuel): Maximum radiation exposure (total dose) as function of volume of brine pockets.....	68

